2-2010

Modeling of Thermal Non-Equilibrium in Superheated Injector Flows

Shivasubramanian Gopalakrishnan
University of Massachusetts Amherst, shivasub@acad.umass.edu

MODELING OF THERMAL NON-EQUILIBRIUM IN SUPERHEATED INJECTOR FLOWS

A Dissertation Presented

by

SHIVASUBRAMANIAN GOPALAKRISHNAN

Submitted to the Graduate School of the
University of Massachusetts Amherst in partial fulfillment
of the requirements for the degree of

DOCTOR OF PHILOSOPHY

February 2010

Mechanical and Industrial Engineering

MODELING OF THERMAL NON-EQUILIBRIUM IN SUPERHEATED INJECTOR FLOWS

A Dissertation Presented

by

SHIVASUBRAMANIAN GOPALAKRISHNAN

Approved as to style and content by:

David P. Schmidt, Chair

J. Blair Perot, Member

Dimitrios Maroudas, Member

Donald Fisher, Department Head
Mechanical and Industrial Engineering

To my beloved parents.

EPIGRAPH

Asato maa sadgamaya

Tamaso maa jyotirgamaya

Mrityor maa amritamgamaya

– Brihadaranyaka Upanishad 1.3.28.

From the untruth to the truth

From darkness to light

From death to immortality

ACKNOWLEDGMENTS

Though the Phd. degree is conferred on a single individual, the effort, at various levels, to obtain this degree is almost always put in by several people. This dissertation has a similar story and is an outcome of the support of many people without whom this would not have been possible.

At the outset I would like to thank my advisor, Prof. David P. Schmidt. The past 6 years under his guidance has been a fantastic learning experience, one which I will cherish for life. His openness to new ideas and willingness to try experimenting with them is remarkable. I also thank Prof. Blair Perot for giving great support and constant fresh ideas. I appreciate him being a part of my dissertation committee. I also acknowledge the computational resources provided by him. I thank Prof. Dimitrois Maroudas for serving on my dissertation committee and providing an extra dimension to it.

I acknowledge the technical contributions and criticisms provided by Dr. Ron Grover of GM and Dr. Jerry Lee of UTRC. I also acknowledge the support provided by Dr. Hrvoje Jasak of Wikki ltd. This work was done with the financial support of NASA under Contract No.NNC07CB05C.

I would like to thank my parents and my brother, Hari. They have been an amazing source of constant support and encouragement. I am eternally indebted to my parents, who sacrificed so much for the education that me and my brother received and also for supporting every decision I took in my career.

During the past 6 years at the CFD lab, I was fortunate to interact with several bright minds. The list of people I got know as colleagues and friends is just way too

long for this section. I would like acknowledge each and every one for a wonderful time and sharing their brilliant ideas.

I would also like to express gratitude to all my close friends, both near and far, who have given me encouragement, been with me through rough times and shared good times. You all know who you are and how much you mean to me. Finally, I would like to thank my landlords, Merle and Billie Howes, who not only provided an apartment but also a home to live in. You have been more than family to me.

ABSTRACT

MODELING OF THERMAL NON-EQUILIBRIUM IN SUPERHEATED INJECTOR FLOWS

FEBRUARY 2010

SHIVASUBRAMANIAN GOPALAKRISHNAN

B.E., UNIVERSITY OF MUMBAI, BOMBAY

Ph.D., UNIVERSITY OF MASSACHUSETTS AMHERST

Directed by: Professor David P. Schmidt

Among the many factors that effect the atomization of a fuel spray in a combustion chamber, the flow characteristics of the fuel inside the injector nozzle play significant roles. The enthalpy of the entering fuel can be elevated such that it is higher than the local or downstream saturation enthalpy, which will result in the flash-boiling of the liquid. The phase change process dramatically effects the flow rate and has the potential to cause subsonic two-phase choking. The timescale over which this occurs is comparable to the flow-through time of the nozzle and hence any attempt to model this phenomenon needs to be done as a finite rate process. In the past the Homogeneous Relaxation Model (HRM) has been successfully employed to model the vaporization in one dimension. Here a full three dimensional implementation of the HRM model is presented. Validations have been presented with experiments using water as working fluid.

For the external spray modeling, where the fuel is said to be flash boiling, the phase change process plays a role alongside the aerodynamic breakup of the liquid

and must be considered for obtaining the fuel spray characteristics. In this study the HRM model is coupled with Linearized Sheet Instability Analysis (LISA) model, for primary atomization, and with Taylor Analogy Breakup (TAB) model for secondary breakup. The aerodynamic breakup model and phase change based breakup model are designed as competing processes. The mechanism which satisfies its breakup criterion first during time integration is used to predict resulting drop sizes.

TABLE OF CONTENTS

LIST OF TABLES

Table **Page**

LIST OF FIGURES

Figure **Page**

CHAPTER 1

INTRODUCTION

The rise in popularity of direct injection systems for gasoline engines necessitates the understanding of the complex phenomena of the fuel spray and its vaporization. The spray structure in the combustion chamber is affected by the external breakup of the jet which itself depends upon the internal flow characteristics in the fuel injector nozzle. The fuel in the injection system can acquire heat from the relatively hot surroundings and from compression during pumping, raising its temperature and the vapor pressure. If the pressure downstream of the injector is less than the vapor pressure, the fuel will likely flash boil. Though primarily associated with gasoline direct injection [49], recent work has suggested that flash-boiling could play a role in premixed-charge compression ignition engines with special fuels [61].

Similarly, in high performance jet engines, such as those found in military aircrafts or those proposed for supersonic civilian applications, the proposition to utilize jet fuel as a heat sink may positively impact both the aircrafts thermal management and combustor performance. System level analysis indicated that to meet future heat load requirements, the temperature of the jet fuel would need to be raised to beyond 700^{o}F. Recent advancement in fuel treatment methods can indeed stabilize jet fuel to mitigate coking in this temperature range [54, 50]; however, the high fuel temperature greatly raises the potential for the fuel to be in the superheated state. On the negative side, there is the risk of vapor lock in the fuel line; whereas, the effect of superheating the fuel on the spray and atomization can improve mixing and

thus combustor performance and emissions as has been shown in experiments and theoretical analysis performed with gasoline direction injection systems [51, 67, 64].

Flash boiling is a phenomenon similar to cavitation, which is also known to occur in gasoline injectors [35]. Both are a transition from liquid to vapor due to a drop in pressure. In contrast to nucleate boiling, the enthalpy for vaporization is not provided at walls during the phase change process, but is instead provided by inter-phase heat transfer. A gross distinction between cavitating and flash-boiling nozzle flow is simply that the enthalpy of the cavitating flow is below the saturated liquid enthalpy at the downstream pressure, while the enthalpy of the flash-boiling flow exceeds the saturated liquid enthalpy at the downstream pressure. A detailed discussion of the differences must be deferred until after some review of phase change physics.

An experimental study by Oza and Sinnamon [40] found that flashing occurred in two modes, namely the "external flashing mode" and the "internal flashing mode." Park and Lee [41] performed investigations using transparent nozzles and reported the flashing modes in the internal and the external flow. Apart from the degree of superheat it was found that the factors affecting flash boiling included the nozzle geometry, surface roughness, turbulence and physical properties of the fuel. The external spray characteristics as result of flash boiling of superheated fuel have been studied experimentally by several researchers [58, 66, 1].

Even though only a very small fraction of the liquid mass changes phase while still in the nozzle, this small amount of mass can occupy a large volume and greatly affect the nozzle flow. However, there are many investigations of external sprays under flash-boiling conditions and relatively few studies of the internal flashing flow. As noted by Park and Lee [41], the phase change process definitely begins within the nozzle. Experimental studies of flashing nozzle flow have primarily been conducted with water, such as Reitz [43] and Fauske [17]. Fauske noted that the flow through nozzles

will choke under saturated conditions (with respect to the upstream conditions) and low downstream pressure.

There have been a few attempts to model the internal flashing flow, almost all limited to one-dimensional flow. For a recent example of one-dimensional modeling, the reader may consult Barret et al. [2]. Such models are often not satisfactory for the low length-to-diameter ratios used in most fuel injector nozzles, where the nozzle flow is separated and displays two and three-dimensional features. Schmidt et al. [47] reported the development of a two-dimensional flashing simulation for simple nozzle shapes, which offers some insights into short flashing-nozzle flow. However, Schmidt et al. were limited to simple, two-dimensional block-structured meshes. This initial effort produced a code that was not terribly robust or efficient. Fortunately, the numerical techniques available and the understanding of the special requirements of modeling flashing flow have progressed.

Any numerical investigation in the physics of the atomization consists of two distinct sections,the external jet break up and the internal nozzle flow. The calculations of the nozzle flow calculations serve as inputs to external jet break up models. The external modeling of flash boiling sprays has been presented in the past by Zeng et al. [68], Zuo et al [69], and Kawano et al. [25].

These external spray models have been developed with the best information available, but the open literature has very little to offer about the details of the internal flashing flow. Important questions remain about the velocity of the fluid leaving the nozzle and the fraction of vapor present at the nozzle exit. Further, we wish to know more about how nozzle geometry and injection pressure affect the internal flow.

When a hot fluid has a vapor pressure that falls between the upstream and downstream pressure in a nozzle, the discharge of the nozzle may be sensitive to the effects of inter-phase heat transfer. This heat transfer will take place on small length scales and will be affected by interfacial and turbulent dynamics. Neither the details of the

small-scale temperature fluctuations, the amount of interfacial area, nor the small scale velocity features are known. Despite these complexities, the limits of thermal equilibrium and frozen flow have been useful for very long and very short nozzles, respectively. An intermediate closure that addresses the finite rate of heat transfer between phases would provide wider applicability to nozzle geometries. If the analyses could further be extended to multiple dimensions, then multi-dimensional CFD techniques could be applied to studying flash-boiling nozzles.

The rate of heat transfer and its role as a limiting factor in phase change depends largely upon the temperature of the fluid. Pressure-driven phase change can be viewed as a spectrum with cavitation at the cold end of the spectrum and flash-boiling at the hot end. In some cavitating flows, the time scales of heat transfer can be assumed to be much faster than the time scales governing acceleration due to pressure [28]. Consequently, for small, high-speed cavitating flows, thermal equilibrium assumptions have produced successful cavitation models [48]. Under such conditions, the vapor density of the cold fluid is very small and is not significant when compared to the liquid density. Thus little energy transfer is required to produce vapor.

In contrast, for hot liquid the phase change is more like a boiling process. The difference between the saturated vapor density and saturated liquid density decreases at higher temperature. Consequently, the liquid must provide more energy per unit volume of vapor. Thus flashing nozzle simulations require additional modeling of finite-rate heat-transfer processes. Further distinctions are provided by Sher et al. [15], who reviewed and categorized typical modeling approaches. Classic studies by Wallis [62], Fauske [17], Henry and Fauske [19], and Moody [34] have explored the role of thermal non-equilibrium in a variety of channel geometries. In an interesting bridge between the two regimes, Vortmann et al have modeled cavitation with a return-to-equilibrium approach [60].

Kato et al. [24] presented an analysis that indicates when thermal effects limit bubble growth. Kato et al. numerically integrated the Rayleigh-Plesset equation and the energy equation. For a boundary condition at the phase interface, Kato calculated the rate of energy transferred out of the liquid by conduction, as the interface produced vapor. The vapor production gave the growth rate of the bubble, and thus the wall velocity. One of their main observations was the significance of Jakob number and the change in governing phenomena over the lifetime of a growing bubble.

Mach number effects are another phenomenon thought to play an important role in the flashing of superheated fluids. Simões-Moreira and Bullard [37] modeled high-speed jets emanating from short nozzles, where expansion waves formed downstream of a liquid core. They applied the solution of a Chapman-Jouguet wave to the process of flash-boiling and predicted choked flow downstream of the wave.

Empirical observations are also essential. In experiments such as Reitz [43], the mass flow rate through a short nozzle was clearly a function of upstream liquid temperature. As the temperature of the upstream liquid approached the vapor temperature at the upstream conditions, mass flow rate decreased. When heated to a point just below the upstream vapor temperature, the flow rate dropped abruptly. Kim and O'Neal [27] made observations of refrigerants flashing in short tubes. Another phenomena that can occur in slightly subcooled flows are condensation shocks, as observed in experiments by Mironov and Razina [65].

However, the complex physics are only the first obstacle to creating CFD simulations of phase change. Depending on the speed and size of the channel flow, the rate of heat transfer can range from slow, e.g. the thermal equilibrium limit, to very fast, namely the frozen-flow limit. When the rate of phase change is extremely fast, numerical stiffness problems can occur. Unless an implicit model of heat transfer is closely coupled to conservation of mass and momentum equations, the resulting scheme may

be limited to very small time steps. For application to transient, three-dimensional flow, severe stability constraints would render an explicit model prohibitively expensive.

This work deals with the construction of new fully three dimensional CFD solver which models the thermal non-equilibrium in the phase change process as a finite rate process and the Homogeneous Relaxation Model (HRM) is used for this purpose. For the external spray atomization and breakup, the HRM model is coupled with Linearized Sheet Instability Analysis (LISA) model, for primary atomization, and with Taylor Analogy Breakup (TAB) model for secondary breaku. The aerodynamic breakup model and phase change based breakup model are qdesigned as competing p rocesses. The mechanism which satisfies its breakup criterion first during time integration is used to predict resulting drop sizes.

CHAPTER 2

INTERNAL FLOW MODELING

The foremost question in a CFD simulation of flash boiling is how to model the heat transfer between the two phases. The rate of heat transfer between the two phases can limit the phase change and is invariably dependent on the temperature of the liquid. This role of heat transfer may be contrasted to cavitating flow. For cavitating flows [28] the temperature of the entering fluid is generally quite low and the energy transfer from the liquid phase to the vapor is consequently lower. The timescale of the heat transfer is several orders of magnitude lower than that of the flow-through time. Thus, assumptions of thermal equilibrium in cavitation models were quite successful in repeated modeling efforts [36] [48] [46].

If the enthalpy of the fluid is high, then the phase change is akin to a boiling process. The majority of the enthalpy needed for vaporization in the flash boiling mechanism is given by way of inter−phase heat transfer. With the increase in temperature, the density of saturated vapor increases. Similarly the rise in temperature corresponds to a decrease in the saturated liquid density. As a result of this trend, the amount energy to be provided by the liquid per unit volume of vapor generated is much higher than in typical cavitating flow despite the decrease in the enthalpy of vaporization. The dimensional analysis of Kato et al.[24] can help identify the relative magnitude of inertial versus thermal rates in phase change.

Kato et al. [24] analytically studied similar thermal effects which limited the growth rate of bubbles in liquids. They calculated rate of formation of vapor as a function of the energy transfer at the interface. Kato et al. found that two non-

dimensional parameters, the Jakob number, Ja, and non-dimensional time $t*$ played an important role in the vaporization. The Jakob number is defined as,

$$Ja = \frac{\rho_l c_p \Delta T}{\rho_v h_{fg}} \tag{2.1}$$

where ΔT is the degree of superheat and h_{fg} is latent heat of vaporization. The Jakob number is ratio of the amount sensible heat available to the amount of energy required for vaporization. The non-dimensional time is given by the following expression, where k is the thermal diffusivity of the liquid.

$$t* = \frac{t\Delta P}{k\rho_l} \tag{2.2}$$

The study revealed that for large Jakob number and non-dimensional time, the inertial effects dominate and vice versa when they are small, the physics are mainly guided by thermal effects. In processes where cavitation occurs the Ja and $t*$ are quite large, whereas in problems with flash boiling involved they are significantly smaller such that thermal effects need to be considered. This necessitates the use of a finite rate heat transfer process where the system is not in thermodynamic equilibrium but rather relaxes to it over a fixed time.

2.1 Modeling Approaches

Once it is decided to pursue modeling of thermal non-equilibrium, one must next decide whether to employ a full two-phase solution with separate transport equations or a pseudo-fluid approach where the mixture of phases is represented by a continuous density variable. The former approach offers complete generality, including separate velocities for each phase, while the latter approach offers relative simplicity and expediency. For an example of one-dimensional modeling using separate conservation equations for each phase, see Boure et al. [16].

For the current investigation, the pseudo-fluid approach was employed. Though the inclusion of slip has been shown to be important by Moody [34] and by Henry and Fauske [19] in one-dimensional analyses, the pseudo-fluid approach still allows relative velocity between the phases on the resolved scales in multi-dimensional CFD. For this reason, a no-slip model is less restrictive in higher dimensions than in one dimension. For example, an annular flow might have low speed vapor surrounding a high speed liquid core, which can be resolved with a no-slip model in two dimensions. Some of the limitations of this sub-grid no-slip assumption will be investigated in the results.

A benefit of the pseudo-fluid approach without assumption of slip is that no explicit model for interphase drag is required. By taking the limit of infinitely fast momentum exchange, one avoids the numerical problems of very high-drag rates and tight coupling between phase velocities, such as high computational cost and problems with numerical instability. The main risk of using the pseudo-fluid approach is that that interphase momentum transfer will be over-predicted.

Given the assumption of no sub-grid slip, the emphasis then shifts to the thermal non-equilibrium modeling. A successful example of such an approach is the work of Valero and Parra [57], who employed an "Equal Velocity Unequal Temperature" for modeling one-dimensional critical two-phase flow. They closed the basic conservation equations using a model of heat and mass transfer from spherical bubbles. They investigated their model predictions for short nozzles and found that a modification to include the effects of bubble nuclei was necessary. Their modified model was able to reliably match mass flow rate measurements in nozzles with length-to-diameter ratios from 0.3 to 3.6.

In the current work, detailed models of interfacial area, convection coefficient, and temperature field in the turbulent, two-phase heat transfer process are not employed. Given the nearly intractable complexity of the detailed heat transfer process, it is

pragmatic to rely on an empirical model that encapsulates the physics in simple correlation. The initial nuclei size and number density are not usually available, nor is the assumption of spherical bubbles always justifiable. As an alternative means of closure, the Homogenous Relaxation model [11] is employed. Like most proposed closures for two-phase channel flow, this model was originally developed for flow in one dimension and has been mostly explored only for one-dimensional scenarios. Duan et al. [12] employed the Homogenous Relaxation model in simulating the evolution of external multidimensional flow in a Lagrangian particle simulation. However, the correlation used by Duan et al. is several orders of magnitude slower than the original correlation of Downar-Zapolski et al. The present work explores the flashing nozzle behavior in multiple dimensional channel flow by constructing an Eulerian computational fluid dynamics code around the Homogenous Relaxation model.

There is some reason to believe that such an extension of a one-dimensional closure to multiple dimensions could be possible. Minato et al. [33] used a simple one-dimensional non-equilibrium two-phase flow analysis to close a two-fluid, two-dimensional, model of flashing flow. Their approach was quite computationally expensive, limiting their investigation to extremely coarse meshes. This initial study has garnered no attention from other researchers (as measured by subsequent citations) and has not prompted any further studies in this area in the fourteen intervening years since its publication. Given the limited computational resources of the time, the ability to calculate two-dimensional flashing flow, even on their very coarse mesh, is most remarkable.

The present work investigates the potential of extending the one-dimensional HRM approach to multiple dimensions, for use as closure of a multi-dimensional CFD code. In contrast to Minato, this model neglects interphase slip on the sub-grid scale and uses a pseudo-fluid approach, saving the computational cost of solving separate momentum equations. The success of this approach will offer new possibilities for multi-

dimensional simulation of flash-boiling flow. The challenge will be constructing a stable coupling between the HRM closure and the basic conservation equations.

CHAPTER 3

GOVERNING EQUATIONS

The flash-boiling internal flow model presented here relies on basic conservation laws. Given the assumption of no slip within a cell, the the pseudo-fluid approach produces the same basic conservation laws as for a single fluid. These are given below for conservation of mass, momentum, and energy. In the following equations, the variable ϕ represents the mass flux and τ is the stress tensor. In the present study, only laminar flow is considered, but the stress tensor does include Stokes' hypothesis for treating the second coefficient of viscosity.

$$\frac{\partial \rho}{\partial t} + \nabla \cdot \phi = 0 \tag{3.1}$$

$$\frac{\partial \rho U}{\partial t} + \nabla \cdot (\phi U) = -\nabla p + \nabla \cdot \overrightarrow{\overrightarrow{\tau}} \tag{3.2}$$

The energy equation is included, even though it is of little significance in the current work. All the simulations in the current study were run under adiabatic conditions and simulations proceed until a steady-state is reached. Hence, total enthalpy will be constant in these limits. However, in order to guarantee time–accuracy, an equation for energy or enthalpy is required. The following form is used, neglecting the kinetic energy of the fluid, viscous energy dissipation, and conduction.

$$\frac{(\partial \rho h)}{\partial t} + \nabla \cdot (\phi h) = \frac{\partial p}{\partial t} + \vec{U} \cdot \nabla p \tag{3.3}$$

Equations 3.1, 3.2, 3.3 are not a closed system. In single-phase flow, an equation of state would be required. However, where non-equilibrium heat transfer governs much

of the flow dynamics, there is no equation of state that would suffice. The two-phase mixture represented by the pseudo-fluid assumption is not in thermodynamic equilibrium. As explained above, our hypothesis is that a relaxation to equilibrium would be an appropriate model for closing the equations. For this purpose,the Homogenous Relaxation Model is employed.

3.1 Homogeneous Relaxation Model

The Homogenous Relaxation Model is based on a linearized expansion proposed by Bilicki and Kestin [3]. The general model form originates with refrigeration modeling by Einstein [14]. It has been used by numerous others for one-dimensional two-phase flow. The model represents the enormously complex process by which the two phases exchange heat and mass. The model form determines the total derivative of quality, the mass fraction of vapor.

$$\frac{Dx}{Dt} = \frac{\overline{x} - x}{\Theta} \tag{3.4}$$

Equation 3.4 describes the exponential relaxation of the quality, x, to the equilibrium quality, $\overline{x}$, over a timescale, Θ. The equilibrium quality is a function of the enthalpy and the saturation enthalpies at the local pressure, as given by Eq. 3.5 with bounds at zero and unity.

$$\overline{x} = \frac{h - h_l}{h_v - h_l} \tag{3.5}$$

The quality, the mass fraction of vapor, is calculated from each cell's void fraction, α for densities falling inside the saturation dome.

$$x = \frac{\alpha \rho_v}{\rho} \tag{3.6}$$

The void fraction in the two-phase region is, in turn, a function of the local density as well as the saturated vapor and liquid densities at the local pressure.

$$\alpha = \frac{\rho_l - \rho}{\rho_l - \rho_v} \tag{3.7}$$

The timescale in Eqn. 3.4 is empirically fit to data describing flashing flow of water in long, straight pipes. The work of Downar-Zapolski et al. [11] provides two correlations, one recommended for relatively high pressures, above 10 bar, and a different correlation for lower pressures. In the low-pressure form, for upstream pressures below 10 bar, the best-fit values suggested by Downar-Zapolski et al. for for flashing water appear in Eqn. 3.8. The empirical parameters include Θ_0 and the two exponents . These values are $\Theta_0 = 6.51 \cdot 10^{-4}$ [s], $a = -0.257$, and $b = -2.24$.

$$\Theta = \Theta_0 \alpha^a \psi^b \tag{3.8}$$

The variable α represents the volume fraction of vapor and ψ is a dimensionless pressure difference between the local static pressure and the vapor pressure, as defined in Eqn. 3.9. The absolute value is used in the present work since the pressure in the domain can fall below the saturation pressure.

$$\psi = \left| \frac{p_{sat} - p}{p_{sat}} \right| \tag{3.9}$$

A slightly different fit is suggested for upstream pressures above 10 bar, as given by Eqn. 3.10.

$$\Theta = \Theta_0 \alpha^a \phi^b \tag{3.10}$$

The dimensionless pressure ϕ, defined in Eqn. 3.11, differs from the definition in Eqn. 3.9 by including the critical pressure p_c. The coefficient values in the high-pressure correlation, Eqn. 3.10 are $\Theta_0 = 3.84 \cdot 10^{-7}$ [s], $a = -0.54$, and $b = -1.76$. Another correlation that was explored was one with a mixed character. In this mode the indices for void fraction and non-dimensional presssure were from the high-pressure

correlation while Θ_0 was of the low pressure correlation. The effects of use of different correlations are presented in the numerical results chapter of this document.

$$\phi = \left| \frac{p_{sat} - p}{p_c - p_{sat}} \right| \tag{3.11}$$

In the present study, the flow at the channel inlets were pure liquid. With no vapor present, the phase change timescale would be unbounded and vaporization would never begin. To avoid numerical overflow and to provide a means of treating boiling incipiency, a very small lower bound of 10^{-15} was applied. In all likelihood, dissolved gasses could provide an incipient void fraction in excess of this value.

The correlations presented by Downar-Zapolski et al. are based on data obtained for water. The empirical constants for other fluids such as hydrocarbons will vary and the ones presented are used only as an initial guess. Currently experimental data for hydrocarbons is unavailable in literature, but the framework developed allows for tuning of these constants as and when such data becomes available.

If the continuity equation is used for solving for mixture density and conservation of momentum is used for velocity, then Eqn. 3.4 is primarily responsible for determining the pressure. In contrast to incompressible or low-Mach number Navier-Stokes solvers, the current model does not seek a pressure that projects velocity into consistency with the continuity equation. Instead, we solve for the pressure that satisfies the chain rule and employs the continuity equation indirectly. Through the chain rule, the pressure responds to both compressibility and density change due to phase change. The behavior of pressure is seen to be both hyperbolic and parabolic, while the phase change model appears as a source term. The description of the numerical technique used to solve this set of fundamental equations is presented in the next chapter.

CHAPTER 4

NUMERICAL APPROACH

In order to provide close coupling with velocity, the momentum equations and continuity equation are combined with Eqn. 3.4 to provide a pressure equation. The procedure starts with conservation of mass and momentum, Eqns. 3.1 and 3.2, respectively. The next step is to discretize the momentum equation. This discretization can take many forms, but they can all be represented generally using the form of Eqn.4.1.

$$a_p U_p = H(U) - \nabla p \tag{4.1}$$

This represents the discrete equation applied to each cell in the domain. The subscript p refers to the point of interest using the notation of Peric and Ferziger [18]. The H operator represents convection and diffusion as discretized equation coefficients multiplied by neighboring velocities plus source terms. The coefficient a_p is the coefficient term of the matrix of velocity equations.

The chain rule can also be used to express the total derivative of density, as in Eqn. 4.2. The chain rule stands in place of the typical equation of state, since this is a simulation of non-equilibrium fluid. Note that for thermodynamic non-equilibrium, density is a function of three variables: pressure, quality, and enthalpy [3].

$$\frac{D\rho}{Dt} = \frac{\partial \rho}{\partial p}\Big|_{x,h} \frac{Dp}{Dt} + \frac{\partial \rho}{\partial x}\Big|_{p,h} \frac{Dx}{Dt} + \frac{\partial \rho}{\partial h}\Big|_{p,x} \frac{Dh}{Dt} \tag{4.2}$$

Currently, the last term in Eqn. 4.2 is neglected due to the near-isenthalpic nature of the adiabatic channel flows currently considered. The first term on the right side,

represents a contribution to the density change due to two-phase compressibility. This two-phase compressibility is calculated as a mass average of the two single-phase compressibilities. This term could be significant in transonic flow. In cases where the two-phase compressibility is not significant, this term can be omitted, which offers the advantage of producing a symmetric matrix for the discretized pressure equations. Calculations where the compressibility was neglected are explicitly mentioned later.

If the conservation of mass, Eqn. 3.1, is subtracted from Eqn. 4.2 then the left side gives an expression for velocity divergence at the new time step.

$$-\rho\nabla\cdot U = \frac{\partial\rho}{\partial p}\Big|_{x,h}\frac{Dp}{Dt} + \frac{\partial\rho}{\partial x}\Big|_{p,h}\frac{Dx}{Dt} \tag{4.3}$$

Using Eqn. 4.1 and U_p in place of U, the momentum equation can be coupled with the chain rule to produce an equation for pressure.

$$\frac{\partial\rho}{\partial p}\Big|_{x,h}\frac{\partial p}{\partial t} + \frac{\partial\rho}{\partial p}\Big|_{x,h}(U\cdot\nabla p) + \rho\nabla\cdot\left(\frac{H}{a_p}\right) - \rho\nabla\frac{1}{a_p}\nabla p + \frac{\partial\rho}{\partial x}\Big|_{p,h}\frac{Dx}{Dt} = 0 \tag{4.4}$$

This is a mixed-character transient convection/diffusion equation. The transmission of pressure waves which is essential for any compressible flow calculation is allowed by the transient and convective terms in the equation while the pressure is kept in range and is damped by the Laplacian term. For low Mach number flows the terms containing $\frac{\partial\rho}{\partial p}\Big|_{x,h}$ can be dropped. The terms were retained for some calculations but dropped for other calculations since they change mass flow rate very little but slow the rate of solver convergence. Without the compressibility terms, the linear system is symmetric and can be solved with approximately half the cost of the full system of equations.

The attractive features of this pressure equation is that most of the terms are linear in p plus the model in Eqn. (1) can be inserted directly into the last term. In the limit

of constant density, an incompressible formulation is recovered. Schmidt et al. [47] used a similar idea (but neglecting the derivative of density with respect to pressure) in a two-step projection method on a staggered mesh approach. The implementation on a staggered mesh was well-suited for their two-dimensional structured grid solver. In order to facilitate the application of the current model to three-dimensional solutions with unstructured, polyhedral mesh support, the current implementation will use a collocated variable approach.

The first step in each time step is the solution of conservation of mass, Eqn. 4.5. This is done implicitly.

$$\frac{\partial \rho}{\partial t} + \nabla \cdot (\phi_v \rho) = 0 \tag{4.5}$$

Here, the volumetric flux, ϕ_v, is based on the velocity field from the previous time step, interpolated to cell faces. The new value of density from Eqn. 4.5 is interpolated to cell faces and a new mass flux ϕ is calculated. Next, the thermodynamic variables such as void fraction, quality, and compressibility are updated using the new value for density.

As in the PISO algorithm [21], the velocity field is predicted using a lagged pressure, indicated by the superscript n. The equation for this predicted velocity, U^0, is given in Eqn. 4.6. Later, when pressure is updated, the additional contribution from the change in pressure will be used as a corrector to the velocity field.

$$\frac{(\partial \rho U^0)}{\partial t} + \nabla \cdot \left(\phi U^0\right) = -\nabla p^n + \nabla \cdot \left(\mu \nabla U^0\right) \tag{4.6}$$

Equation 4.6 represents three linear systems of equations, one for each component of velocity, and is solved implicitly with the pressure gradient acting as an explicit source term, in the form of Eqn. 4.1.

The ratio of the off-diagonal terms to diagonal terms that appear in Eqn. 4.1 have dimensions of velocity and can be thought of as a velocity field prior to pressure projection, as indicated in Eqn. 4.7.

$$U^* = \frac{H}{a_p} \tag{4.7}$$

This velocity is interpolated to face centers to produce a flux field, ϕ^*, that is used in Eqn. 4.4.

With multiple PISO iterations, the non-linearity of the momentum equation can be accommodated. However, the phase change model presents an additional challenge: the last term in Eqn. 4.4, representing the effects of the phase-change model is highly non-linear and strongly dependent on pressure. As a shorthand, we define this term as M in Eqn. 4.8. Using linearization, the PISO iterations also provide secant method iterations for semi-implicitly including the pressure, as shown in Eqn. 4.4. The superscripts k and $k+1$ indicate the previous and current PISO iteration, respectively.

$$M \equiv \frac{\partial \rho}{\partial x}\Big|_{p,h} \left(\frac{\overline{x} - x}{\Theta} \right) \tag{4.8}$$

Typically, two to five PISO/secant iterations were employed, each requiring solution of the pressure equation. Without the compressibility terms, the linear system for pressure is symmetric, and is solved using a diagonal incomplete Cholesky preconditioned conjugate-gradient method. With the full pressure equation, a diagonal incomplete LU preconditioned bi-conjugate gradient is used. The non-orthogonal parts of the Laplacian are handled with a deferred correction approach that also benefits from the multiple iterations if the computational mesh is highly skewed [22]. Once Eqn. 4.4 has been solved, the pressure field is used to correct the fluxes and the time step is completed. The pressure must also be updated in the momentum equation. This is done by reconstructing the face-based pressure gradients into a

cell-centered gradient. This reconstruction process can produce spurious out-of-plane velocities in two-dimensions that are discarded.

This approach produces a set of equations that are solved on an arbitrary polyhedral mesh in two and three dimensions. The underlying framework is provided by OpenFOAM [63]. A detailed discussion of the software framework employed is presented in the subsequent chapter.

CHAPTER 5

SOFTWARE FRAMEWORK

The numerical model described in the preceding chapter is implemented in a framework called OpenFOAM [63]. OpenFOAM is an open source toolkit for continuum mechanics. It is developed in an object oriented framewrok using C++ and provides fundamentals classes for discretisation operators, linear algebra solvers, mesh handling capability etc. An overview of the structure of OpenFOAM is given in Fig.5.1.

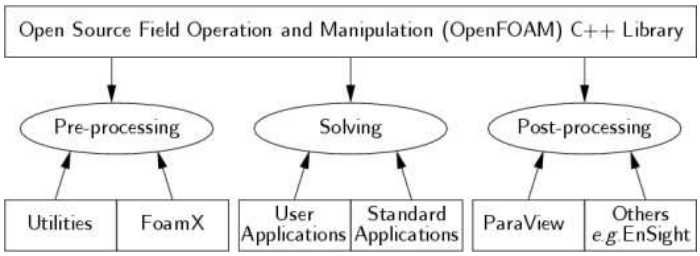

Figure 5.1. Structure of OpenFOAM [38]

The fundamental classes provided by OpenFOAM allows the rapid construction of numerical solvers for continuum mechanics solver.

5.1 Polyhedral Finite Volume Method

The computational domain is divided into several computational cells which form control volumes over which the governing PDE's are discretised. The control volumes can be aribitrary polyhedra in three dimensional space. A computational cell (control volume) can have any number of faces. This offers a lot of geometric freedom during the mesh generation phase of any CFD calculation and enables the resolution of complex geometries.

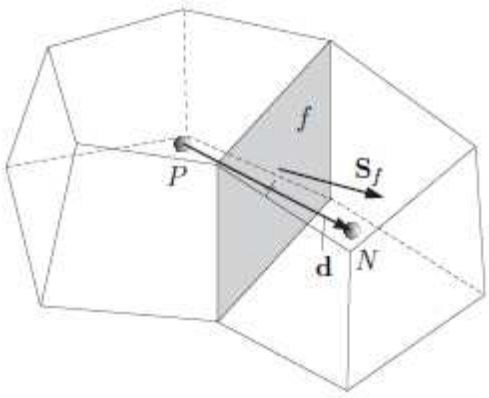

Figure 5.2. Finite Volume Discretisation [38]

Fig.5.2 describes a generic cell with its cell centroid at the point P. The neigboring cell centroid is denoted by the point N. Typically the dependant variables for the calculation are stored at cell centers, but they also can be stored on faces. The face between the two cells is denoted as f with S_f being the surface area vector of the face. All internal faces will be connected to two cells designated as owner and neighbor. Boundary faces are part of the boundary of the computational domain and are connected only to one cell.

5.2 Discretisation Operators

The spatial derivative terms in any PDE are converted to an integral form using Gauss's theorem. The modified form is then discretised on the computational mesh.

$$\int_V \nabla \cdot \phi dV = \int_S dS \cdot \phi \tag{5.1}$$

where ϕ is any tensor field and S is the surface area vector.

For simplicity's sake we will consider the terms in the momentum equation referred in equation 4.6.

5.2.1 Convection Term

$$\int_V \nabla \cdot (\phi U) dV = \int_S dS \cdot (\phi U) = \sum_f S_f \cdot (U)_f \phi_f = \sum_f F \phi_f \tag{5.2}$$

The face flux field ϕ_f has the following methods of evaluation.

Central differencing scheme (CDS) which is second order accurate.

$$\phi_f = f_x \phi_P + (1 - f_x)\phi_N \tag{5.3}$$

where $f_x = \overline{FN}/\overline{PN}$ where $\overline{FN}$ is distance between face center of f and the cell center N. Similarly the $\overline{PN}$ is the distance between the cell centers P and N. The central difference scheme is unbounded in nature which can lead to stability issues.

An Upwind Scheme (UDS) which depends only on the direction of the flow is first order accurate but will be bounded and hence offer better stability. For the upwind scheme ϕ_f takes the following form,

$$\phi_f = \phi_P, \text{ for } F > 0 \tag{5.4}$$

$$\phi_f = \phi_N, \text{ for } F < 0 \tag{5.5}$$

A Blended Difference Scheme (BDS) combines both the CDS and UDS to provided stability with reasonable accuracy.

$$\phi_f = (1 - \gamma)(\phi_f)_{UDS} + \gamma(\phi_f)_{CDS} \tag{5.6}$$

where γ is the blending coefficient.

5.2.2 Gradient Term

The explicit gradient term can be evaluated in a couple of different ways. A simple approach will be to employ Gauss's theorem.

$$\int_V \nabla p dV = \int_S dS \cdot p = \sum_S S_f p_f \tag{5.7}$$

This method interpolates the pressure from the cell centers to the faces and then evaluates the gradient based on the face values. This technique is prone to numerical errors when employed highly non–orthogonal grids.

To alleviate this, a least squares approach is quite useful. The basic idea of the least square approach is minimise the error at every neighboring cell if the variable of interest was to be extrapolated on the basis of the gradient at cell center P

Initally a tensor $\mathbf{G}$ is computed on the basis of,

$$\mathbf{G} = \sum_N w_N^2 \bar{d}\bar{d} \tag{5.8}$$

where $\bar{d}$ is the vector from P to N and w_n is a weighting function which is typically chosen as $1/\left|\bar{d}\right|$. The gradient is then given as,

$$(\nabla p)_P = \sum_N w_n^2 \mathbf{G}^{-1} \cdot \bar{d}(P_n - P_P) \tag{5.9}$$

5.2.3 Laplacian

The laplacian term is integrated over the control volume as follows,

$$\int_V \nabla \cdot (\mu \nabla U) dV = \int_S dS \cdot (\mu \nabla U) = \sum_f \mu_f S_f \cdot (\nabla U)_f \tag{5.10}$$

where S_f is the surface area vector and,

$$\sum_f S_f \cdot (\nabla U)_f = |S_f| \frac{U_n - U_p}{\left|\bar{d}\right|} \tag{5.11}$$

5.2.4 Time Derivative

The time derivative term is given as,$\frac{\partial}{\partial t} \int_V \rho U$

A Euler implicit scheme which is first order accurate in time is provided as follows,

$$\frac{\partial}{\partial t}\int_V \rho U = \frac{(\rho_P U_P V)^n - (\rho_p U_p V)^o}{\delta t} \tag{5.12}$$

where the subscript n stands for the current timestep and the subscript o is the previous timestep.

5.3 Boundary Conditions

Mathematically, boundary conditions can be fundamentally described as two types,

- Dirichlet boundary condition - This provides a fixed value for the scalar variable of interest at the boundary. It can be directly applied to the boundary faces. If the gradient of the variable is needed, then a gradient based of on the boundary face value and cell centre value is computed.

$$S_f \cdot (\nabla\phi)_f = |S_f| \frac{\phi_P - \phi_f}{\left|\bar{d}\right|} \tag{5.13}$$

  where ϕ is the variable of interest.

- Neumann boundary condition - Here the boundary condition is specified in terms of a gradient. If the boundary condition is required in terms of the gradient, then it can be directly substituted. If a value is required at the boundary face then it is calculated based on the gradient and the cell centre value.

$$\phi_f = \phi_P + \bar{d} \cdot \bar{g_B} \tag{5.14}$$

  where $\bar{g_B}$ is gradient specified at the boundary condition.

Once the discrete set of equations are formed and the associated boundary conditions are applied, they can be expressed as a system in the matrix form.

$$[A]\,[x] = [b] \tag{5.15}$$

where $[x]$ is a vector of the dependant variable of interest. $[A]$ is square matrix with the coefficients for the linear algebra system and $[b]$ is the source vector. The system of equations can be solved using any solver of simultaneous equations. OpenFOAM provides a variety of linear algebra solvers and associated preconditioners, such as Preconditioned Conjugate Gradient, Biconjugate Gradient, Geometric Multigrid etc.

The software framework is also fully parallelized in three dimensions using the Message Passing Interface (MPI). Sophisticated decomposition tools employing graph partitioning routines such as METIS [23] are provided to ensure proper load balancing.

CHAPTER 6

ATOMIZATION AND BREAKUP MODELS

The internal flow model discussed in the previous chapter successfully models the thermal non-equlibrium of the superheated fluid flowing through the injector nozzle. If the degree of superheat is high enough then it is possible that at the injector exit the liquid is still in themal non-equilibrium. This chapter deals with atomization and secondary breakup of superheated fluid.

The methodology used in both the primary atomization and the secondary breakup models is thus: two simultaneous competing processes are coupled and which ever reaches its respective critical condition first dictates the mode of atomization. In the case of primary atomization, the surface instability mode competes with the non-equilibrium vaporization of the core (which is modeled with HRM). Both dynamic systems are integrated in a coupled manner, and the process which satisfies its breakup criterion first is the one used to predict the properties of the daughter droplets. Similarly, for the secondary breakup, the TAB model competes with HRM to predict breakup and final drop sizes.

Fig.6.1 visualizes the concepts of the dual model atomization model. It combines the phenomena of aerodynamic instability and flashing. Once again, the use of the term *instabilty atomization* to refers to the atomization mechanism that is driven by the aerodynamic instability occurring between the liquid core and the air; and *flash atomization* to refer to the atomization mechanism driven by the relaxation of the superheated liquid core. In the current application, for the primary and secondary atomization, the Linearized Instability Sheet Atomization (LISA) model [52, 45] and

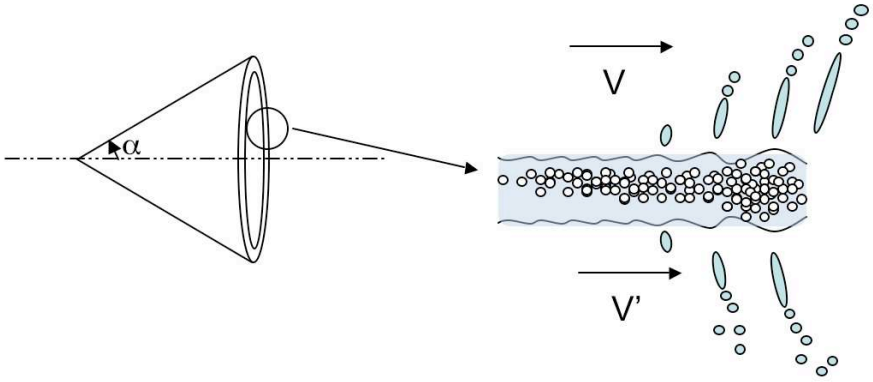

Figure 6.1. Atomization of a superheated jet is brought about by two distinct but coupled phenomena: instability at the jet/air interface and the rapid evaporation of the superheated liquid.

the Taylor Analogy Breakup (TAB) Model [39] are used as the basis for the instability atomization mode. As for the flash atomization mode, the Homogeneous Relaxation Model (HRM) was utilized.

6.1 Linearized Instability Sheet Analysis

The dynamics model used here is identical to the one described earlier by Schmidt *et al.* [52, 45]. The only modification required is the evaluation of the jet core properties. They are taken to be the average of the respective properties of the two phases of the fluid with the quality (vapor mass fraction) used as the weighting factor. For example, as the superheated fluid vaporizes, the overall density of the core is taken to be the harmonic mean of the values of the liquid and vapor density weighted by $x(t)$. The properties of the core are obviously time dependent as they are algebraic functions of $x(t)$ which is obtained by integrating Eqn. (3.4).

For the instability atomization mode (LISA), the breakup length or time τ is determined by the maximum growth rate of a disturbance at the liquid-vapor interface.

Aerodynamic instability will atomize the core when this disturbance on the interface grows to a critical value.

The dispersion relation for the primary shear instability breakup as derived in [45] is

$$\begin{aligned}\omega^2(tanh(kh)+Q) &+ \omega\left[4\nu_l k^2 tanh(kh)+2iQkU\right]+4{\nu_l}^2k^4tanh(kh)\\ &- \left(4\nu_l^2k^3Ł\right)tanh(Ł h)-QU^2k^2+\frac{\sigma k^3}{\rho_l}=0\end{aligned} \tag{6.1}$$

In Eqn. (6.1), U denotes the velocity of the gas relative to the liquid core, Q the gas to liquid density ratio $\frac{\rho_g}{\rho_l}$, h the half-thickness of the liquid core, and k the wave number of the disturbance; also $Ł=\sqrt{k^2+\omega/\nu_l}$. After dropping second order terms, the growth rate for the sinuous mode is given by

$$\omega_r=\frac{-2\nu_l k^2 tanh(kh)+\{4\nu_l^2k^4-Q^2U^2k^2-(tanh(kh)+Q)(-QU^2k^2+\sigma k^3/\rho_l)\}^{-1/2}}{tanh(kh)+Q} \tag{6.2}$$

In Eqn. (6.2), there are two possible solutions: long and short waves [45]. For the current application, we assume only the short wave solution. Equation (6.2) can then be further simplified into

$$\omega_r=-2\nu_l k^2+\sqrt{4\nu_l^2k^4+QU^2k^2-\frac{\sigma k^3}{\rho_l}} \tag{6.3}$$

Eqn. (6.3) was solved for the most unstable growth rate which is denoted by Ω (i.e., the maximum value of $|\omega_r|$). Eqn. (6.3) indicates that this maximum growth rate is dependent on the physical properties of the two phase core and thus is dependent on time or equivalently the length along the core (after a Galilean transformation to the moving coordinate of the core).

It is assumed that when the perturbation associated with this most unstable mode grows to a certain extent (this being a model tuning parameter), breakup occurs. This extent is described by logarithm of the ratio of the disturbance and its initial value i.e. $ln\frac{\eta_b}{\eta_o}$. Following the original work of Dombrowski and Hooper [9], a critical value of 12 was set such that when $ln\frac{\eta_b}{\eta_o} = 12$, instability induced breakup, or atomization occurs. With this, the breakup length is simply given by

$$L = U\tau = \frac{U}{\Omega} ln(\frac{\eta_b}{\eta_o}) \tag{6.4}$$

where Ω is maximum growth rate. η_b and η_o are the initial and final wave amplitudes.

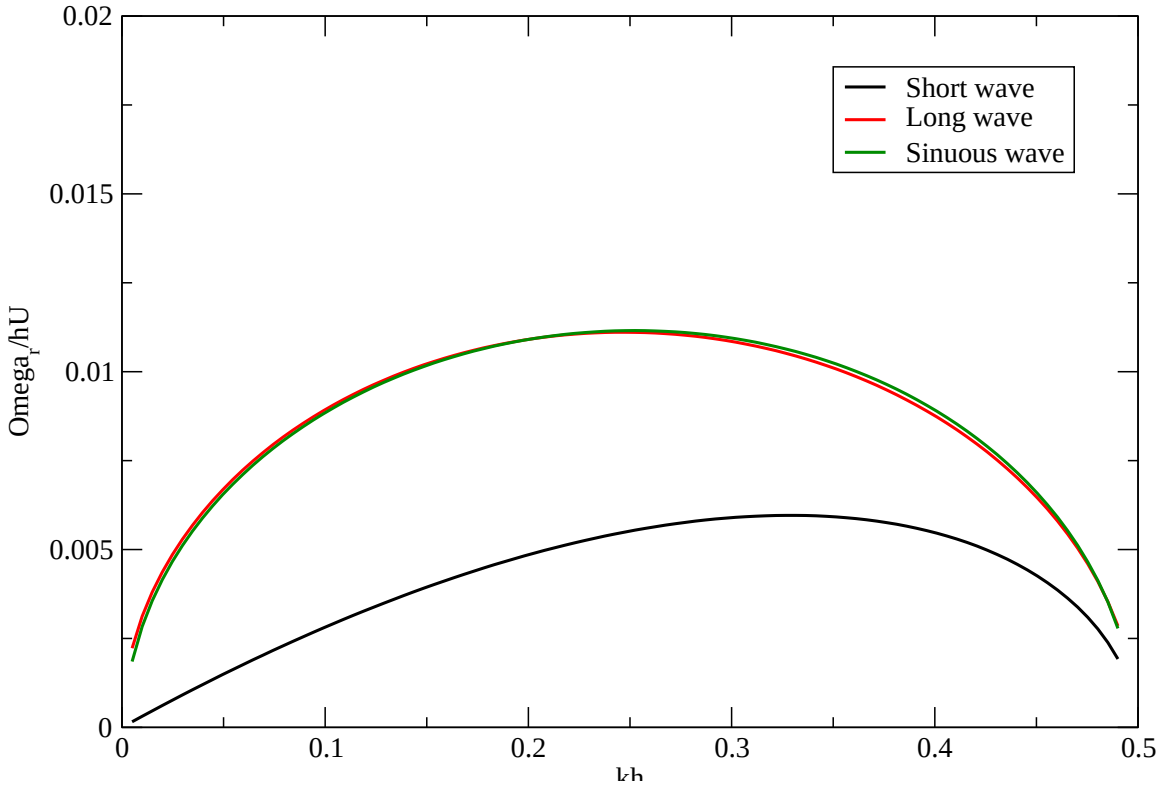

Figure 6.2. Non−dimensional growth rate versus non−dimensional wave number We = 0.5

The ligament diameter at break up depends on whether we are in the long wave, short wave or surface wave regimes. If the wavelength of the disturbance is higher

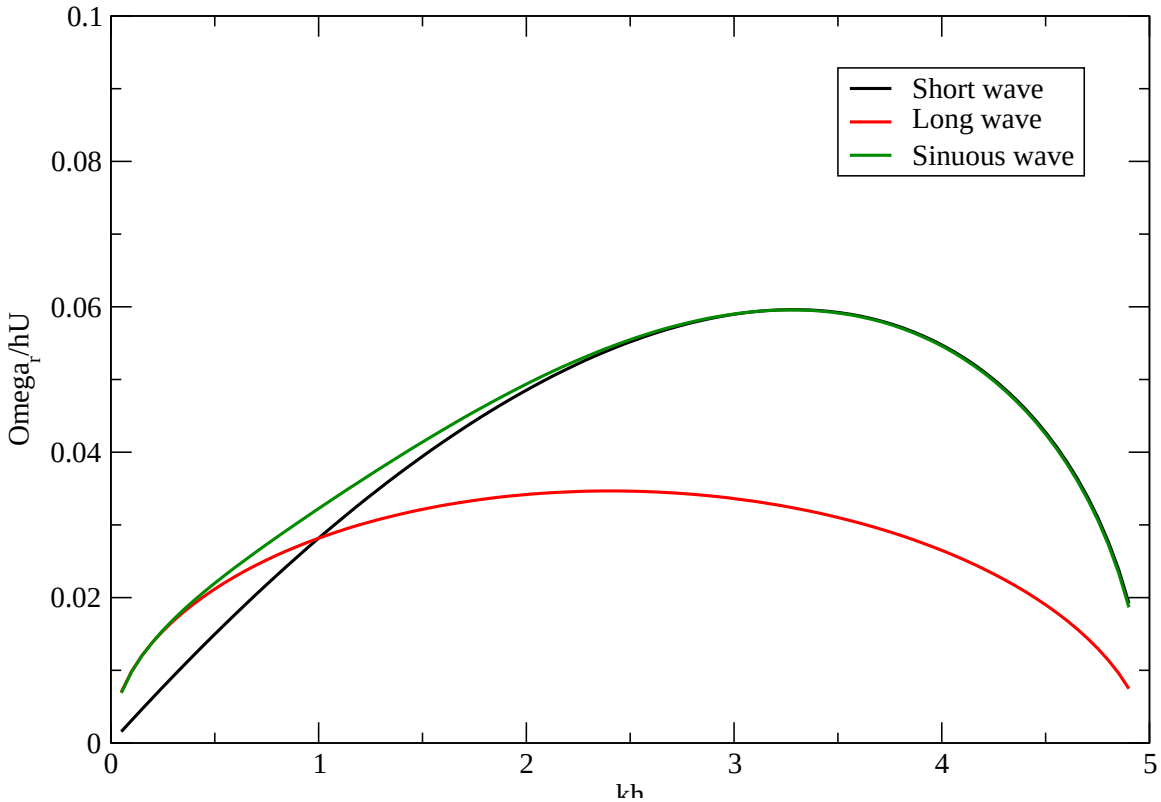

Figure 6.3. Non−dimensional growth rate versus non−dimensional wave number We = 5.0

than the half sheet thickness, it is assumed that long wave growth exists. Otherwise short wave solution is imposed. The ligament diameter for long waves is calculated as,

$$d_L = \sqrt{\frac{8h}{K_s}} \tag{6.5}$$

where h is the half sheet thickness at breakup, K_s is the wave number of maximum wave growth. For short waves the the ligament diameter is,

$$d_L = \sqrt{\frac{16h}{K_s}} \tag{6.6}$$

If the Weber number is sufficiently high, then only surface waves exist which are independent of the sheet thickness. The transition to surface waves in this study is assumed to occur at a Weber number of 50. The ligament diameter of the surface wave is assumed to be half the wavelength.

$$d_L = \frac{\pi}{K_s} \tag{6.7}$$

The drop diameter is obtained from the ligament diameter via the following relation which is obtained by a mass balance,

$$d_D^3 = \frac{3\pi d_L^2}{K_L} \tag{6.8}$$

Where K_L is given as ,

$$K_L d_L = \left(\frac{1}{2} + \frac{3\mu_l}{2\sqrt{\rho_l \sigma d_L}}\right)^{-0.5} \tag{6.9}$$

6.1.1 Derivation of Sheet Thickness

The instantaneous sinuous wave growth rate is based on the the current thickness of the conical liquid sheet. Additionally, at breakup, the ligament diameter depends

upon the sheet thickness at the instance of breakup. This necessitates the computation and tracking of the sheet thickness and is done using conservation of mass. The derivation for the expression of the current sheet thickness, h_s is given below.

The variable $\dot{m}$ is the mass flow rate of the nozzle, h_0 the initial sheet thickness, d_i the inner diameter of the nozzle, ρ the density of the liquid, U the velocity of the sheet, θ the cone angle and L is the distance along the sheet.

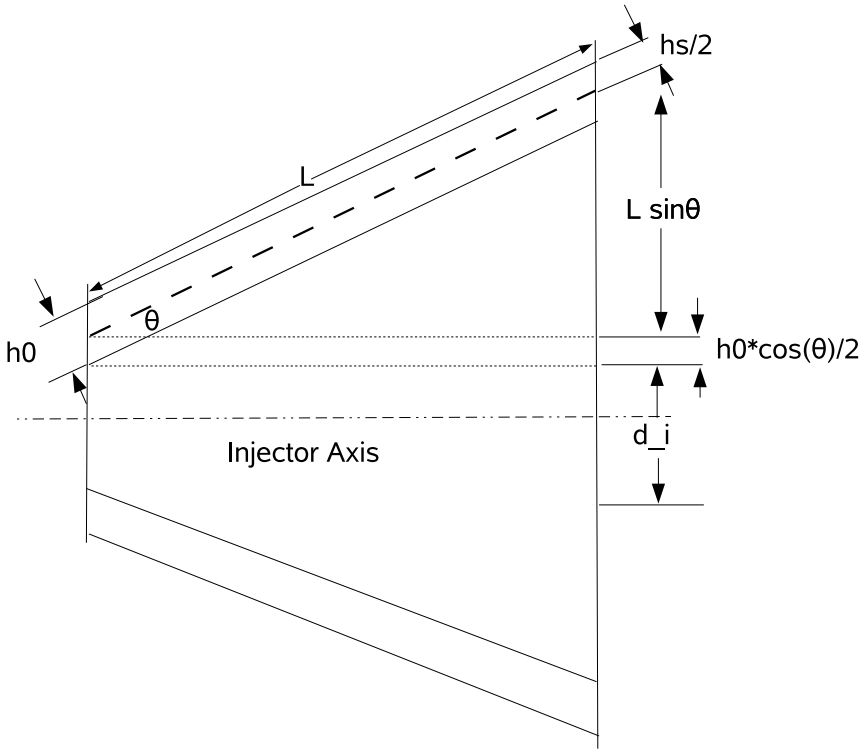

Figure 6.4. Conical sheet at an angle θ

$$R_o = Lsin\theta + \frac{d_i + \left(\frac{h_0}{cos\theta}\right) + \left(\frac{h_s}{cos\theta}\right)}{2} \tag{6.10}$$

$$R_i = Lsin\theta + \frac{d_i + \left(\frac{h_0}{cos\theta}\right) - \left(\frac{h_s}{cos\theta}\right)}{2} \tag{6.11}$$

$$\dot{m} = \rho U_{liq} cos(\theta)\pi((R_o)^2 - (R_i)^2) \tag{6.12}$$

$$\frac{\dot{m}}{\rho U_{liq} cos(\theta)\pi} = (Lsin\theta + \frac{d_i + \left(\frac{h_0}{cos\theta}\right) + \left(\frac{h_s}{cos\theta}\right)}{2})^2 - (Lsin\theta + \frac{d_i + \left(\frac{h_0}{cos\theta}\right) - \left(\frac{h_s}{cos\theta}\right)}{2})^2 \tag{6.13}$$

$$\frac{\dot{m}}{\rho U_{liq} cos(\theta)\pi} = 2\left(\frac{h_s}{cos\theta}\right) Lsin\theta + \left(\frac{h_0}{cos\theta}\right)\left(\frac{h_s}{cos\theta}\right) + d_i\left(\frac{h_s}{cos\theta}\right) \tag{6.14}$$

$$\left(\frac{h_s}{cos\theta}\right) = \frac{\dot{m}}{\rho U_{liq} cos(\theta)\pi(2Lsin\theta + \left(\frac{h_0}{cos\theta}\right) + d_i)} \tag{6.15}$$

$$h_s = \frac{\dot{m}}{\rho U_{liq}\pi(2Lsin\theta + \left(\frac{h_0}{cos\theta}\right) + d_i)} \tag{6.16}$$

6.1.2 Cylindrical Jet

The LISA model cannot be strictly applied to cylindrical jet breakup. For plain orifice injectors, the jet emanating from the nozzle is cylindrical in shape. The fundamental nature of the wave disturbances which cause the breakup of the liquid sheet are of a similar nature to that of a liquid cylinder. The analytical solution to the wavelengths at which maximum disturbance growth occurs for a cylinder differs from that used for a liquid sheet and has been provided by Reitz [42]. The expressions for the drop sizes after jet breakup are fundamentally different as well. The primary atomization model is designed to switch to the cylindrical jet breakup solution if the injector cone angle is 0, i.e a straight jet.

The model used for the process of cylindrical jet breakup is as given by Reitz [42]. The wave length of the most unstable wave is given by equation 6.17

$$\frac{\Lambda}{a} = 9.02\frac{(1+0.45Z^{0.5})(1+0.4T^{0.7})}{(1+0.87We_2^{1.67})^{0.6}} \tag{6.17}$$

The growth rate of the most unstable wave is equation 6.18.

$$\Omega[\frac{\rho_1 a^3}{\sigma}]^{0.5} = \frac{0.34+0.38We_2^{1.5}}{(1+Z)(1+1.4T^{0.6})} \tag{6.18}$$

where,

$$Z = \frac{We_1^{0.5}}{Re_1},\ T = ZWe_2^{0.5} \tag{6.19}$$

We_1 and Re_1 are the liquid phase Weber and Reynolds number respectively. We_2 is the gas phase weber number.

The breakup criterion for the jet was the same as the LISA model. The drop radius predicted the by the model are given by equations 6.20 and 6.21. The criteria for the switch is based on $B_0\Lambda$ and a. B_0 is a constant assumed to be 0.61 and a is the initial blob radius.

$$r = B_0\Lambda \ \ (B_0\Lambda \leq a) \tag{6.20}$$

$$r = min\begin{bmatrix} (\frac{3\pi a^2 U}{2\Omega})^{0.33} \\ \\ (\frac{3a^2\Lambda}{4})^{0.33} \end{bmatrix} \ \ (B_0\Lambda > a) \tag{6.21}$$

For the primary atomization model, the Homogeneous Relaxation Model (HRM) is coupled with the sheet atomization model (LISA) and the cylindrical jet breakup model (Reitz). The thermodynamic relaxation process competes with instability growth model in a race to achieve the breakup criterion.

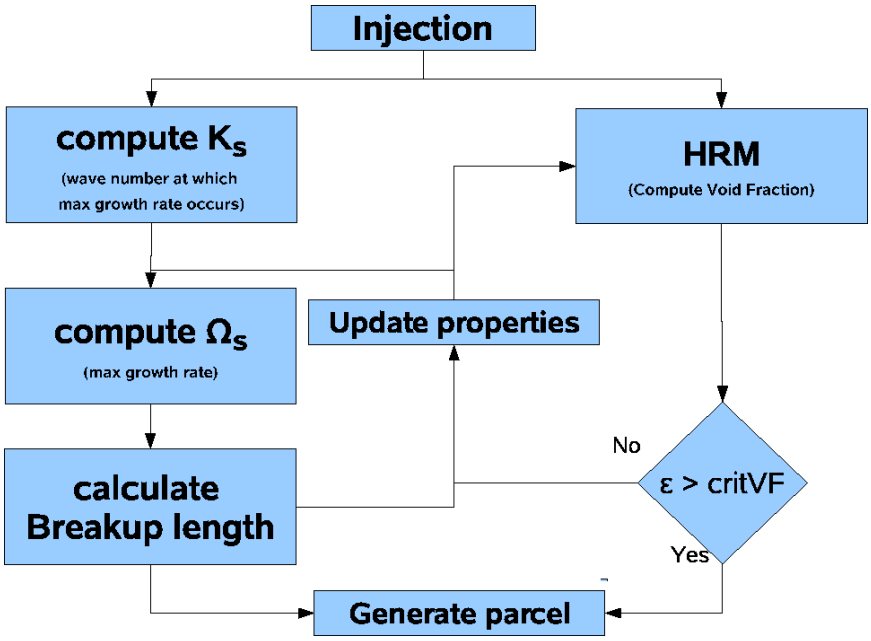

Figure 6.5. Flowchart for coupled HRMLISA

As described in the flowchart as given in Fig.6.5, for every injection, the HRM rate equation is tracked simultaneously with the wave growth model. The breakup length from the wave growth model is continously updated with the time integrated void fraction and the corresponding thermophysical properties. Breakup is said to occur when either the breakup length has been reached or the critical void fraction has been exceeded.

In Eqn. (6.4), the breakup length L and the breakup time τ are related by the relative velocity. The flashing of the fluid is coupled to the instability breakup mode using this expression. The HRM expression (6.22) is handled with a time integrator . At each time step $t = t_i$, the void fraction $\epsilon(t_i)$ is evaluated with Eqn. 6.23 using the value of $x(t_i)$, and we check if the critical value is reached ($\epsilon_c = 0.61$). The value of $x(t_i)$ is also used to evaluate the physical properties that are needed in evaluating the breakup length in Eqn. (6.4). Then the breakup time defined in Eqn. (6.4) is compared with the current time step t_i. If $\tau > t_i$ and $\epsilon(t_i) \geq \epsilon_c$, then flash atomization occurs. If $\tau \leq t_i$ and $\epsilon(t_i) < \epsilon_c$, then instability is responsible for the primary breakup. If

none of these two conditions are met, the time integration continues. Depending on which physical phenomenon is responsible for the primary breakup, the appropriate submodel that describes the droplet number density will be used.

When this breakup time is shorter then the time required for the superheated liquid to reach the critical void fraction, the instability breakup mode takes over the atomization process. If flashing reaches its critical condition sooner, then, it becomes the atomization mechanism. For the flash atomization mode, the breakup criteria is the critical void fraction. Senda et al. [51] and Kawano et al. [26], in their work on superheated gasoline, discovered that the primary core flash atomization occurs when the void fraction (vapor volume fraction) reaches a value of 0.61 *ca.* In a related work of Zeng and Lee [67], a more elaborate model for an isolated superheated droplet also yielded a similar criticality condition for a wide range of conditions. Sher and Elata [53], who worked on aerosols, concluded that this critical void fraction is related to the packing limit of spheres in a volume i.e. the maximum number of identical spheres that can be packed in a given volume [5]. There are many theories on the evaluation of this packing limit, but in three dimensions they all predict a volume ratio of approximately in the range of 0.6 to 0.7. The physical reasoning of this criticality is obvious: when the core cannot accommodate any more bubbles, it shatters - the geometry changes from "bubbles-in-liquid" to "droplets-in-vapor".

The dual mode model as described, mathematically, is formulated in the following way. First we construct the model that describes the time variation of the void fraction using the HRM by combining equations (3.4) and (6.23). These, together with the critical void fraction as the break up criteria, complete the main part of the flash atomization component. What remains is the model that describes the droplet number density subsequent to the flash atomization process which is discussed in the next section. Note that the same flash atomization model is used in both the primary and the secondary breakup processes.

6.2 Homogenous Relaxation Model

The non−equilibrium phase change process is tracked by the Homogenous Relaxation Model [10] . The rate of vapor formation is given by,

$$\frac{dx}{dt} = \frac{x^{eq} - x}{\Theta}; \quad \Theta = \Theta_o \epsilon^{\alpha} \phi^{\beta}; \ \alpha = -0.54; \ \beta = -1.76; \ \Theta_o = 6.51e^{-4}[s] \tag{6.22}$$

where in $x^{eq}(p, h)$ denotes the equilibrium quality; α, β, and Θ_o are model constants. ϵ and ϕ denote, respectively, the void fraction and the degree of superheat of the system.

$$\epsilon = \frac{\rho_l - \rho}{\rho_l - \rho_v}; \quad \phi = \frac{P_b(h) - P}{P_c - P_b(h)} \tag{6.23}$$

P_c is the critical pressure of the fluid. $P_b(h)$ is the bubble point pressure of the system for the particular enthalpy. The void fraction is tracked along with the HRM rate equation. The sheet is assumed to breakup when the void fraction reaches a critical value of 0.6.

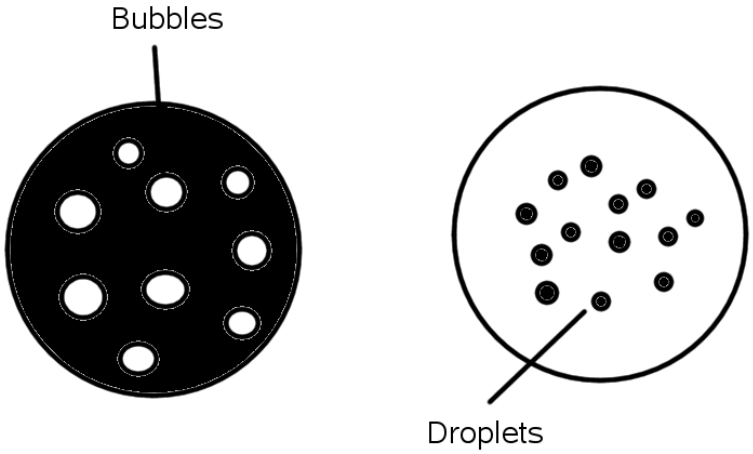

Figure 6.6. Bubble growth and subsequent breakup into droplets

The number of nucleation sites for bubbles is obtained from a relation provided by Senda et al [51]. The nucleation density is a function of the degree of superheat of the fluid which is denoted as $\delta\theta$.

$$N = C \cdot e^{-5.279d0/\delta\theta} \tag{6.24}$$

The constant C is assumed to have a value of $5.757 * 10^{12}$ as reported by Senda et al [51]. The droplet diameter for flash induced breakup is purely based on thermodynamic quantities and is given as,

$$D = 2 \cdot (\frac{1-\epsilon}{\frac{8}{3}\pi N})^{1/3} \tag{6.25}$$

where ϵ is the void fraction. It is assumed that for every bubble two daughter droplets will be formed as given by Senda et al[51].

6.3 Taylor Analogy Breakup

The secondary breakup model was constructed similarly to the primary atomization model. The Taylor Analogy Breakup (TAB) model [39] and the HRM were combined. The TAB model describes the perturbation of a droplet from its initial spherical shape using a single parameter y, which denotes the deformation of the single droplet.

$$\rho_l R^3 \ddot{y} = C_F/C_b \rho_g U^2 R - C_K \sigma y - C_d \mu_l \dot{y} R \tag{6.26}$$

In Eqn. (6.26), U denotes the droplet velocity relative to the ambient, R the droplet radius, y the normalized droplet shape perturbation, σ the surface tension, μ_l the viscosity of the two-phase fluid within the droplet, ρ_l the density of the two-phase fluid within the droplet, and ρ_g the density of the ambient gas. C_F, C_b, C_K, and C_d are modeling parameters with values of 1/3, 1/2, 8, and 5 respectively, as

given by O'rourke [39]. Equation (6.26) is then integrated in time simultaneously with the HRM model i.e., equations (6.22) and (6.23). The breakup criteria for the TAB model was taken to be $y = 1$ [39] and the same criticality criteria for the flash atomization mode as described before was utilized for the secondary breakup model. Again, the physical process that reaches its critical condition first will be the controlling mechanism. The flowchart for the coupled secondary breakup process is given in Fig.6.7.

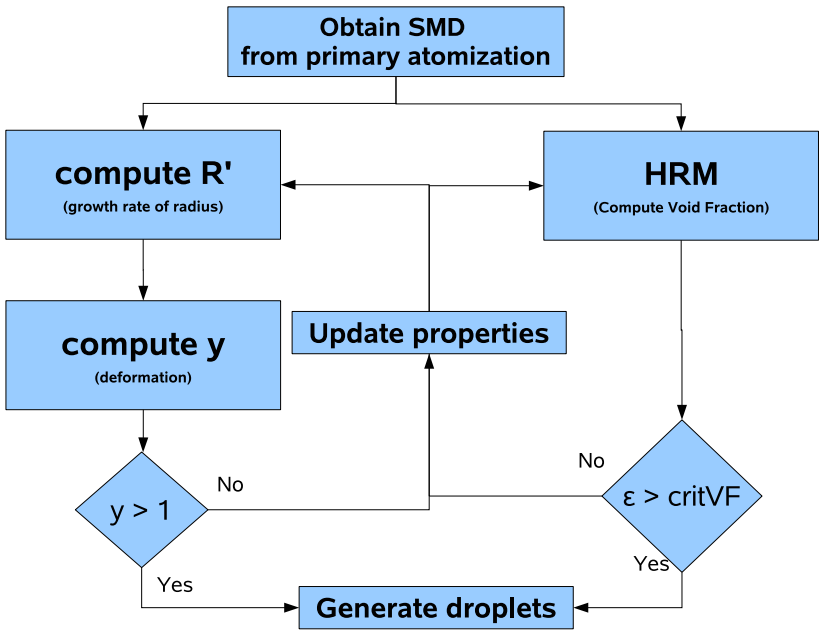

Figure 6.7. Flowchart for coupled HRMTAB

If flash atomization occurs, the same procedure used in the primary breakup model to obtain the droplet number density was implemented here. If TAB is the breakup mechanism, the expression developed in [39] for the mean droplet radius was implemented.

$$r_s = \frac{r_{init}}{1 + \frac{4}{3} * y^2 + \frac{\rho r_{init}^3}{8\sigma(\dot{y})^2}} \tag{6.27}$$

CHAPTER 7

INTERNAL NOZZLE FLOW - RESULTS AND VALIDATION

All the test cases used for validation were channel flows containing water. Though the simulation is transient, the experiments were always steady state, so all calculations were run until both the inflow and outflow had stabilized. The typical flash-boiling experiment is a straight channel with a sharp inlet. The sharp corner creates the potential for a separated flow with strong two-dimensional flow features. For convenience, these kinds of flows were simulated as axisymmetric flow. To avoid imposing boundary conditions where sharp gradients would be present, a plenum was added to both the inlet and outlet side of the channel, as shown in Fig. 7.1. The addition of the plenum provides some separation distance between the imposed boundary conditions and the region of interest. An unstructured quadrilateral mesh was used throughout the whole domain.

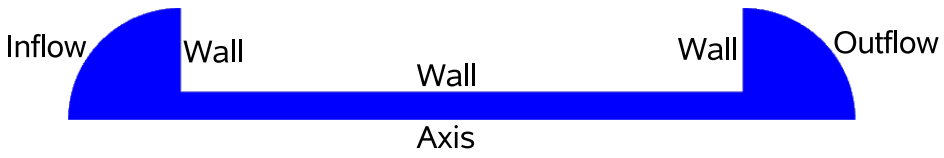

Figure 7.1. A typical two-dimensional computational domain.

7.1 Reitz Experiment

An experimental investigation using an axisymmetric nozzle and water as the working fluid was done by Reitz [43]. The downstream pressure was kept at 101 kPa and the inlet pressure was fixed at 787 kPa. He varied the inlet temperature and noted the effect on mass flow rate. The mass flow rate gradually decreased until an upstream temperature of about 430K was reached, whereupon the mass flow discontinuously dropped. Reitz reported that the mass flow rate dropped below the measurement range of his flow meter.

This experiment was simulated for validation and to provide new knowledge not obtainable in the original measurements. In the simulation, the axisymmetry of the nozzle was exploited to achieve quicker results. Fig.7.2 shows the geometry of the nozzle used in both the experiment and in the simulations.

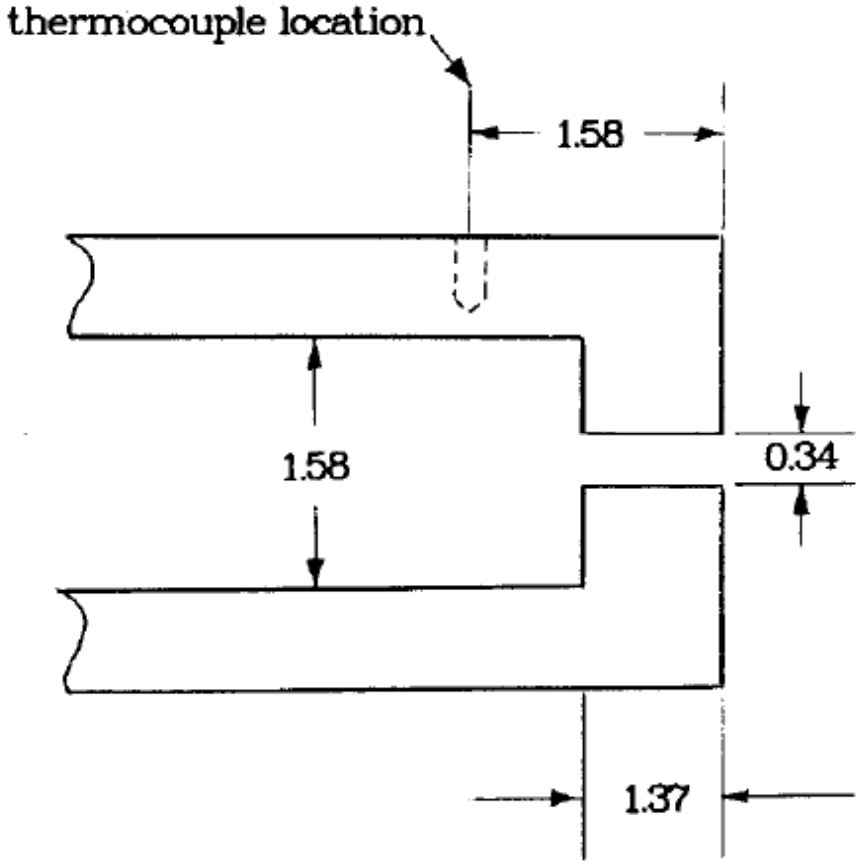

Figure 7.2. Nozzle design used by Reitz[43]. All dimensions are in centimeters.

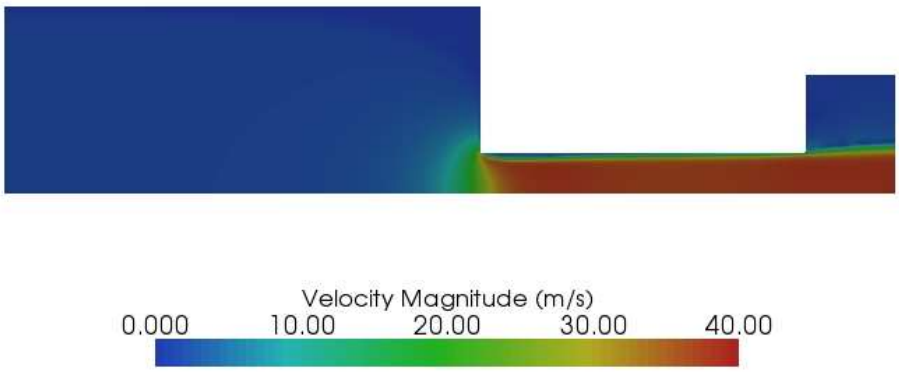

Figure 7.3. Velocity contours for inlet temperature = 404 K

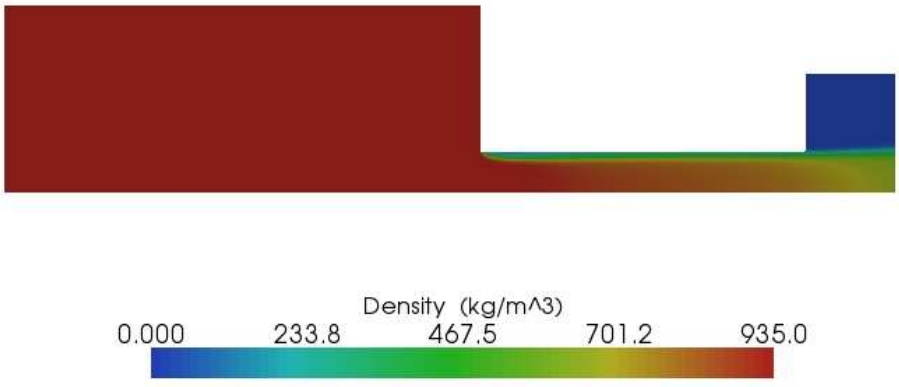

Figure 7.4. Density contours for inlet temperature = 404 K

The computational domain was meshed using quad cells. A receiver plenum was added to study the effects after the nozzle exit. Pressure boundary conditions were used at both the inlet and the exit of the nozzle. To reduce the effect of pressure waves bouncing off the boundaries which would generate numerical instabilities a transmissive formulation of the boundary conditions was employed. This technique sets a far field pressure value which is interpolated to the exit boundary.

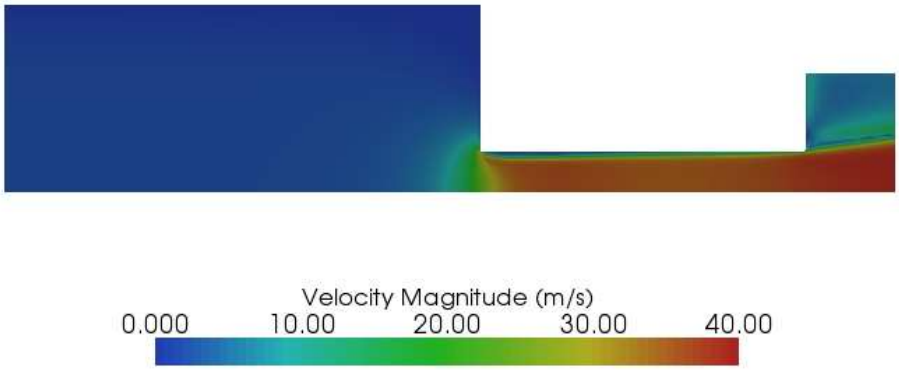

Figure 7.5. Velocity contours for inlet temperature = 415 K

Acceleration of the liquid through the nozzle results in a drop in pressure. When it falls below the saturation vapor pressure, it causes the liquid to flash boil. Figs. 7.3 and 7.4 reveal that the vaporization originates at the formation of the *vena contracta* at the inlet corner. This shows that flashing can also be geometrically induced, similar to cavitation. At inlet temperatures lower than 373 K the fluid was subcooled at the exit. Separation was observed at the inlet corner leading to the formation of a *vena contracta*. As the temperature was increased, more of the flashing was observed towards the nozzle exit

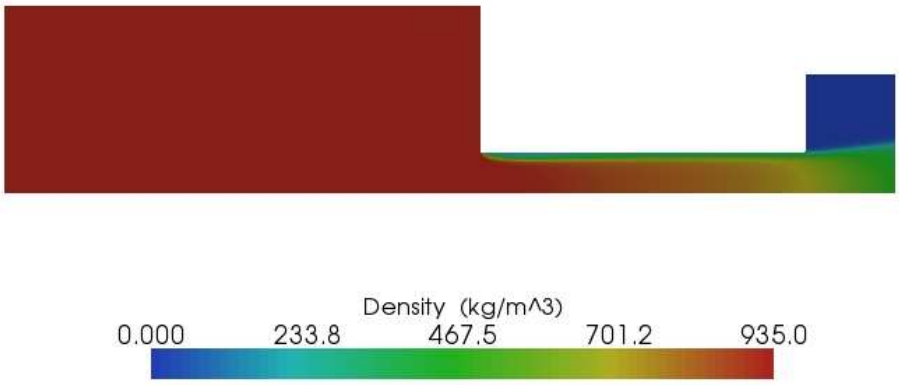

Figure 7.6. Density contours for inlet temperature = 415 K

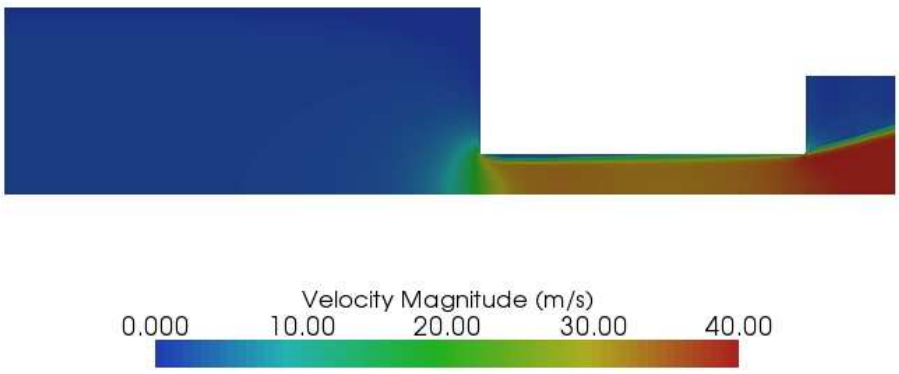

Figure 7.7. Velocity contours for inlet temperature = 427 K

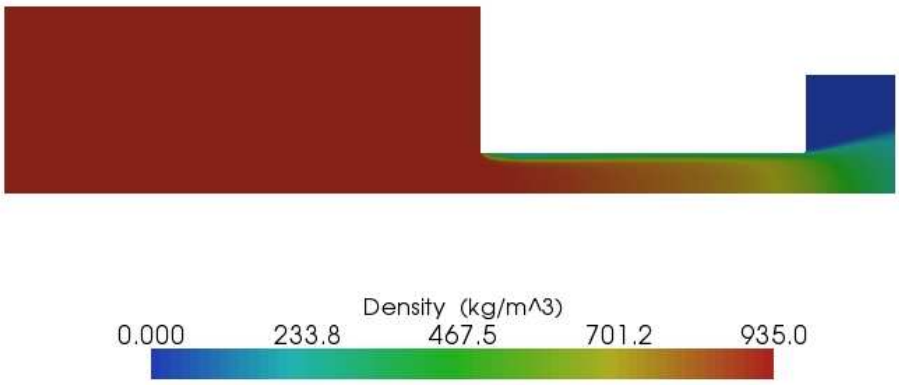

Figure 7.8. Density contours for inlet temperature = 427 K

With increased inlet temperature, the rate of flashing increases within the nozzle. This is is noted by the reduction in density in the contour plots, Figs. 7.4, 7.6, 7.8 and 7.10. The higher quantity of vapor in the interior of the nozzle causes a decrease in the overall mass flow rate of the fluid. Also, as the jet exits the nozzle, rapid expansion takes place as the vapor is no longer constrained by the nozzle wall.

Experiments with sprays undergoing flash atomization [66, 1] have observed an increase in the spray cone angle with the rise in the temperature of the working fluid. The contour plots of velocity in Figs. 7.3, 7.5, 7.7, and 7.9 show that fluid ejects at wider angles successively as the inlet enthalpy increases while the *vena contracta* undergoes little change..

The further increase in the temperature of the fluid promotes vaporization to such an extent that the liquid completely vaporizes inside the nozzle resulting in a dramatic decrease of the mass flow rate and a condition of "vapor lock." Though the experimental data show the approximate temperature where this discontinuous reduction

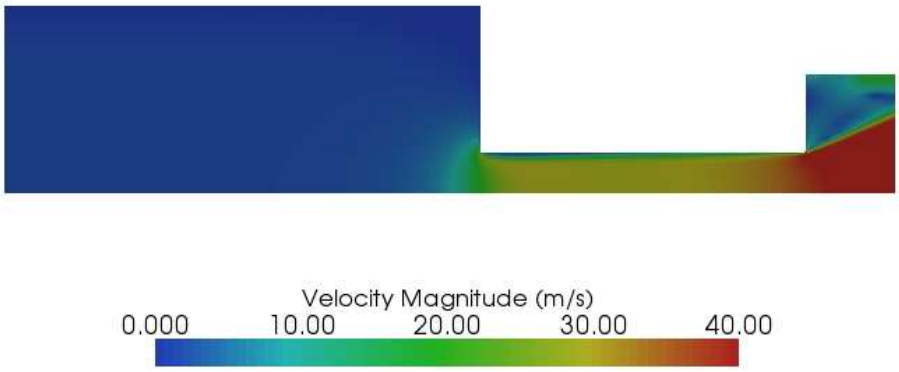

Figure 7.9. Velocity contours for inlet temperature = 438 K

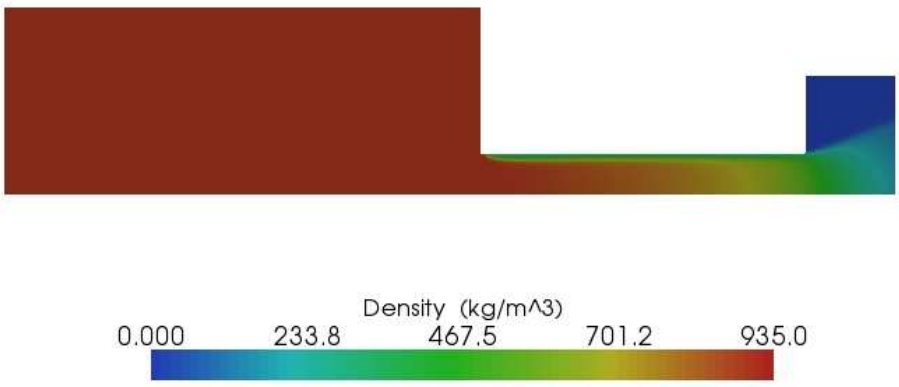

Figure 7.10. Density contours for inlet temperature = 438 K

of mass flow occurred, the actual mass flow rate dropped below the resolution of the flow meter at about 430K. A comparison of the computed and measured mass flow rates is given in Fig. 7.11. An analytical calculation based on Bernoulli's equation will grossly overpredict the mass flow rate. Even frozen flow models will under predict vapor formation thus leading to erroneous results. The frozen flow calculations reported are achieved by setting the timescale of vaporization to a sufficiently high value compared to the characteristic time of the system. For practical purposes the phase change time can be considered infinite in the frozen flow calculations. On the other end of the spectrum, an equation of state approach is achieved by setting the timescale of vaporization to a value smaller than the timestep size of the computation. This method results in excessive vapor generation and hence a much lower prediction of mass flow rates.

An equilibrium type calculation at higher temperatures poses additional numerical challenges as well. For example, consider the case for which the inlet temperature of the incoming fluid is 438 K. The equilibrium vapor density at this temperature is 0.5 kg/m^3. Assuming a nozzle discharge coefficient of 0.6, an analytical calculation gives that the predicted velocity of the vapor at the exit is 993.9 m/s. This value of exit velocity is not only unrealistic but will also be a large source of numerical error in any computation.

The finite rate process modeled by HRM is shown to obtain results very close to that experimentally observed. Though there is slight disagreement about the exact temperature at which the drop-off in flow occurs, the model succeeds in predicting the mass flow rate in the flashing nozzle over a range of temperature. In the simulations, the critical temperature for vapor lock corresponds closely to the temperature at which the vapor pressure equals the upstream static pressure. At the upstream pressure of 787 kPa, the saturation temperature of water is 443 K. Under superheated conditions,

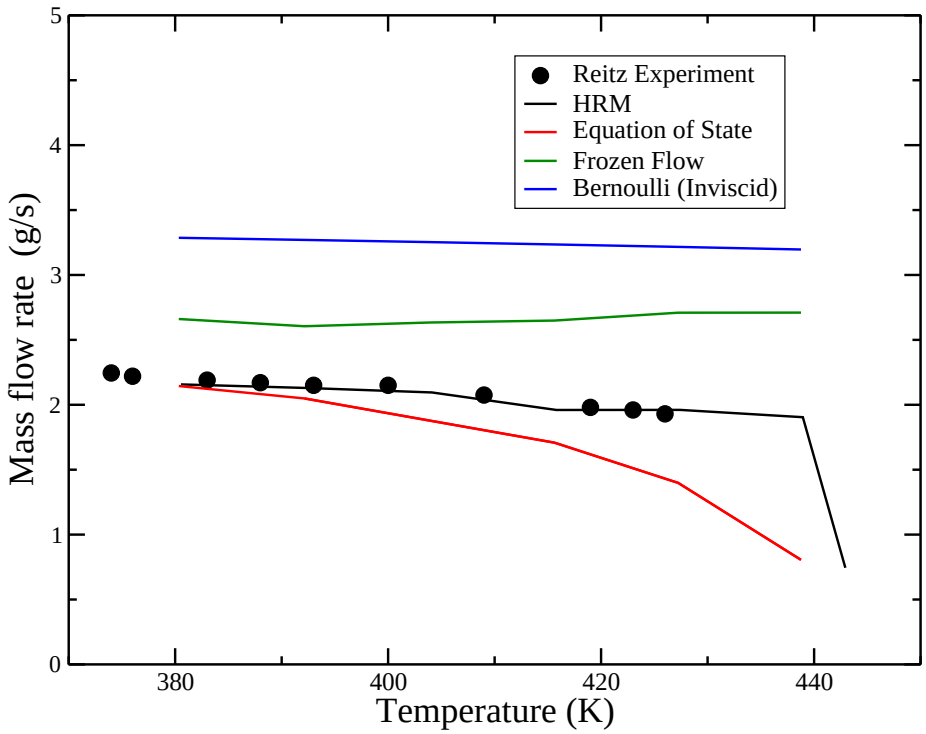

Figure 7.11. Comparison of mass flow rates between experiments and simulations

where the incoming fluid has a vapor pressure in excess of the upstream pressure, the simulation predicts that the entire nozzle fills with vapor.

7.2 Tikhonenko Experiment

A high temperature, high pressure test case was taken from Tikhonenko et al. [55], who explored critical flow of hot water in various pipes with a sharp inlet. These experiments include data from pressure taps placed along the length of the pipe. In this simulation, a channel with a 25 mm diameter and 250 mm length was simulated. The inlet conditions were saturated water at 4 MPa and the downstream pressure was specified to be one atmosphere.

This test case was used to check grid independence of the solution. Even though a perfectly sharp corner represents a singularity, the flow should show an acceptably low sensitivity to the mesh resolution in order for the results to be useful. The nozzle was meshed using a coarse mesh of three thousand five hundred cells and a finer

mesh with fifteen thousand cells. A comparison of predicted wall pressures from the several calculations, exploring both the high pressure and low pressure correlations (see Eqns. 3.8 and 3.10) and mesh sensitivity, can be seen in Fig. 7.12. The coarser mesh is sufficiently close to the fine mesh result, such that the modeling assumptions are a larger source of error than the discretization error.

The results for static pressure along the pipe wall in Fig. 7.12 also permit a comparison of the two correlations, as well as revealing some of the internal flow features. The experimentally-measured pressure shows a slight local minimum near the inlet corner due to the separated flow. As the computational results will show, the liquid forms a vena contracta downstream of the inlet. Once past the vena contracta, the pressure partially recovers and then drops precipitously at the exit.

The computational results follow the expected trend. There is a local pressure minimum on the wall just downstream of the inlet corner in the simulations. The pressure recovers slightly and then remains nearly constant along the nozzle length until just upstream of the nozzle exit. The pressure at the nozzle exit decreases dramatically due to rapid flashing near the exit plane. However, both correlations under-predict the rate of flash boiling, though the low pressure correlation is especially far off. The high pressure correlation produces pressures that are much closer to the experimental measurements.

In addition to predicting pressure, the computational results show other features of interest, such as pressure, velocity, density, and the rate of change of quality. These results can be used to explain the nozzle behavior under these flow conditions.

As in both single-phase and cavitating nozzles, the flow separates off of the sharp inlet corner [44]. In an incompressible flow, the pressure would be expected to be extremely low downstream of this corner, due to the separated flow and the constraint of a divergence-free velocity field. However, with flashing flow, the decrease in pressure creates an increase in the rate of phase change. The flashing of the liquid creates a

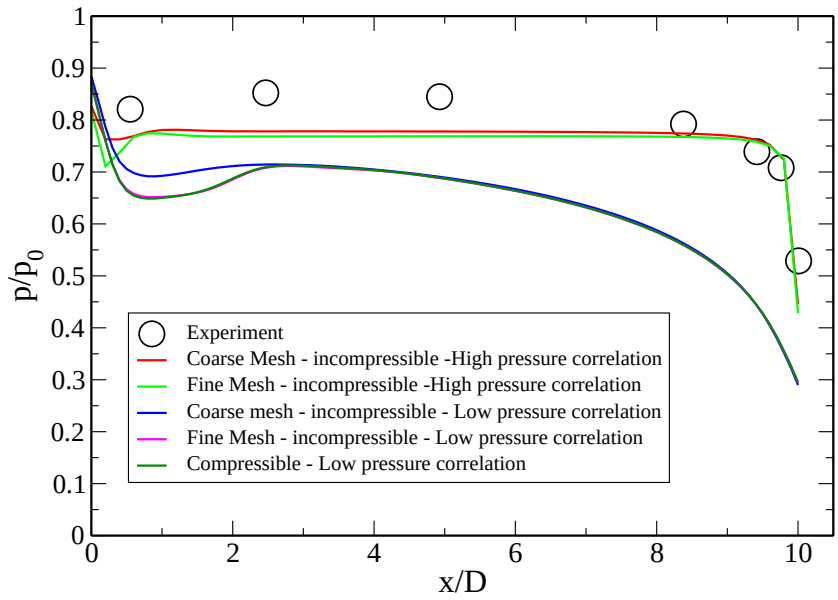

Figure 7.12. Static pressure versus position at the wall for saturated water at 4 MPa discharging through a 25 mm tube with L/D=10

positive velocity divergence that allows the contraction to occur with a relatively small dip in pressure behind the inlet corner.

The contours of volume fraction in Fig. 7.13 show this rapid vapor generation at the inlet corner. The two-phase density in the computational domain ranges from the initial saturated liquid density down to a value of 1.5 kg/m^3. The sharp corner induces a phase change around the outer periphery of the flow. This vapor remains as an outer sheath for the length of the nozzle, as previously described in experimental studies [15].

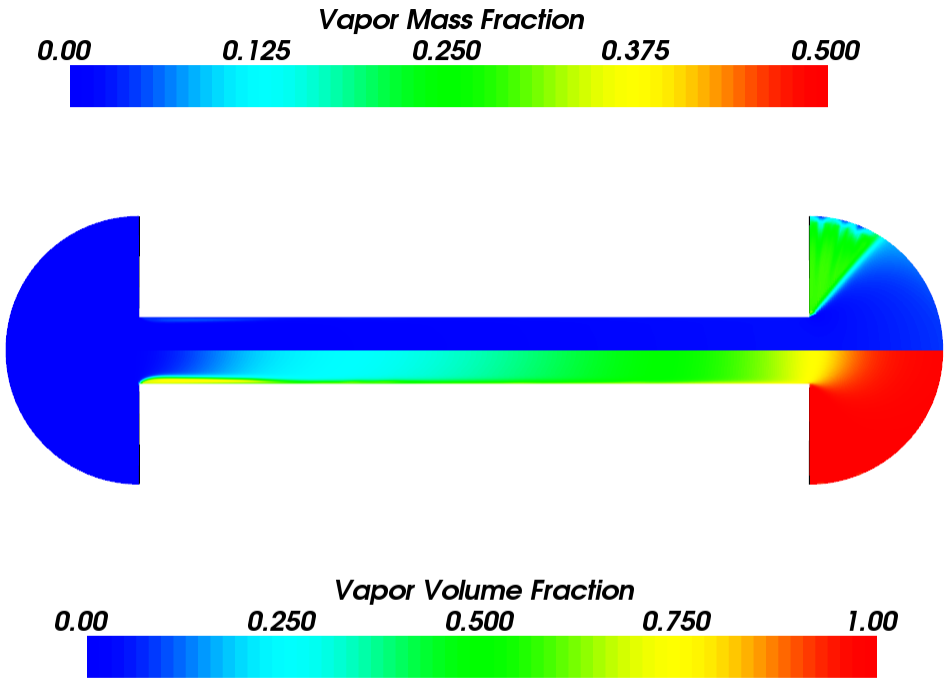

Figure 7.13. Predicted vapor mass fraction and volume fraction in the 4 MPa saturated water experiment of Tikhonenko. The domain has been reflected around the axis of symmetry so that two fields can be shown simultaneously.

This radial density and velocity profiles are interesting features of a multi-dimensional CFD study of flashing nozzles. It serves as an example of macroscopic interphase slip,

where the liquid core moves with one velocity at the inner radius in the nozzle and the vapor could move with a different velocity near the nozzle walls.

Between x/D of 2 and 8, very little change occurs in the axial direction. The pressure gradient is minimal and there is little change in the radial density or velocity profile. However, near the nozzle exit plane, a dramatic change occurs, as shown in Fig. 7.14.

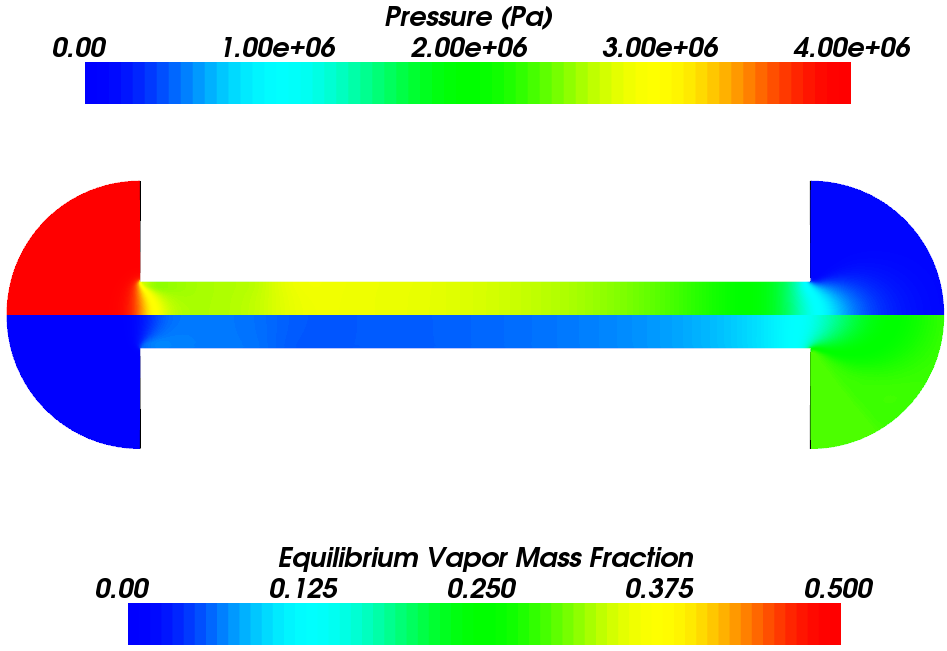

Figure 7.14. Predicted pressure and equilibrium mass fraction $\overline{x}$ in the 4 MPa saturated water experiment of Tikhonenko.

Figs.7.12 and 7.14 indicate that part of the pressure drop across the nozzle occurs at the inlet, followed by a relatively flat pressure region, and then a second pressure drop at the exit. As the pressure drops further below the vapor pressure of 4 MPa, the rate of phase change increases. The nature of the timescale correlation provided by Downar-Zapolski et al. [11] also captures the effect of increasing interfacial area for

phase change, due to the dependence on vapor volume fraction. So, with the creation of vapor, the rate of phase change is further increased. Note how the timescale shown in Fig. 7.15 correlates with the creation of vapor. By conservation of mass, the drop in density is accompanied by an increase in axial velocity. Conservation of momentum then indicates that pressure drops further. This pressure drop, in turn, feeds back into the flashing process. The pressure finally reaches the downstream value just outside of the nozzle.

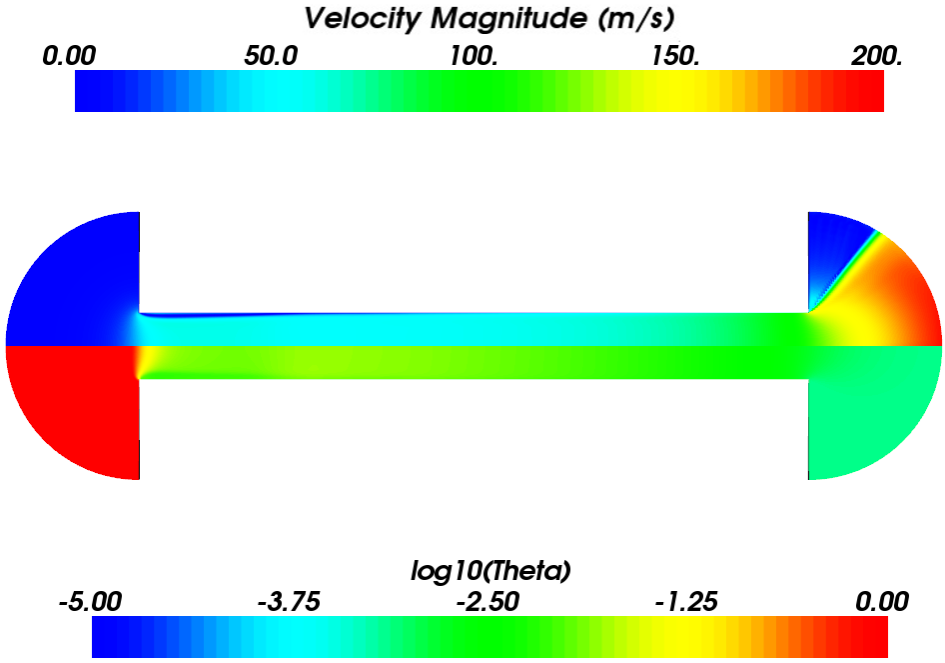

Figure 7.15. Predicted velocity magnitude and the common log of the phase change timescale Θ for the 4 MPa saturated water experiment of Tikhonenko.

The anticipation that the flashing flow process would continue just beyond the nozzle motivated the decision to place the computational boundary downstream of the nozzle. However, the model does not account for the presence of non-condensible gases, such as air. Fortunately for this case, it appears from the velocity field that air

is not entrained into the internal nozzle flow. The strong favorable pressure gradient near the nozzle exit discourages the counter-flow of air and produces no recirculating flow in the exit plenum of the computational domain.

The ability of the model to predict choking was also investigated. The high liquid temperature and low downstream pressure suggests that the flow should be choked [17]. Computationally, this is indeed the case. The above simulation was re-run with the downstream pressure set to two atmospheres, which reduces the pressure drop across the nozzle by 2.6 percent. The computed mass flow rate changed by less than 0.03 percent.

7.3 Fauske Experiment

The second test case was chosen to emphasize two-dimensional effects. In these experiments Fauske [17] studied saturated water discharge through short tubes. He noted the maximum discharge rates as a function of L/D and upstream stagnation pressure. Of the various nozzles that Fauske tested, a relatively short nozzle was chosen for validation, with $L/D = 4$, in the next test case. It is expected that the inlet corners will cause large variations of void fraction and velocity in the radial direction. These two-dimensional effects are likely to be more pronounced than in the longer nozzle discussed above.

First, the mass flow rates were compared for 6.35 mm diameter tubes at stagnation pressures of 1.37 MPa, 4.13 MPa, and 6.89 MPa. The calculated mass flow rates using the low-pressure correlation, Eq. 3.8 are compared to Fauske's measurements in Fig. 7.16. The agreement of the data is excellent, with the computed results lying within the scatter of the experimental data. The good agreement produced by the low-pressure correlation is somewhat surprising and much better than the high-pressure correlation, Eq. 3.10, which under-predicted mass flow rate by a factor of two.

In the calculations shown back in Fig. 7.12 the high pressure correlation performed better, as one might expect given the 4 MPa upstream pressure. In the simulations with Fauske's experiments, the low pressure correlation was clearly better. This observation is especially curious given the similarities between the two experiments. Tikhonenko's experiment was at an upstream pressure very close to the middle of the range of Fig. 7.16 and both were saturated. The L/D ratio for the data in Fig. 7.16 are for L/D of 4, compared to Tikhonenko's L/D of 6. The diameter of Tikhonenko's nozzle was about four times larger than Fauske's, which could be a factor.

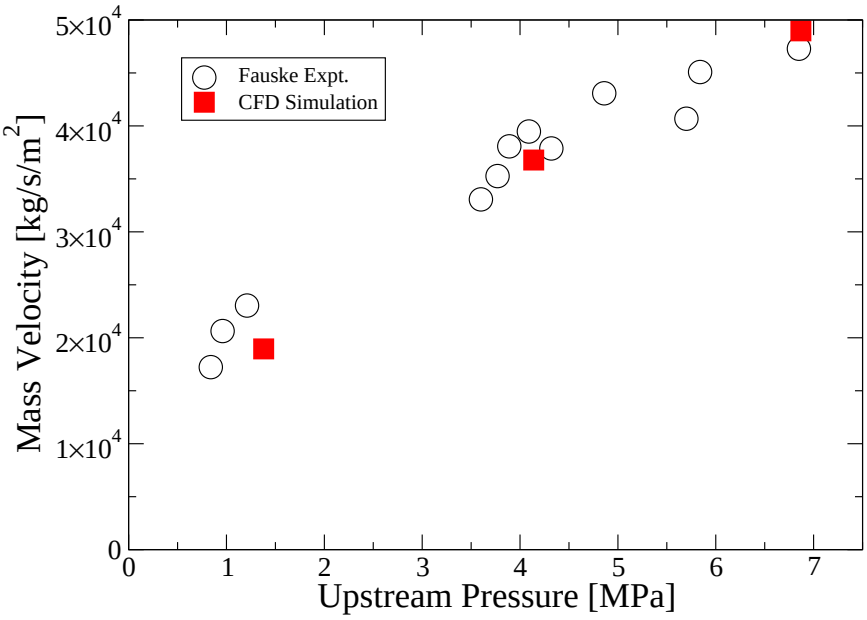

Figure 7.16. Measured [17] mass flow rates for a nozzle with L/D=4 compared with the present calculations.

Next, the internal flowfield details were observed in order to understand how the two-dimensional effects were manifesting themselves in the flowfield. The first figure illustrates a simulation of Fauske's experiment with an upstream pressure of 1.38 MPa (200 PSIA). Fig.7.17 shows the volume fraction of vapor in the upper half of the figure and approximate stream lines in the bottom half. The streamlines are not

from a solution of a stream function, since the velocity field is not divergence-free, but are rather calculated from Runge-Kutta integration of particle trajectories using the discrete velocity field, incurring a discretization error commensurate with the CFD computations.

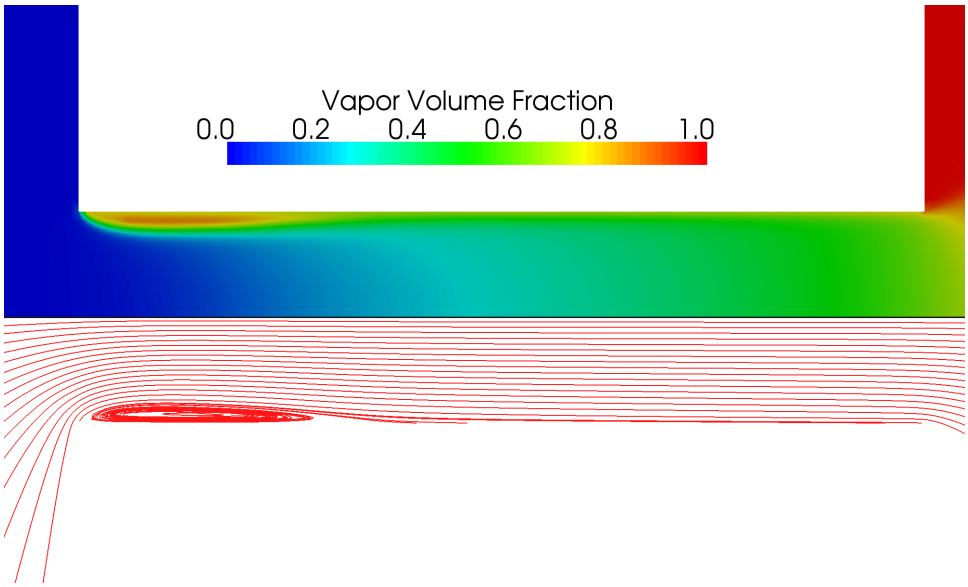

Figure 7.17. Simulation of Fauske's experiment with 1.38 MPa saturated liquid discharge. This figure shows volume fraction of vapor and approximate streamlines.

The streamlines in Fig. 7.17 show the separation and formation of a *vena contracta* just downstream of the nozzle inlet. The outer flow recirculates downstream of this corner, forming an area of high vapor concentration. This outer fluid likely has a long residence time in the nozzle due to the recirculation, which may explain why Fauske did not observe any sensitivity to nucleation. The recirculating fluid has a relatively long time to change phase, compared to the central flow. As the vapor fraction shows, the core begins to vaporize closer to the exit. The predictions of the annular vapor sheath and core vaporization are consistent with Fauske's observations and published sketches of the flow.

The phase change process is accompanied by acceleration as a consequence of conservation of mass and momentum. This acceleration is evident in the upper half

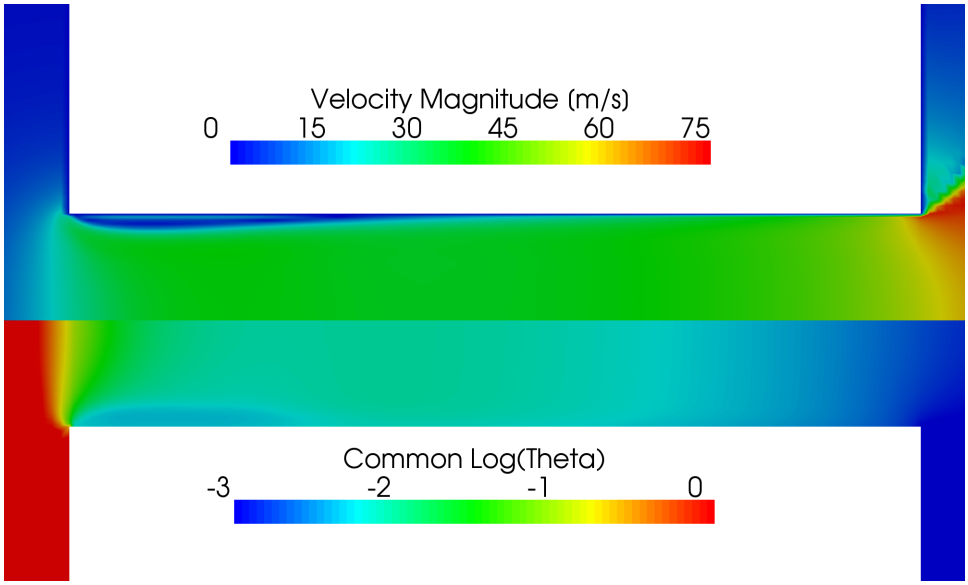

Figure 7.18. Simulation of Fauske's experiment with 1.38 MPa saturated liquid discharge. This figure shows velocity magnitude and the common logarithm of the timescale of phase change.

of Fig. 7.18. The initial contraction near the throat of the *vena contracta* produces an acceleration as the core flow passes through a reduced cross-sectional area in the nozzle. A second acceleration occurs near the exit, where vapor is formed.

As vapor is formed, more interfacial area is available for heat transfer, which feeds back into the phase change process by shortening the timescale. The feedback of between interfacial area and the timescale can be seen in the lower half of 7.18, where the lowest values of the timescale represent regions where the fluid will move more quickly towards the equilibrium quality.

The above figures were only considering the lower end of the range of upstream pressures. However, the general character of the nozzle flow in these saturated discharge calculations is relatively insensitive to variations in the upstream pressure. Though velocities increase with increasing upstream pressure, the *vena contracta* remains a relatively constant feature. The amount of vapor does not change much with a factor of five increase in upstream saturation pressure, as shown in Fig. 7.19. The

stability of the *vena contracta* is well-known from previous studies of cavitating flow and single-phase nozzle flow [36].

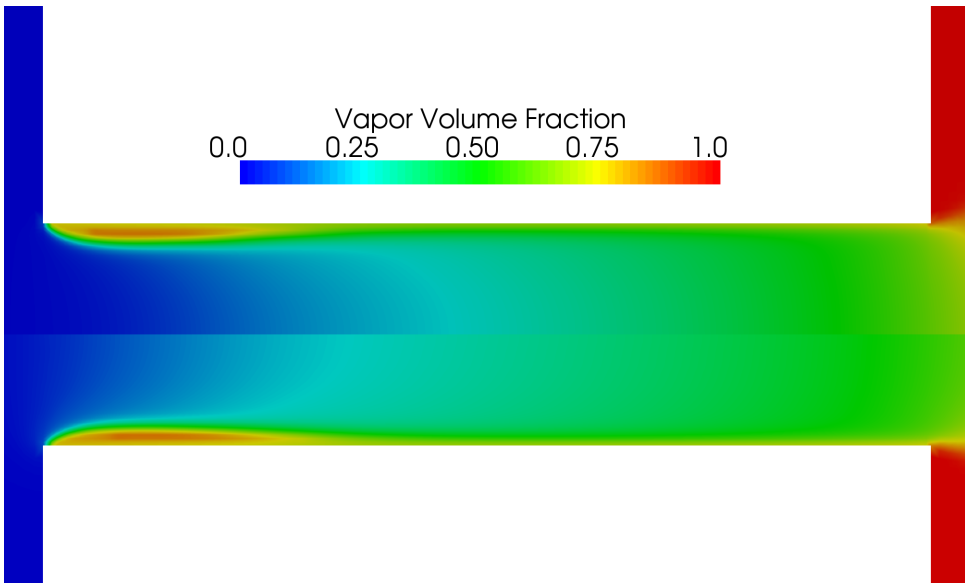

Figure 7.19. Comparison of the volumetric vapor fraction with 1.38 MPa saturated liquid discharge (upper half) and 6.89 MPa (lower half).

7.4 Three Dimensional Nozzle

Simulations were performed on a three dimensional, single-hole, asymmetric fuel injector shown in Fig. 7.21. The design for the fuel injector obtained from Bosch GmbH is shown in Fig.7.20. This particular design is intended for research only and not for production purposes. The single nozzle is offset at an angle such that the entry of the fuel was non−orthogonal. A receiver plenum has been added for this case as well to capture physics downstream of the nozzle exit.

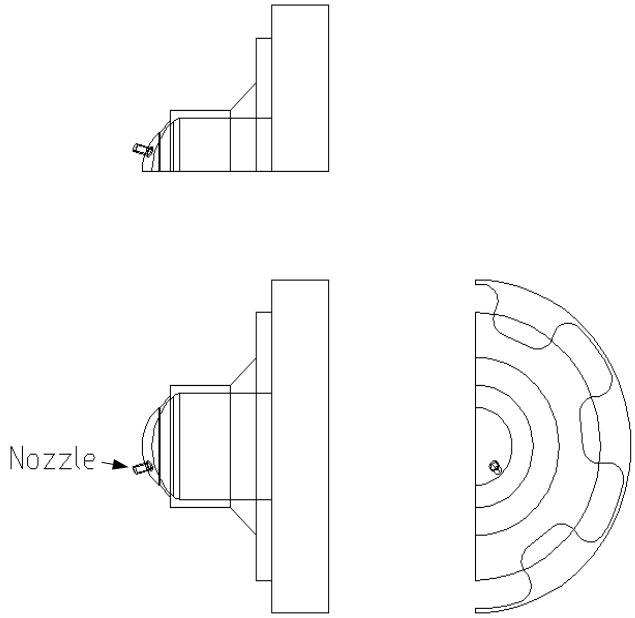

Figure 7.20. Orthographic projection of the injector design obtained from Bosch GmbH.

A hybrid mesh is employed with hexahedral cells in the nozzle interior (see Fig. 7.22) and tetrahedral cells in the rest of the injector volume, for a total cell count of two-hundred thirty-eight thousand. A Dirichlet pressure condition was specified at the exit of the nozzle and it was set to 1 bar for all the cases. A time-varying velocity condition was specified at the inlet in which the velocity was ramped up to a final steady-state velocity over a time 0.1 ms. Table 1 provides the boundary conditions

for the different cases. Normally the incoming and outgoing mass flow rates differ during the transient phase change process; comparing the inlet and outlet mass flow rates suggest that steady state was reached by about 0.25 ms. The results shown below are after a simulated time of 0.25 ms.

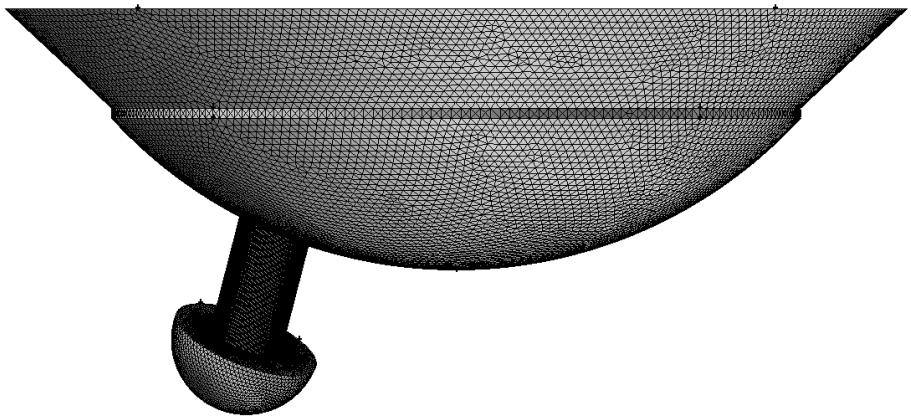

Figure 7.21. Computational domain with mesh

The working fluid used is water. At the time of the investigation gasoline data were not available in a format required for the code. It is proposed to study realistic fuels in future work.

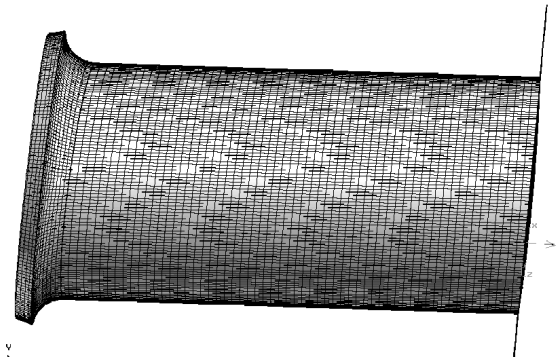

Figure 7.22. Hexahedral mesh in nozzle

For clarity, the three-dimensional results are shown on a plane through the orifice axis. Fig. 7.23 orients the reader with cut plane used in the subsequent figures.

	Inlet Velocity (m/s)	Exit Pressure (bar)	Temperature (Celsius)
Baseline	3.0	1.0	120
Low Flow	1.0	1.0	120
High Flow	4.5	1.0	120
Low Temp.	3.0	1.0	50
High Temp.	3.0	1.0	170

Table 7.1. Table. 1 Boundary conditions used for three dimensional injector case

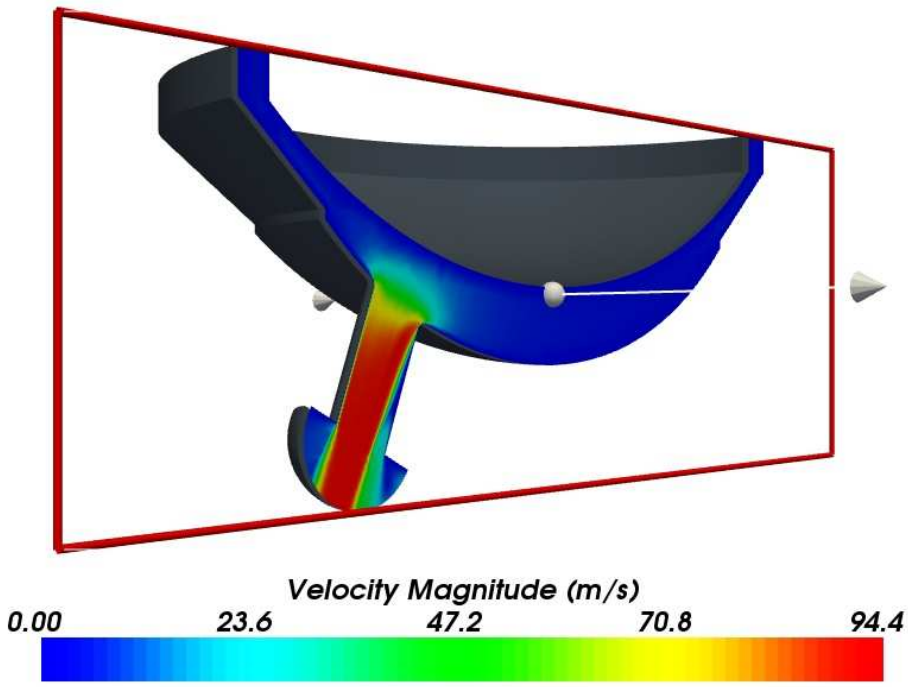

Figure 7.23. Orientation of the cut plane

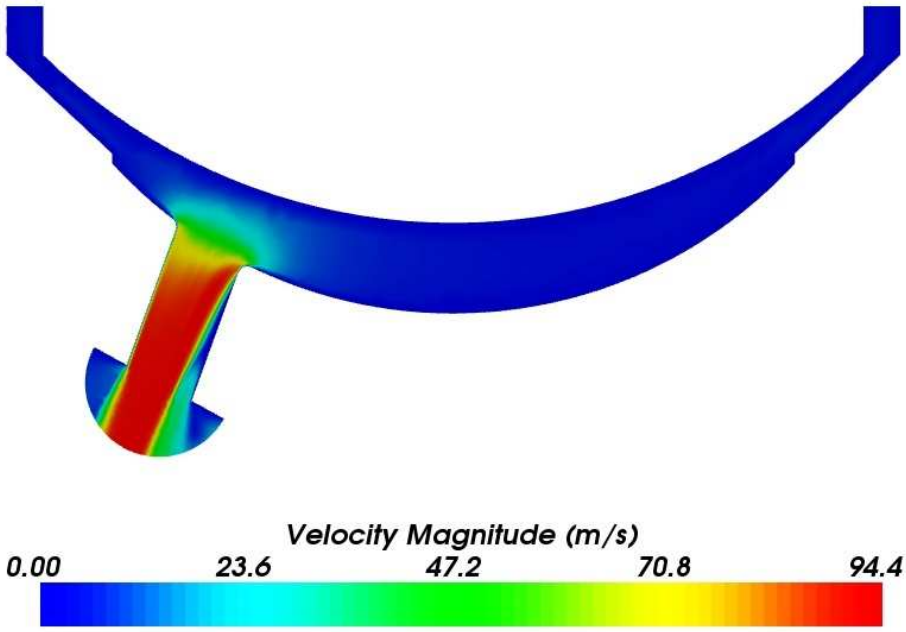

Figure 7.24. Velocity contours for baseline case

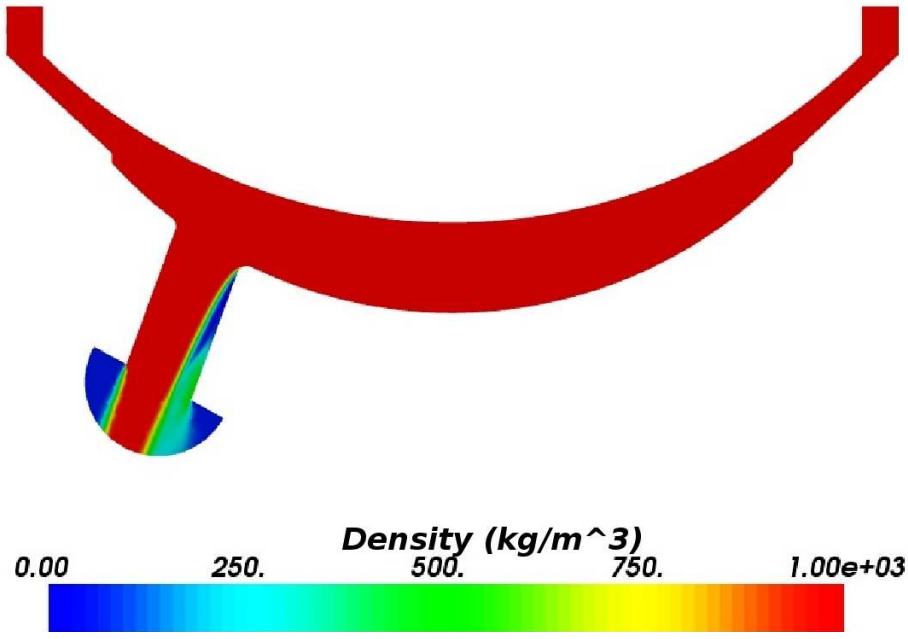

Figure 7.25. Density contours for baseline case

Similar to the axisymmetric nozzle, it is noted that flashing begins at the inlet corner. The asymmetry of the nozzle design induces vapor formation at the corner which is closer to the central axis of the injector, as is depicted in Figs. 7.24 and 7.25. This also forces the jet exiting the nozzle to be non-uniform and the liquid core to be shifted outward.

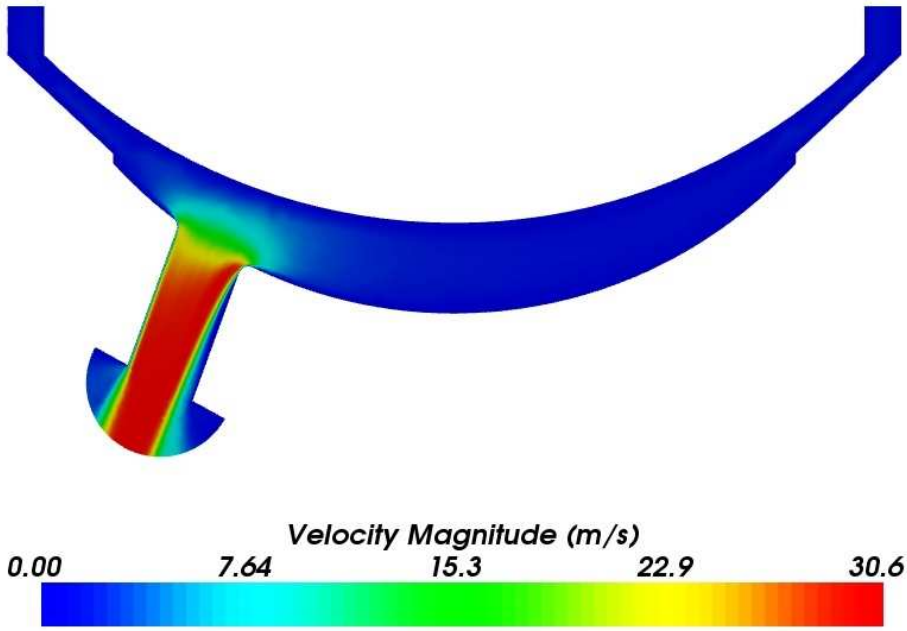

Figure 7.26. Velocity contours for low flow case

For the low flow case, it is observed that vaporization is diminished and the liquid core is more prominent, as can been seen in Figs. 7.26 and 7.27. The high flow case, shown in Figs.7.28 and 7.29, has significantly more vapor formation as compared to the baseline and low flow cases. The expansion of the jet as it exits the nozzle is also at a much wider angle in comparison to the previous two cases.

Lowering the temperature changes the pattern of the vapor formation as seen in Fig. 7.31. The spread of the vapor compared to baseline case is narrower with vapor at the widest part having a lower density. On the other hand, increasing the

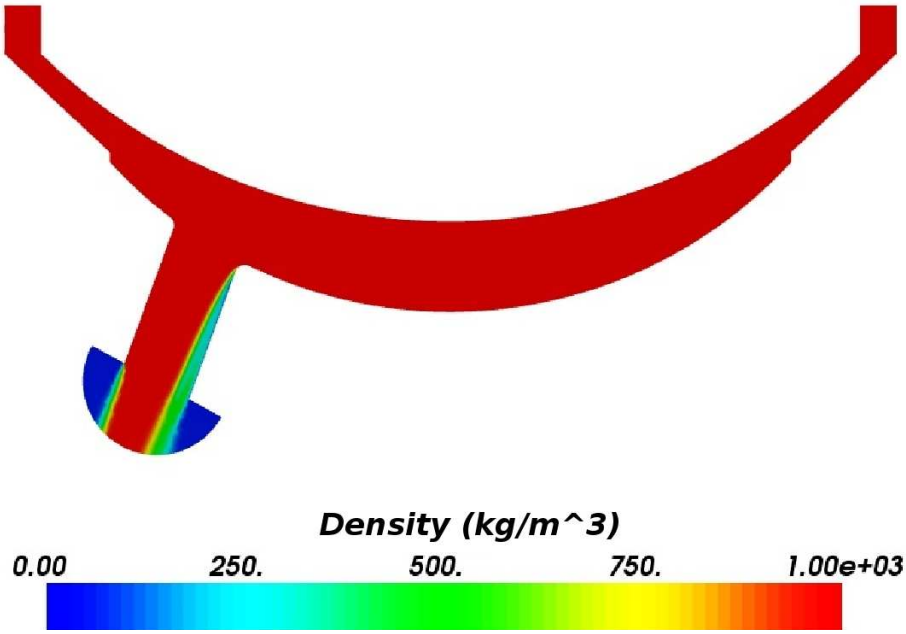

Figure 7.27. Density contours for low flow case

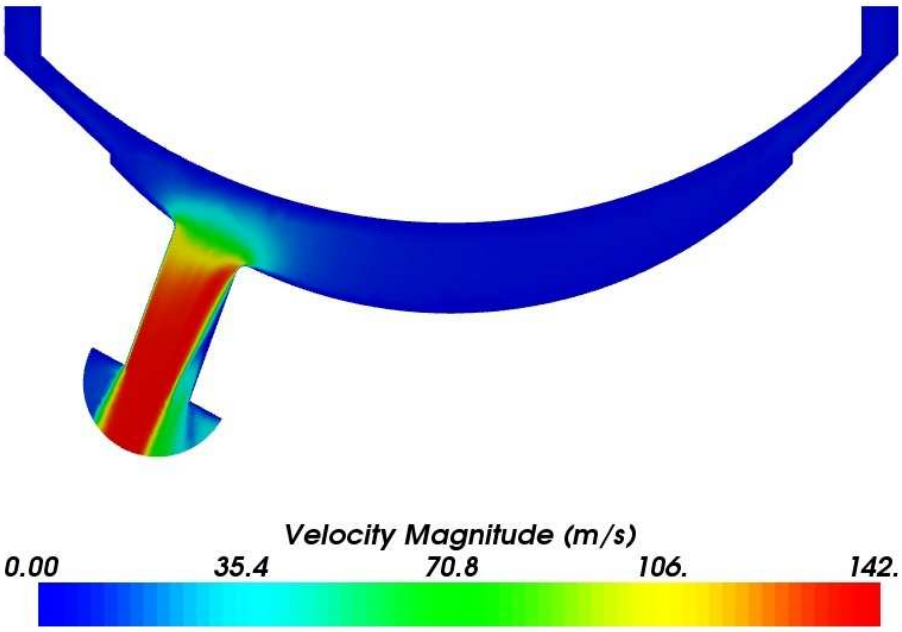

Figure 7.28. Velocity contours for high flow case

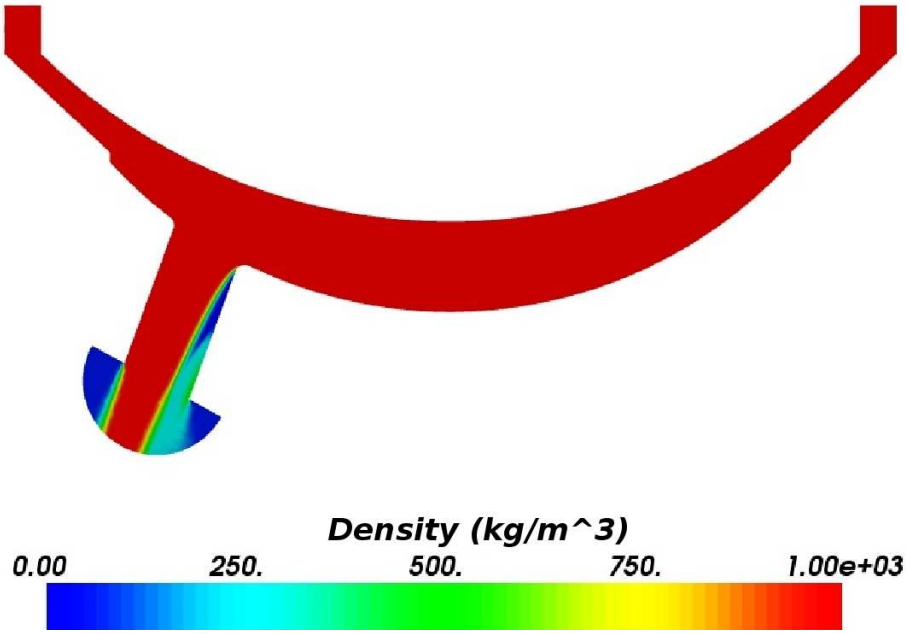

Figure 7.29. Density contours for high flow case

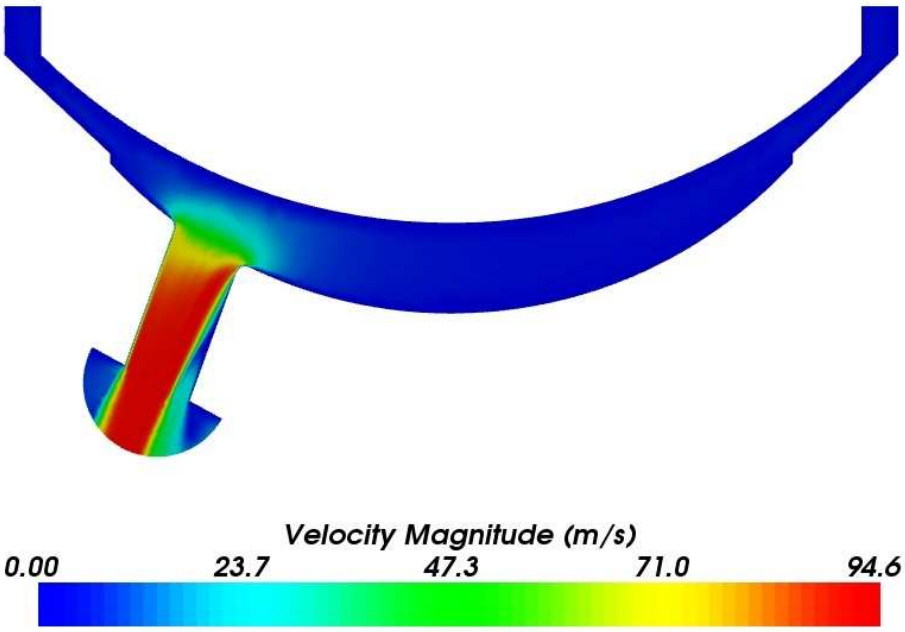

Figure 7.30. Velocity contours for low temperature case

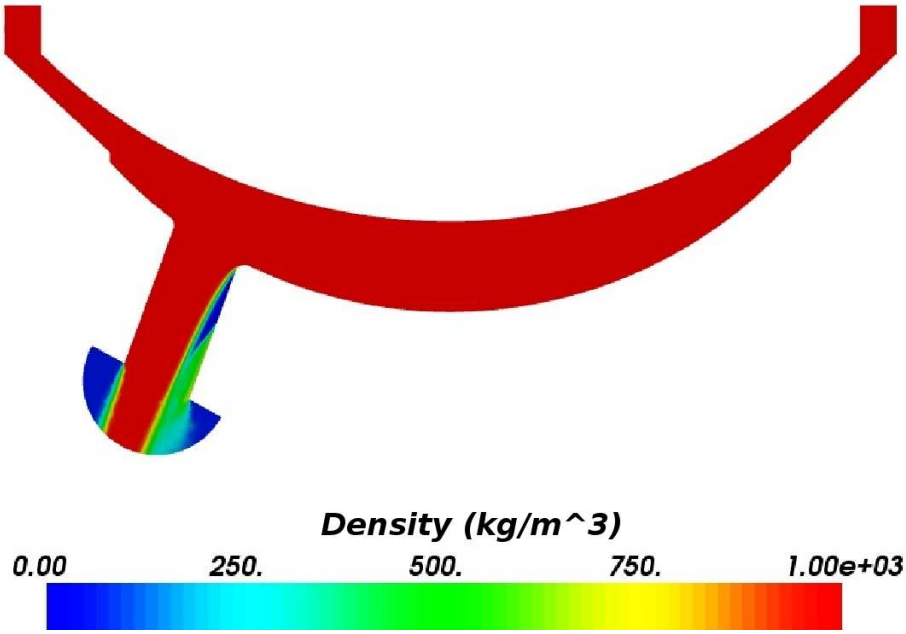

Figure 7.31. Density contours for low temperature case

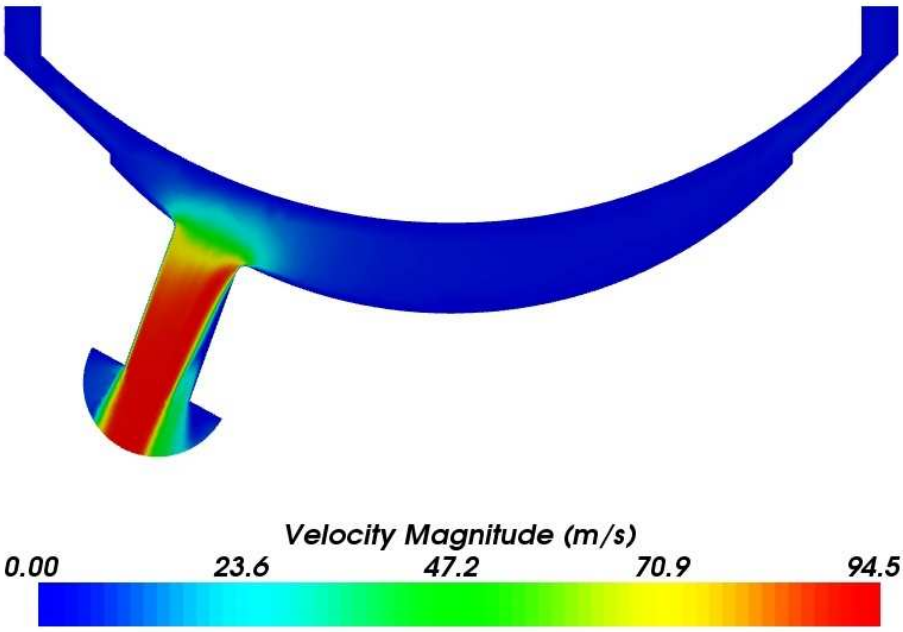

Figure 7.32. Velocity contours for high temperature case

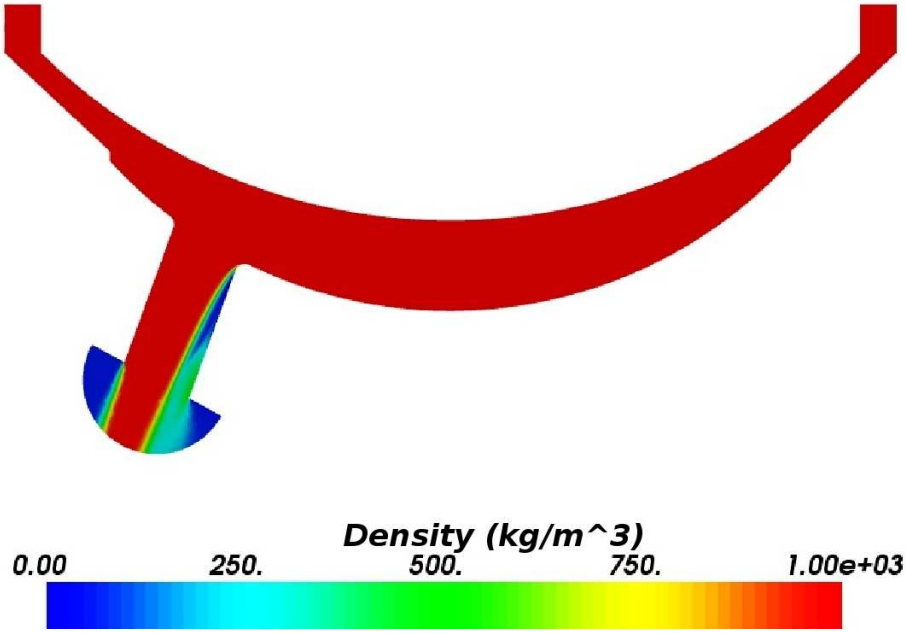

Figure 7.33. Density contours for high temperature case

temperature of the incoming fluid results in it being ejected at wider angle. The vapor density is also higher than the comparative cases for lower temperatures.

It is interesting to note that the velocity profiles and mass flow rates are less sensitive to the variation in temperature for the three dimensional case than the previous axisymmetric case. The injection pressure is around ten times higher than the one used by Reitz. The consequence of a higher injection pressure is that the flow–through time is diminished, reducing the sensitivity to inlet temperature of the fluid.

The lack of experimental data prohibits the validation of these calculations. The accurate validation from the calculations for the axisymmetric nozzle gives us confidence in numerical results for this simulation. The attractive features of this case is the use of full three dimensional hybrid mesh. MPI parallelization was used to run

the case on multiple processors. Speedup tests indicated super-linear performance enhancement using up to six processors on a cluster of dual-CPU Itaniums.

7.5 Conclusions

The first major finding of this work is that the flashing begins well inside the nozzle, typically near the inlet corner. The phase change process is usually geometrically induced, similar to cavitation. Unlike cavitation, the vapor region continues to expand as the flow proceeds towards the exit.

The second finding is that at high temperatures the phase change process begins to manifest itself strongly across the breadth of the nozzle exit. The outer sheath of vapor is supplemented by vapor created across the entire exit plane. Further, at the highest temperatures a strong radial expansion of the flow is evident in the computational results, which is consistent with expectations that the flashing flow should produce a wider spray angle.

The final observations are from the three-dimensional calculations. These calculations show asymmetric vapor generation due to the angle between the nozzle and the tip volume. The simulations were performed with higher injection pressures than those used in the two-dimensional experimental validation cases. Because of the shorter flow-through time and the stronger inertia of the flow, there is less sensitivity of the internal nozzle flow to the fluid temperature. This observation of the internal flow should not lead the reader to assume that the exterior spray will be less sensitive to temperature.

CHAPTER 8

INTERNAL FLASHING FLOW OF JP8

The internal flow model was coupled to a fuel property database for jet fuel (JP8). Simulations were perfomed to demonstrate the ability to handle multicomponent hydrocarbons as a working fluid. The lack of experimental data for JP8 prevented the validation of these calculations. A typical injector for aerospace applications with a diameter of 2mm and L/D ratio of 30 was modeled as a straight channel. Numerical simulations were performed using JP8 with varying the inlet and back pressures. The temperature of the entering fluid was 620 [K] (h=-6×10^4 [J·mol^{-1}]). The presented results were obtained under the adiabatic assumption.

8.1 Multi-component Superheated JP8 Model

A fluid is in a superheated state when its vapor to liquid mass ratio (the quality x) is below its equilibrium value x^{eq}. A superheated fluid is in a state of non-equilibrium and thus will relax towards the equilibrium state via the mechanism of nucleation site formation and bubble growth. In this state, for a multi-component system, one needs three variables to define a state. Lee et al [31] used the coordinates of enthalpy, pressure, and quality $< p, h, x >$ to define the state and the techniques used by them to evaluate thermophysical propertied is described in this section. A surrogate model was constructed by Lee et al. to describe the multi-component nature of JP8; in particular, a six component model termed "surrogate #2" or "sur2" reported in [59, 8]. The composition of this surrogate model as stated in [59] is incorrect; the correct composition was obtained from the authors and is thus: para-xylene 8.5%, Naptha-

lene 8%, N-Octane 3.5%, Decalin 35%, Dodecane 40%, and hexadecane 5%. Many different surrogate models had been considered, including those that were explicitly optimized for the combustion kinetics [8] but not volatility or any thermodynamic properties [6]. This particular one from [59] was down-selected for its accurate prediction of the volatility of JP8 (or the Jet-A family). In fact, its prediction on other thermodynamic variables such as heat capacity, conductivity, viscosity etc. also agree with data published in [7]. The distillation curves for this surrogate model and two others are shown in Fig. 8.1 along with the data reported in a CRC data book [7]. Other surrogate models had been tested and the ones shown in this figure represent those that fit the CRC distillation data the best.

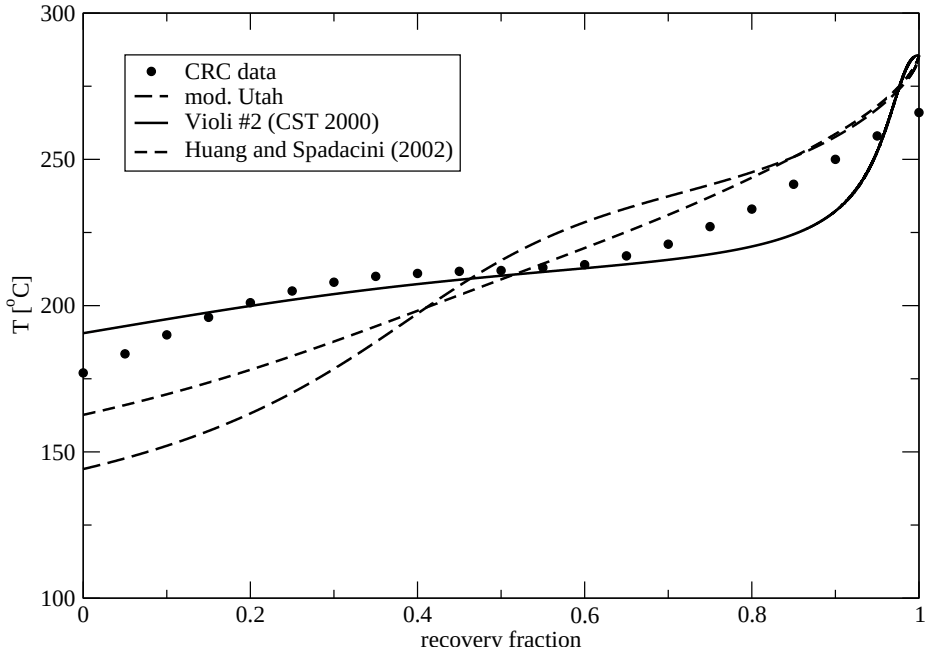

Figure 8.1. Distillation curve of surrogate fuel for JP8. Given by Lee et. al. [29]

The bubble point is more critical in describing the volatility of JP8 although it is typically not specified in the petroleum industry. The loci of the bubble and dew points predicted by this surrogate model are shown in Fig. 8.2. They were obtained by solving iteratively the equation of state for the conditions in the p-T

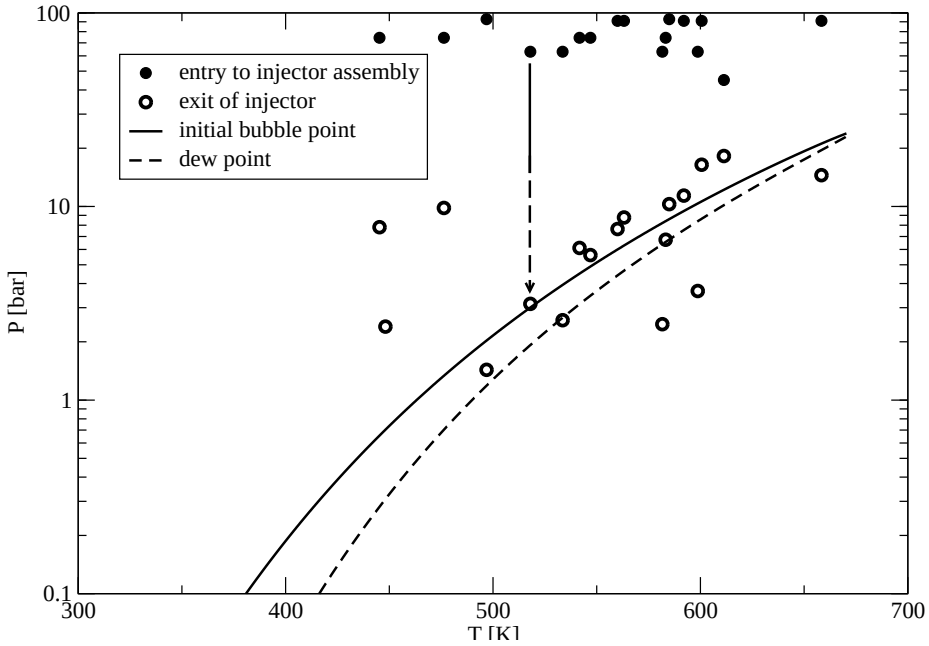

Figure 8.2. Loci of bubble and dew points for JP8. Given by Lee et. al. [29]

diagram when the vapor phase first appear and when the last amount of liquid all disappear, respectively. Note that for a multi-component system, the bubble and dew points are distinct in the $p - T$ diagram. These curves mark off the liquid, vapor, and two-phase regions. The critical point as well as the bubble and dew points near the critical region predicted by this surrogate model also agree with data found in [13]. Although other thermodynamic and transport properties of JP8 can be evaluated readily with the same surrogate model, it would need to be extended into the superheated regime. Superimposed in this Fig. 8.2 are the state of the JP8 found just upstream of the injector assembly (solid circles) and at the injector exit (open circles) that were calculated in a system level study on a supersonic cruise aircraft that uses JP8 as the coolant. The position of these points relative to the bubble and dew point curves would tell not only the thermodynamic of the fuel in the system but also indicate the condition when the jet fuel can reach the superheat condition. The high pressure ranges (solid circles) ensures that the fuel is in the subcooled state within the fuel line. However, this pressure would have to be throttled down within

the injector assembly and eventually, the fuel would exit the injector and "sees" the combustor pressure (open circles). One can readily see that some of the open circles lie in the two-phase and in the vapor regions. If during this transit within the injector assembly, the flow time is shorter than the vaporization time, then, the jet fuel may reach the superheated state.

The system level analysis provided the fuel flow rate information and thus the characteristic flow time of the injector assembly. A comparison with the characteristic time for the relaxation of the superheated jet fuel indicated that the two are comparable. Thus the relaxation of the superheated fuel would have to be modeled as a finite rate process and the Homogeneous Relaxation Model (HRM) was utilized to describe it.

Since properties in the superheated regime cannot be measured directly (being an unstable state), an extrapolation method was employed to calculate their values. For a given set of variables $< p, h, x >$ that defines a state (superheated or otherwise), if the value of instantaneous mass fraction, x corresponds to the equilibrium value x^{eq} for the given $< p, h >$ i.e. $x = x^{eq}(p, h)$, then the system is in the equilibrium state. In this case, the liquid and vapor properties can be readily calculated for the given surrogate model by the standard properties code such as SUPERTRAPP [20]. If $x < x^{eq}(p, h)$ then the fluid is superheated, and the liquid properties at p were calculated by extrapolating their values from the closest regions in the pressure space where the liquid is in the subcooled state. Note that this extrapolation scheme must conserve the enthalpy of the two-phase fluid. To do so, first the *reference* pressure $p' > p$ is found such that $x = x^{eq}(p', h)$. This pressure p' takes on the role of the saturation pressure for single component systems. The liquid and vapor components at this pressure p' are imagined to be isolated with their respective enthalpy and composition held fixed. Then the properties of this liquid are evaluated at several values of pressure $\geq p'$ in the subcooled state. This allowed the calculation of the

coefficients in a Taylor's expansion which was used in an extrapolation step from p' to p to get the liquid state properties at p. The properties of the vapor, on the other hand, pose no problem as they all can be evaluated readily at p since $p < p'$ and vapor would remain in the vapor state. The fluid properties for the two-phase system are evaluated by combining the liquid and the vapor values as follows:

$$\bar{\phi} = (\nu * \phi^n + (1 - \nu) * \phi^n)^n, \quad n = \pm 1 \tag{8.1}$$

Equation 8.1 represent the weighted and the weighted harmonic means. Here, ϕ denotes any fluid property averaged over the two phases such as density ρ, conductivity λ, and viscosity μ; and ν denotes the weighting factor which is either the quality x or the void fraction α. For viscosity, (8.1) was used with $\nu = \alpha$ and $n = 1$. Similarly, for thermal conductivity and density (8.1) was used with $\nu = x$ and $n = 1$. The multicomponent JP8 property evaluation is highly accurate in metastable region of the two−phase system. For the single component simulations described in the previous chapter, the REFPROP [32] suite from NIST is employed for property evaluation. The property evaluation in the metastable region using REFPROP follows a simpler approach where physical properties are based on their equilibrium values. Though not exactly accurate, this is deviance in viscosity and thermal conductivity does not cause any significant error due to the high Reynolds number of these flows.

8.2 Nozzle Results

First consider two cases both with upstream pressure fixed at 15 [bar] and the back pressure set to 9 and 4 [bar], respectively. Fig.8.3 depicts the isocontours of the density and the void fraction for these two cases. In both cases, vapor formation originated at the inlet corner and developed along the length of the nozzle resulting in the configuration of a high density core surrounded by a low density region near the wall. The initiation of vaporization at the sharp corner is due to the sensitivity

of the nucleation rate to pressure and the sensitivity of the bubble growth rate to the nucleation number density. Overall evaporation rate increases rapidly in a non-linear fashion with the concentration of vapor bubbles because their existence dramatically lower the energy the superheated liquid needs to overcome in order to vaporize [4]. This phenomenon is captured in the HRM model incorporated. Although the density variation in the radial direction was significant, the fluid remained in the superheated state throughout as the quality of the jet fuel remained low within the nozzle (a small change in x resulted in a large change in density due to the large difference in densities of the two phases). At the exit of the nozzle, the fluid was still in the superheated condition. This would have significant impact on breakup of the jet core downstream of the nozzle.

It is also evident in Fig. 8.3 that when the back pressure dropped, vaporization became more prominent. Fig.8.6 shows the radial variation of void fraction at the exit plane at different back pressures. The ejection angle of the fluid was also observed to increase with decreasing back pressure which is a consequence of the increase in vaporization. A continuous drop of back pressure however, did not result in a corresponding linear increase in the mass flow rate. As vaporization occurs along the nozzle, the local pressure is pushed up towards p' (analogous to saturation pressure for a single component system) thus attenuating the effect of a lower back pressure in raising the mass flow rate. In the limiting case, this would result in a choking behavior. Fig.8.4 depicts plots of the pressure along the centerline of the nozzle as the back pressure is dropped which illustrate this phenomenon.

To further investigate the effects of choking and its mitigation strategy, simulations were performed with the inflow pressure kept constant at 15 [bar] and dropped the exit pressure from 14.5 [bar] to 1 [bar]. The plot depicted in Fig. 8.5 demonstrated the phenomenon of choking as the mass flow rate plateaued at 9 [bar]. Choking differs from the unity Mach number critical flow phenomenon in that it is due to

the rapid expansion of the superheated fluid that pushes back the flow. Choking can occur at a subsonic speed (w.r.t. frozen acoustic speed) and has been reported in a number of experiments performed with superheated water [43, 17]. To mitigate this restriction on mass flow rate, one can, similar to the choked flow phenomenon in high Mach flows, increase the upstream inlet pressure. To illustrate this, the down stream pressure was fixed at 6 [bar] and the inflow pressure was raised. The lower limit of the inlet pressure was 15 bar as any lower pressure will result in the fluid being superheated at the nozzle inlet. The increase in the mass flow rate with the increase in the upstream pressure, as shown in Fig. 8.5, provides a simple algorithm to control the effect of choking.

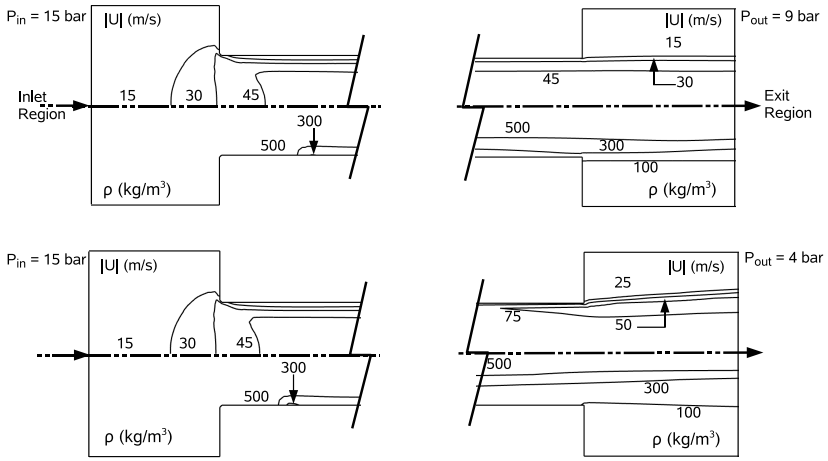

Figure 8.3. Pressure and density contours for cases with back pressure of a) 9 bar and b) 4bar

As mentioned earlier, experimental data is currently awaited for the validation of calculations using JP8 as a working fluid. The timescale correlations used in this set of calculations use coefficients obtained with water experiments [10]. Since the physical properties of JP8 vary significantly from water, these coefficients will need to be fine tuned with respect to the obtained experimental data.

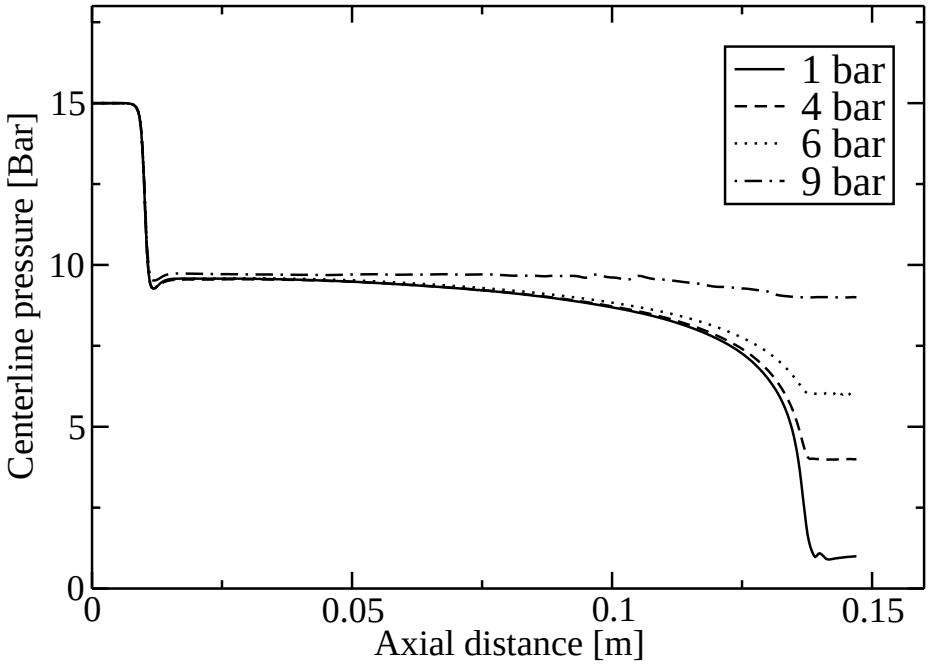

Figure 8.4. Pressure drop along the length of the channel

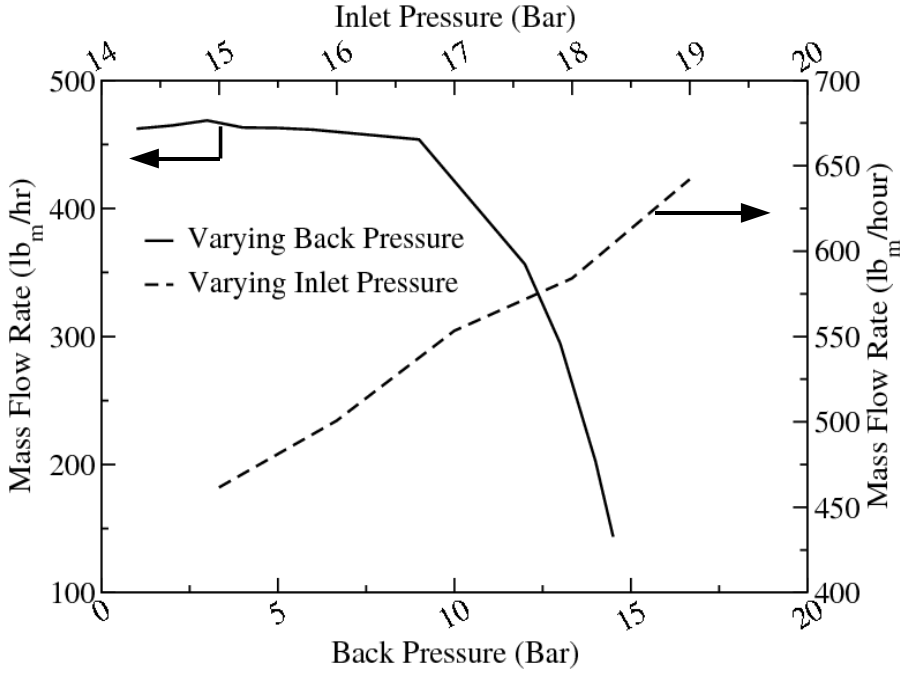

Figure 8.5. Variation of mass flow rate with inlet and back pressure

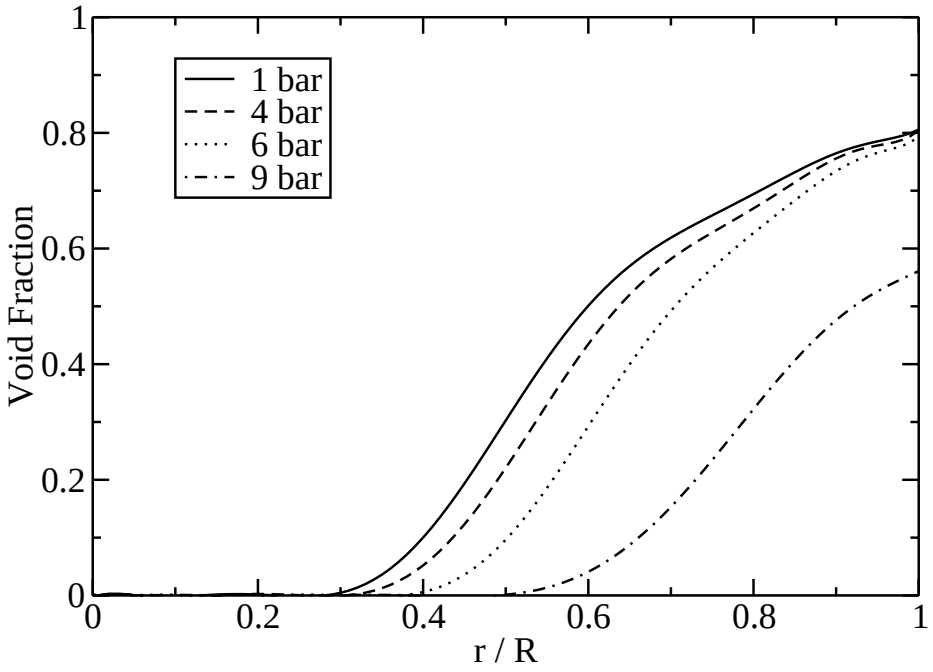

Figure 8.6. Radial variation of void fraction at injector exit

CHAPTER 9

SPRAY ATOMIZATION RESULTS

The atomization and breakup models devised, discussed in Chapter 6, resolves two independent (but coupled) physical processes that can lead to the breakup of the core. When the velocity of surrounding air relative to the core is increased i.e. increased Weber number, the surface wave due to the aerodynamic instability will grow faster. Whereas, when the degree of superheat is increased, the non-equilibrium evaporation within the core will increase making flash atomization more likely.

An experiment devised and conducted by researchers at United Technologies Research Center, East Hartford, CT and Engine Research Center, Irvine, CA [30]. The experiment was performed with the degree of superheat being varied while keeping all other system parameters constant to find out the condition when the atomization mechanism switches from one to another. The back pressure "seen" by the injector is kept constant at the atmospheric condition. The degree of superheat is altered simply by raising the temperature or enthalpy of the fuel while the mass flow rate is kept constant. The experiment was started with a value of temperature that corresponds to the subcooled region and it was confirmed that the breakup process is controlled by the instability mode, i.e. , the existence of a long intact liquid core with droplets stripping out of the liquid column. A photograph of a spray atomized under the instability mode is shown in Fig. 9.1. The temperature is then increased beyond the subcooled condition. It was found that instability based atomization persists well into the region when the fuel, if it were in the equilibrium state, would be entirely in the vapor state. At a temperature of 519 [K], a transition process was observed.

The system "jumps" between the aerodynamic instability mode and the flash atomization mode. A photograph of a spray atomized under the flash atomization mode is shown in Fig. 9.2. In the flash atomization mode, the liquid core was not observable. Visually, in this transitional regime, the system switches between the configurations depicted in Figs.9.1 and 9.2 rapidly in a random fashion.

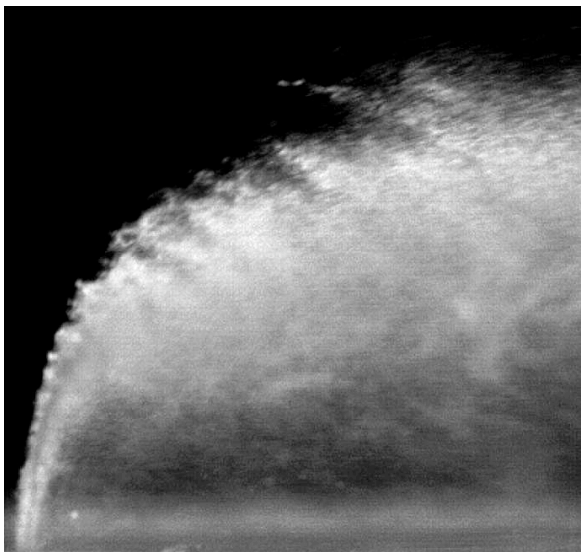

Figure 9.1. Shear instability induced breakup of a liquid jet. The liquid core can clearly be seen prior to its breakup (atomization) [30].

When the temperature is then raised beyond 519 [K], the system would remain steadily in the flash atomization mode, i.e. , the spray pattern remains constant and resembles what is shown in Fig. 9.2. Besides the visually different spray patterns, in the flash atomization mode, an attempt to measure the droplet size revealed a dramatic difference between these two atomization modes. In the instability based atomization case, it was possible to measure the droplet size distribution. However, for the flash atomization case, (at the same measurement location downstream of the jet exit), the droplet size falls below the instrument's lower limit. Although it was not possible to measure the droplet size resulting from flash atomization,

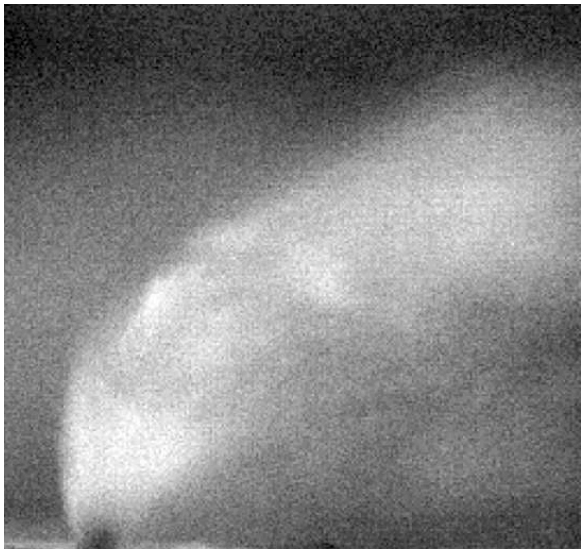

Figure 9.2. Flash vaporization induced breakup of a superheated jet. The liquid core disappeared and the atomization process occurs near the exit of the nozzle orifice. [30]

visual confirmation was achieved that there were fine droplets resulting from the flash atomization process.

The atomization model can be exercised at any point in the subcritical region of the P-T space (excluding the solid regime). The models then can be utilized to find out in the P-T space, the regions where atomization is effected either by the shear or the flashing mode. A binary cut algorithm was coupled to the atomization model in the following way. For each value of P, a search is initialized by setting two values of T i.e. T_{min} and T_{max} such that the primary breakup is caused by shear instability at $T = T_{min}$ and by flashing at $T = T_{max}$. These two values always exist since one can put simply $T_{min} = T_{bub} - 1$ and $T_{max} = T_{superheat\ limit} + 1$. This is followed by the standard binary cut algorithm to locate the transition value of $\tilde{T}$ for the given value of P i.e. $\tilde{T} = \tilde{T}(P)$ such that when $T < \tilde{T}$, instability based atomization occurs; when $T > \tilde{T}$, flash atomization takes place. The locus of $\tilde{T}(P)$ is dependent on the air velocity relative to the liquid core at the exit of the nozzle. High values of this relative velocity favors the shear instability breakup mode.

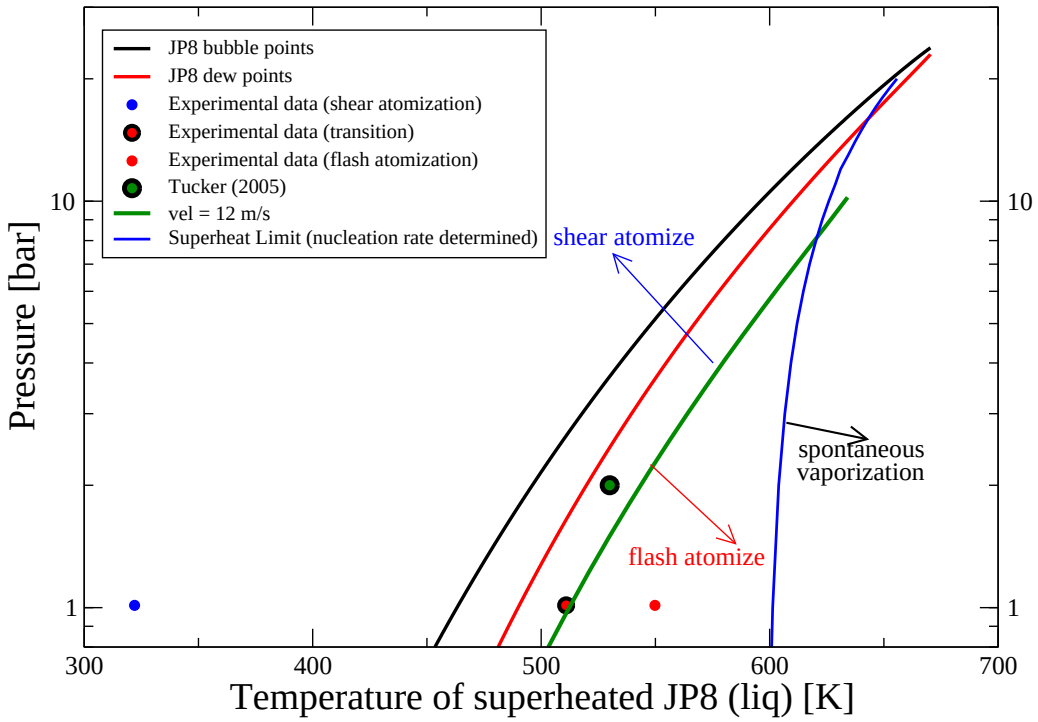

Figure 9.3. Curves that mark the boundary in the T-P space separating the region were atomization is effected either by the shear atomization or flash atomization mode. Experimentally determined value of T at 1 atmospheric pressure in the current work for this transition is shown for comparison. Additionally, a value reported at 2 atmospheric pressure [56] is included as well. Plots of the loci of the bubble and dew points are included for comparison.

The loci of the transitional points $\tilde{T}(P)$ are plotted as the green curve in Fig. 9.3 using the value of the relative air velocity employed in the experiment. The corresponding transitional point at $P = 1.01325$ $[bar]$ measured experimentally is depicted as the black circle with a red core in Fig. 9.3. One can see that the theoretical prediction agrees with the experimental datum. In Tucker et al. [56], a transitional point at 2 atmospheric pressure was estimated theoretically and later on verified experimentally. This point is also reported in Fig. 9.3 as the black circle with a green core at 2.265 $[bar]$.

The green curve in Fig. 9.3 shows the transition temperature for different values of pressure. As can be expected, higher values of pressure requires a higher degree of superheat to induce flash atomization. A designer can simply use the green curve to figure out the temperature required, for given values of pressure and jet relative velocity, to take advantage of flash atomization. Although not shown, when the relative jet velocity is increased, the green curve moves to the right. This is so because an increase in the relative jet velocity would raise the Weber number which in turns would make the shear layer more unstable. Consequently, the flash atomization would have to occur at a higher degree of superheat. The nucleation rate imposed superheat limit is also depicted in Fig. 9.3. This curve intersects the shear-flash atomization transition curve. Thus, for a given value of the relative jet velocity and at a sufficiently high ambient pressure, as one increases the fluid temperature, one would cross the superheat limit curve first. In this case, as the temperature is increased, the superheated fluid will never undergo the finite rate vaporization (controlled by nucleation and bubble growth), but instead, will undergo spontaneous vaporization when this limit curve is crossed - the atomization step is bypassed entirely. Thus, Fig. 9.3 describes all the vaporization modes exhibited by a supheated jet: atomization due to shear instability, atomization due to the finite rate relaxation of a superheated fluid, and the spontaneous vaporization of the fluid.

9.1 Drop Size Variation

The predicted drop sizes after atomization and breakup are functions of the relative jet velocity, temperature of the superheated fluid, exit cone angle and the ambient pressure of the chamber. The drop size variation for three different relative jet velocities are shown. The cone angle for all these cases is 0^o. The two competing modes of atomization and breakup, i.e. instability based and flash boiling based, are completely independant of each other. As a result of this, the lengthscales predicted by each mechanism is quite different. An abrupt change in this lengthscale is noted when the mechanism which causes breakup switches from one to another. The transition points for the jet breakup are noted by the discontinuity in the drop sizes. In full spray calculations drop sizes will be sampled from a distribution with the predicted mean drop size. This will smoothen any such discontinuos changes in drop sizes.

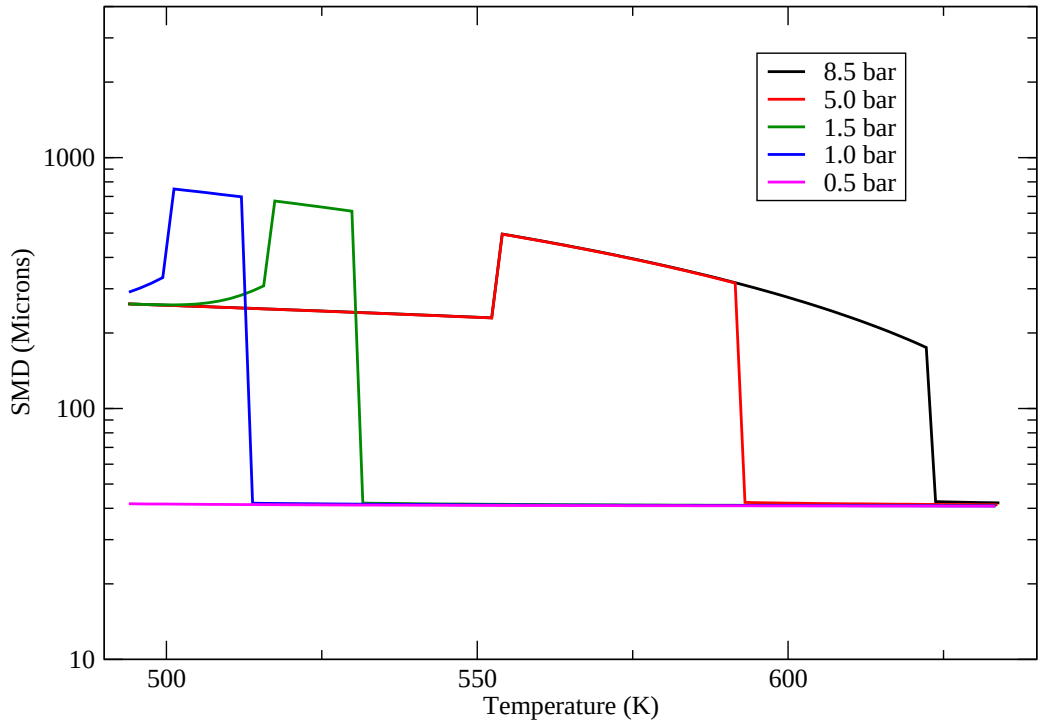

Figure 9.4. Variation of primary drop size, relative jet velocity = 12 m/s

For the case of a relative jet velocity of 12 m/s, shown in Fig.9.4 the drop sizes predicted due to instability based primary atomization is in the range of 200 to 800 microns, depending upon the ambient pressure conditions. The flash induced breakup is a thermodynamic phenomenon and the length scale associated with it, is a function purely of the degree of superheat. This is noted by fairly uniform drop sizes in the range 40 microns, which is independent of the jet relative velocity. However, the onset of flash induced breakup depends on the jet relative velocity and the ambient pressure. The increase in the ambient pressure shifts the transition from instability based breakup to higher liquid temperatures.

It is noted that for an ambient pressure of 0.5 bar only flash induced atomization occurs. For higher pressures there are two distinct transitions in the drop sizes. The transition occurring at higher temperatures, for all the cases, is from instability to flash induced breakup. The lower temperature transition is the switch in the drop size based from Eqn. 6.21 to Eqn. 6.20. One of the controlling factors for the flash induced drop size is the constant C in Eqn. 6.24, which can vary depending on the amount of dissolved gases in the liquid.

The stand−alone secondary breakup tests used a value for the initial drop size equal to the size obtained at the end of primary atomization for a particular temperature and pressure. Fig.9.5 shows the variation of the drop size after secondary breakup with respect to temperature of liquid and the pressure of the ambient gas. The transition from Taylor Analogy Breakup (TAB) to flash induced breakup occurs at a temperature similar to that of primary atomization. The drop sizes after secondary breakup are in the range of 50 to 125 microns if based on TAB and around 30 microns if flash induced. The transitional characteristics of the instability based break up for straight jets (noted by Eqns. 6.20 and 6.21) are passed down to the secondary breakup model.

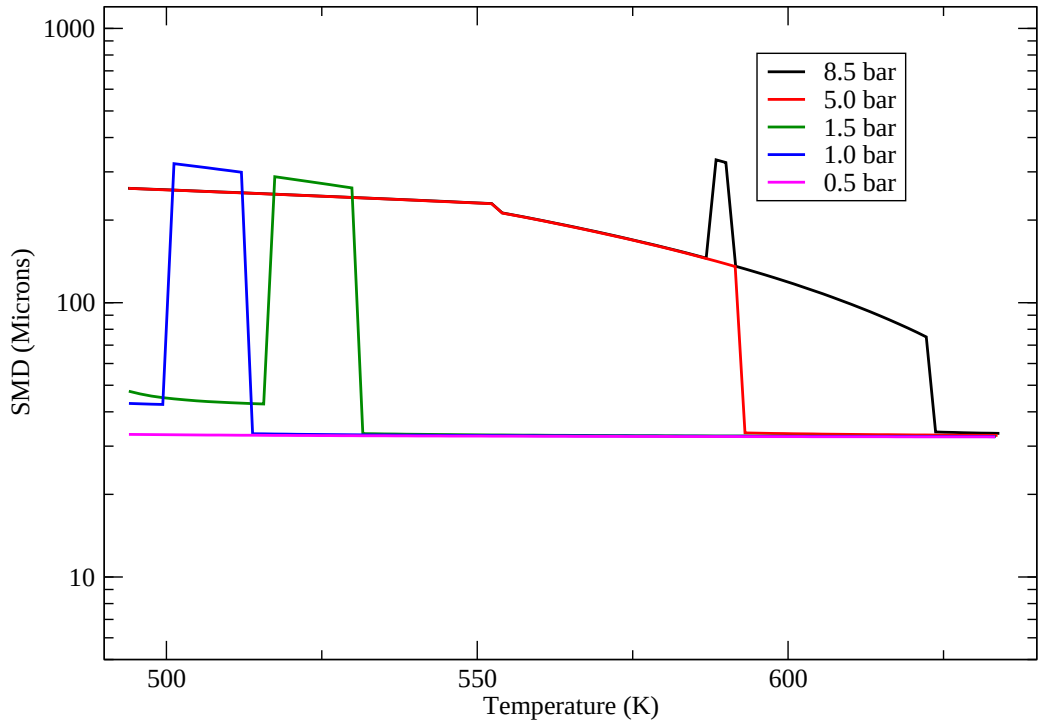

Figure 9.5. Variation of secondary drop size, relative jet velocity = 12 m/s

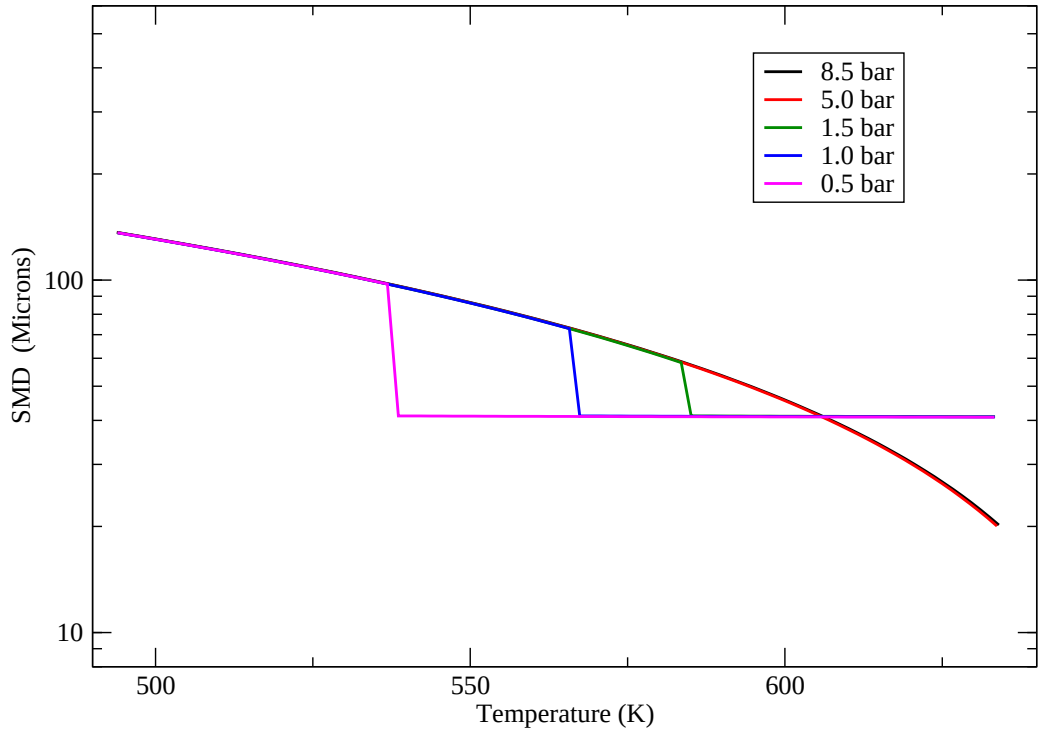

Figure 9.6. Variation of primary drop size, relative jet velocity = 30 m/s

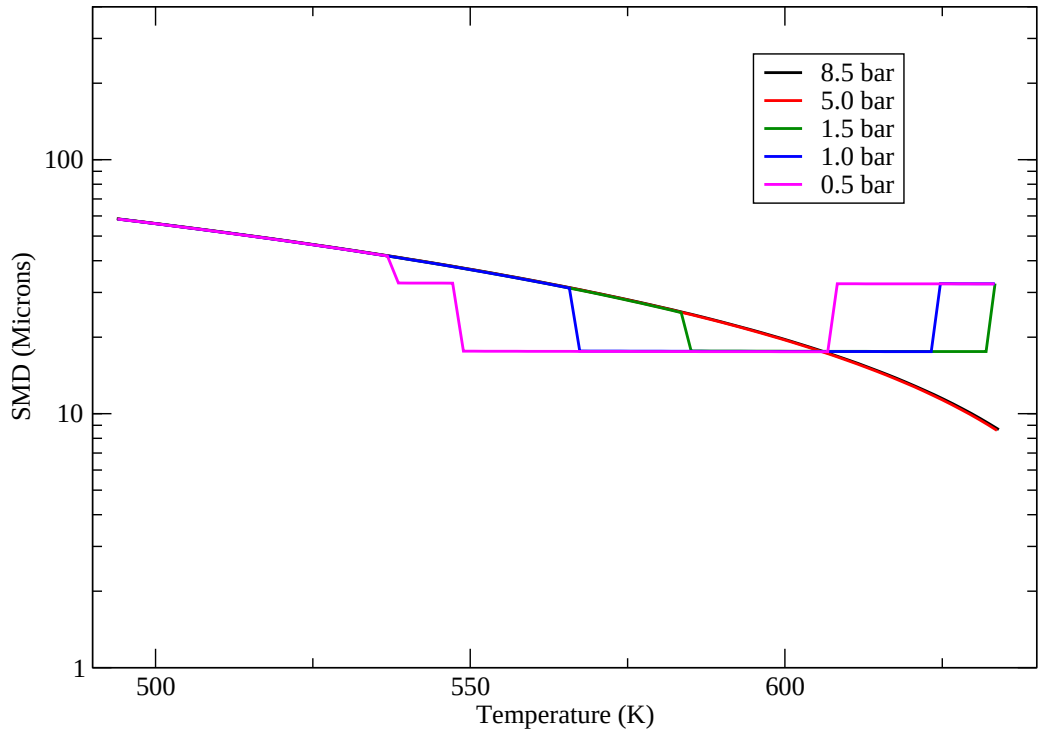

Figure 9.7. Variation of secondary drop size, relative jet velocity = 30 m/s

At higher relative jet velocities, a strong prominence of instability based atomization and breakup is expected and observed in the calculations. For sufficiently high pressures such as 5 bar and 8.5 bar, the transition to flash induced breakup does not take place in the investigated temperature range. The drop sizes obtained at higher relative jet velocities are significantly smaller as well as shown in Figs.9.6,9.7,9.8 and 9.9. For the instability based primary atomization, the breakup characteristic of the straight jet always follows Eqn. 6.20. Hence for each case there is only one transition point for primary atomization.

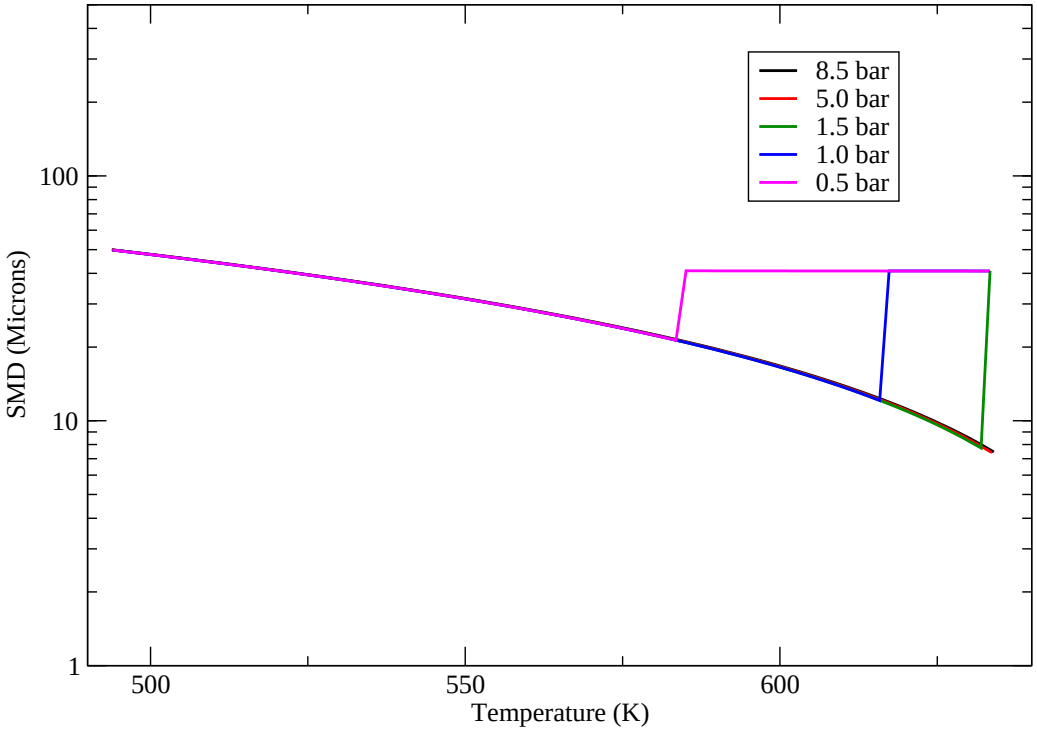

Figure 9.8. Variation of primary drop size, relative jet velocity = 50 m/s

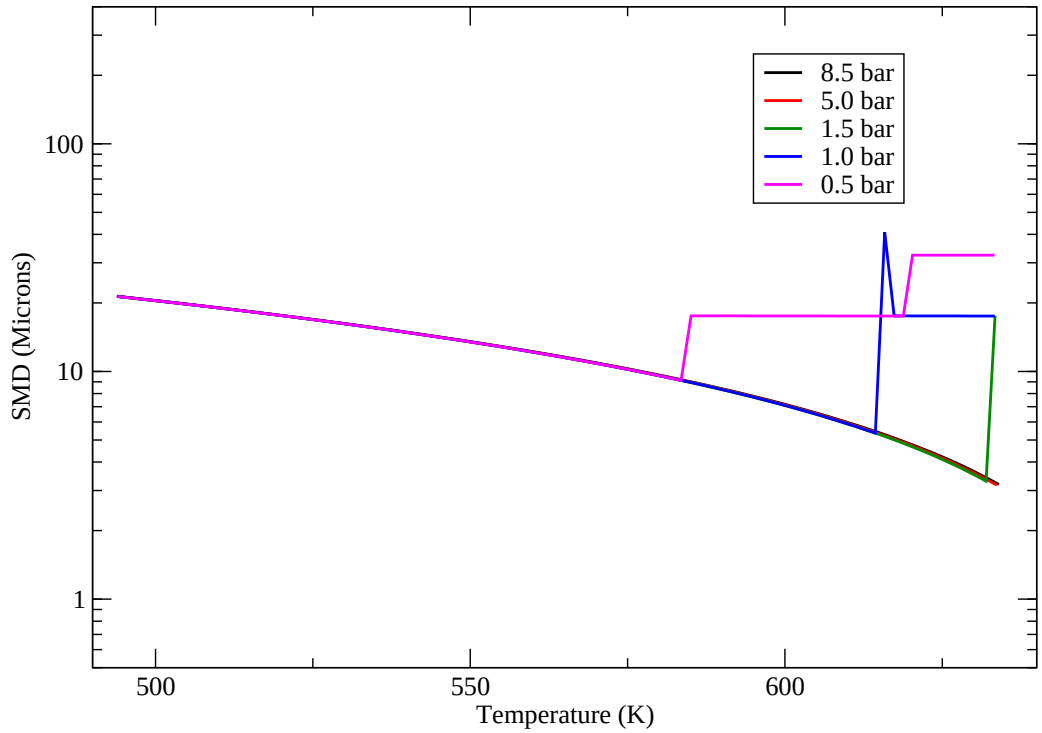

Figure 9.9. Variation of secondary drop size, relative jet velocity = 50 m/s

The stand−alone tests provide a tool for the analysis of expected drop sizes. The model predictions have shown that drop sizes are in the expected range under the given set of conditions.

9.2 Lagrangian Spray Calculation

The HRMSpray module provides a framework in which for a given set of injector conditions primary atomization is predicted along with the associated sauter mean diameter of the droplet and the atomization mode. It also provides similar data for the secondary breakup process of the droplets. For a full Lagrangian spray calculation, HRMSpray provides the necessary interface to full CFD solver. To perform a sample calculation the HRMSpray suite was coupled with FLUENT 6.3 solver using the User Defined Function (UDF) interface. An example of calculation of a jet in cross flow was performed. The working fluid in this case was JP−8. The size of the computational

domain was set 0.05mx0.05mx0.1m. The injector was located at the coordinate [-0.02499 0.0 0.025]. A steady state solver has been used to resolve the flow in the gas phase. A finite number of unsteady Lagrangian particles were injected in the time it took the steady state solver to reach convergence.

The particle tracking was set to be unsteady, with 500 particles being injected every time step, which was set to 5e-6 s. The injector diameter was 0.508 mm and the injection velocity was 40.85 m/s. The liquid temperature for this case was 540 K. The exit cone angle for the jet was 30^o and the critical void fraction at which breakup occurs for flash based atomization was assumed to be 0.6.

A cross flow velocity of 120 m/s was set in the z−direction. The boundary layer thickness was assumed to be 10mm based on discussions with Energy Research Consultants. This sample calculation was used to illustrate the usage of the atomization model to predict the breakup length and the path of the droplet. The vaporization model for the particle injections was not used in this calculation as mass transport equation was not solved in this demonstration.

Figs.9.10 and 9.11 show the velocity and pressure contours at a plane [y=0]. The velocity plot clearly shows the developed boundary layer and the effect of the jet.

The particle tracks shown in Fig.9.12, which is a close−up image, reveals the divergence of the jet as it exits the nozzle. The cross flow velocity causes a strong asymmetry, blowing the jet downstream in the direction of the cross flow velocity. As the jet exits the boundary layer and reaches the zone of the free stream gas phase velocity the effect of being pushed downstream becomes more pronounced. The predicted sauter mean diameter for the entire spray is calculated as 33 microns.

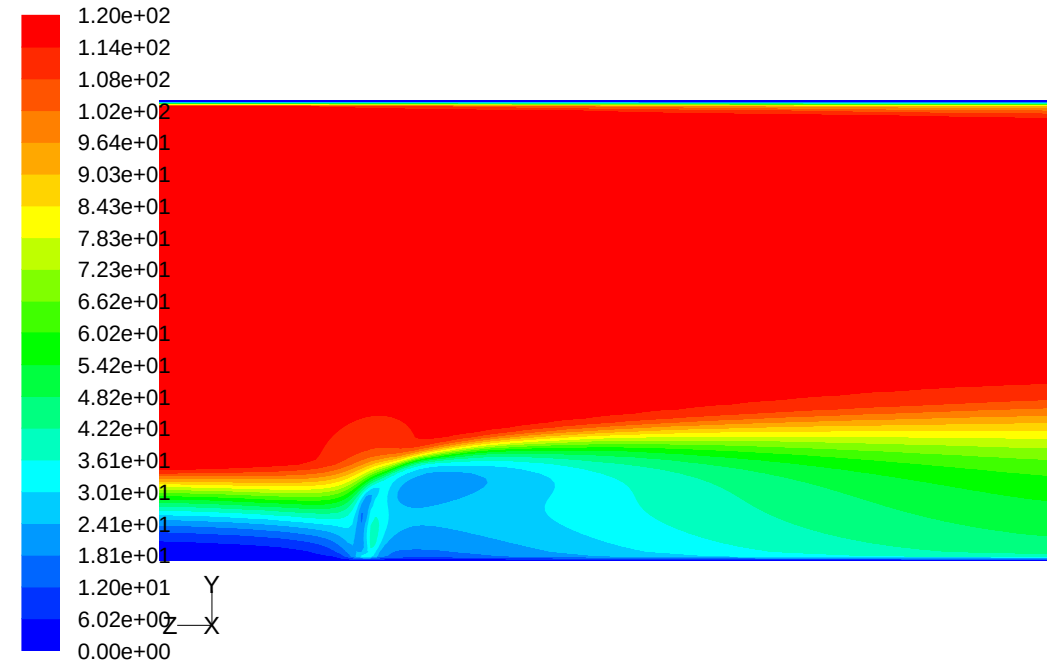

Figure 9.10. Velocity contours, Boundary layer = 10 mm

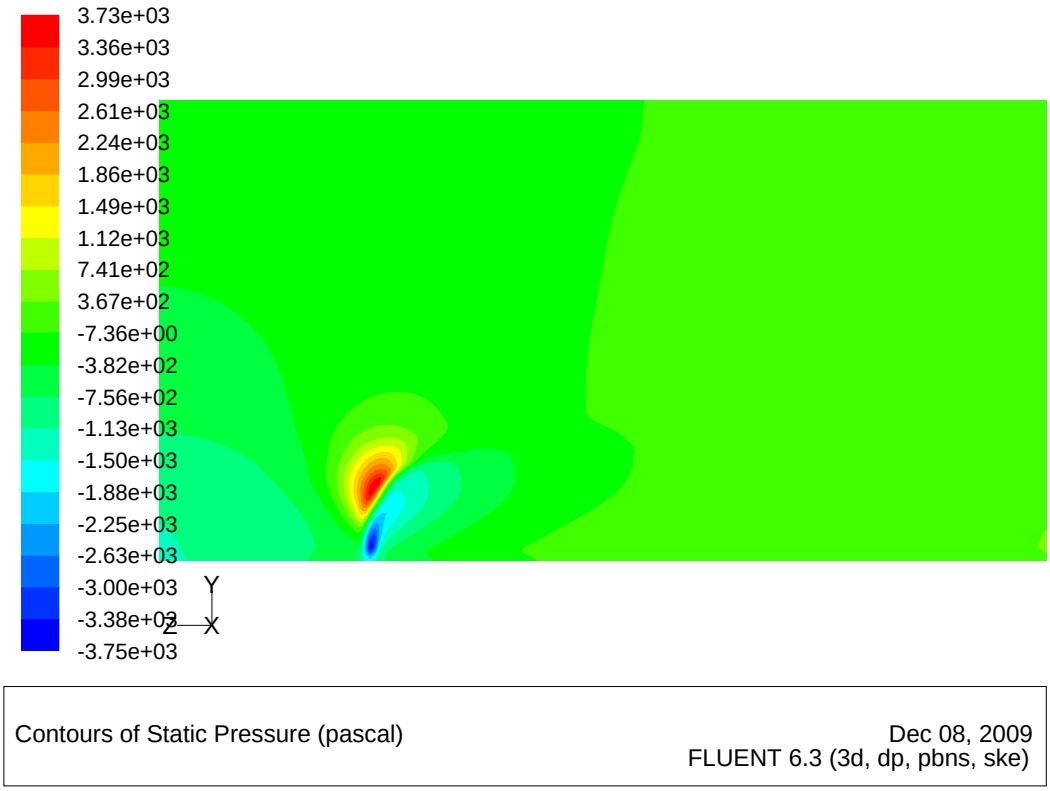

Figure 9.11. Pressure contours, Boundary layer = 10 mm

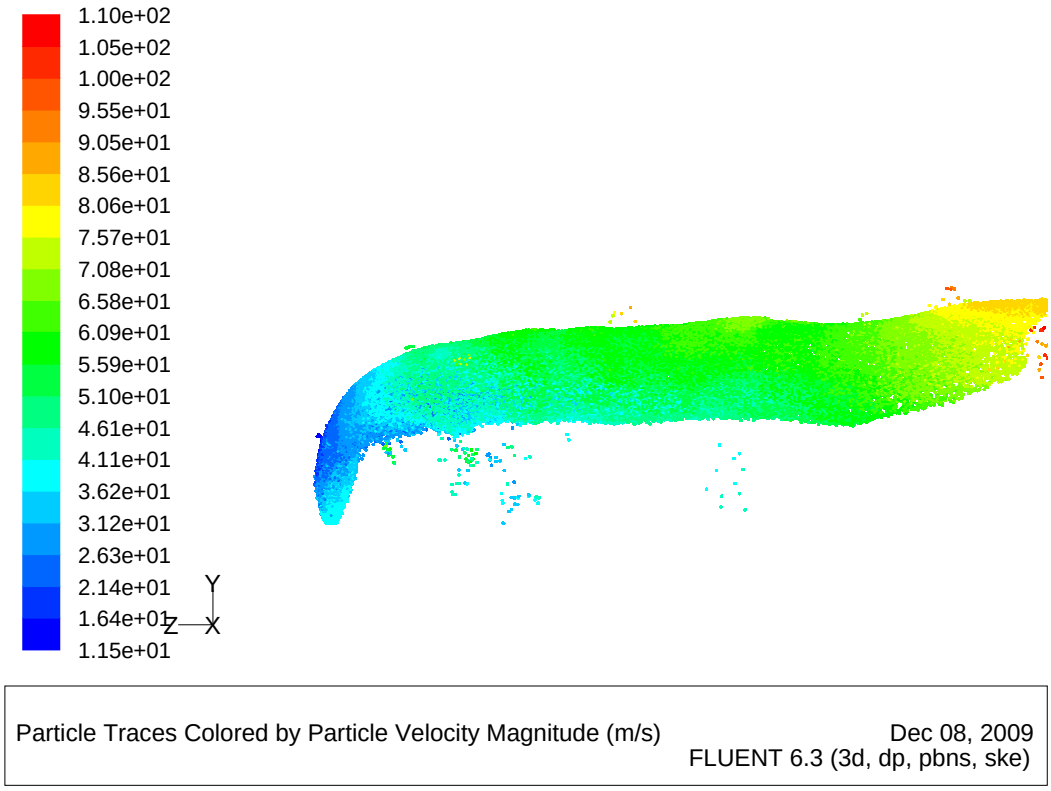

Figure 9.12. Particle Tracks, Boundary layer = 10 mm

As mentioned earlier, this calculation was performed with a purpose of demonstrating the capability of the HRMSpray model coupled to a spray solver. Currently experiments are being pursued by Energy Research Consultants (ERC) on flash boiling sprays using JP−8 as the working fluid. Valdiations and comparisons to experiments are planned for the future as soon as such data becomes available.

CHAPTER 10

SUMMARY

At elevated temperatures the interphase heat transfer is the main mechanism which provides enthalpy for phase change. This causes the fluid to be in thermodynamic nonequilibrium when the flow–through time is comparable to the relaxation time. The thermal nonequilibrium has been modeled and tested as a finite rate heat process. The Homogenous Relaxation Model (HRM) has been successfully demonstrated as a model for the phase change process in flash–boiling flows.

A new solver for internal nozzle flows was constructed using OpenFOAM, an object-oriented framework that supports a variety of discretization schemes and polyhedral meshes and is parallelized using MPI. The model was validated with several experiments from literature. Phenomena such as "vapor lock" and "two-phase subsonic choking" observed in experiments were reproduced numerically in simulations.

External spray atomization and breakup models were constructed in conjuction with phase change model. These models provide dual mode breakup mechanisms which rely on aerodynamic instabilities and internal phase change processes. An identification of regimes in thermodynamic state space was carried out to reveal the dominant process of droplet formation.

10.1 Future Work

10.1.1 Fuel properties

The fuel property database is currently can provide data for single component fluids and one multicomponent fuel, namely JP8 (jet fuel). Extensions to fuel prop-

erty database to incorporate several multicomponent fuels such as gasoline, gasoline–ethanol blends etc., are at present underway. This will enable further investigations of realistic fuel properties, including the effects of transport properties such as viscosity.

10.1.2 Validation and Adjustments of Coefficients

The lack of experimental data for validation is a concern; experimental data for internal flows using realistic fuels are not available at present. It is anticipated that, due to the importance of flash-boiling, more experimental investigations of internal nozzle flow with fuels will soon be published. At that time, further validation of this model will be possible.

The finite rate phase change model is based on an empirical timescale relationship. The coefficients for this equation are based on experimental data obtained for water. Though these provide a good starting point for calculations using hydrocarbons as working fluids, it is expected that these will need to be fine tuned once experimental data using such fluids becomes available.

10.1.3 Nucleation Model

Dissolved gases and impurities in the working fluid start as nucleations sites for phase change process. The number of these germination sites can vary with the quality of the fluid used and physical parameters such as pressure and temperature. A rudimentary constant nucleation model was implemented in this study which uses a fixed value. A sophisticated nucleation model which considers thermophysical variables is expected to improve the fidelity of the CFD calculations.

BIBLIOGRAPHY

[1] Aquino, C., Plensdorf, W., Lavoie, G., and Curtis, E. The occurence of Flash Boiling in Port Injected Gasoline Engines. *SAE Paper 982522* (1998).

[2] Barret, Michel, Faucher, Eric, and Hérard, Jean-Marc. Schemes to compute unsteady flashing flows. *AIAA Journal 40*, 5 (2002).

[3] Bilicki, Z., and Kestin, J. Physical aspects of the relaxation model in two-phase flow. *Proc. Roy. Soc. London A. 428* (1990), 379–397.

[4] Blander, M., and Katz, J. L. Bubble nucleation in liquids. *ALCHE J. 21* (1975), 833–848.

[5] Conway, John Horton, and Sloane, Neil J. A. *Sphere Packings, Lattices and Groups (Grundlehren Der Mathematischen Wissenschaften) ISBN: 0387979123*, 2^{nd} ed. Spinger, Nov 1992.

[6] Cooke, J. A., Bellucci, M., Smooke, M. D., Gomez, A., Violi, A., Faravelli, T., and Ranzi, E. Computational and experimental study of jp-8, a surrogate, and its components in counterflow diffusion flames. *Proc. Comb. Inst. 30* (2005), 439–446.

[7] Coordinating Research Council Inc. Ed. *Handbok of Aviation Fuel Properties, Third Edition CRC report No. 530.* 1983, 2004.

[8] Dagaut, P., and Cathonnet, M. The ignition, oxidation, and combustion of kerosene: A review of experimental and kinetic modeling. *Prog. in Energy and Combustion Science 32* (2006), 48–92.

[9] Dombrowski, N., and Hooper, P.C. The effect of ambient density on drop formation in sprays. *Chem. Eng. Sci. 17* (1962), 291–305.

[10] Downar-Zapolski, P., Bilicki, Z., Bolle, L., and Franco, J. The Non-equilibrium Relaxation Mokdel for One-Dimensional Flashing Liquid Flow. *Int. J. Multiphase Phase Flow 22-3* (1996), 473–483.

[11] Downar-Zapolski, P., Bilicki, Z., Bolle, L., and Franco, J. The Non-Equilibrium Relaxation Model for One-Dimensional Flashing Liquid Flow. *IJMF 22*, 3 (1996), 473–483.

[12] Duan, Ri-Qiang, Jiang, Sheng-Yao, Koshizuka, Seiichi, Oka, Yoshiaki, and Yamaguchi, Akira. Direct simulation of flashing liquid jets using the mps method. *Intl. J. of Heat and Mass Trans. 49* (2006), 402–405.

[13] Edwards, Tim, and Maurice, Lourdes Q. Surrogate Mixtures to Represent Complex Aviation and Rocket Fuels. *J. Prop. Power 17-2* (2001), 461–466.

[14] Einstein, A. Über Schallschwingungen in teilweise dissocierten Gasen. *Sitzung Berl. Akad. Physik Chemie* (1920), 380–385.

[15] et al., E. Sher. Flash-boiling atomization. *Progress Energy Combust Sci. in press* (2007).

[16] et al., J.A. Boure. Highlights of two-phase flow: on the links between maximum flow rates, sonic velocities, propogation and transfer phenomena in single and two-phase flows. *Int. J. Multiphase Flow 3* (1976), 1–22.

[17] Fauske, H. K. The discharge of saturated water through tubes. *Chem. Eng. Prog. Symp. Ser. 6* (1965), 210–216.

[18] Ferziger, Joel H., and Peric, Milovan. *Computational Methods for Fluid Dynamics*, 3rd ed. Springer, 2002.

[19] Henry, R.E., and Fauske, H.K. The two-phase critical flow of one-component mixtures in nozzles, orifices, and short tubes. *Heat Transfer 93*, 2 (1971), 179–187.

[20] Huber, M. L. SUPERTRAPP: Thermophysical properties of Hydrocarbon Mixtures Database. *U.S. Department of Commerce, NIST, Gaithersburg MD 20899* (Feb. 2003).

[21] Issa, R. I. Solution of the implicitly discretised fluid flow equations by operator-splitting. *J. Comput. Phys. 62*, 1 (1986), 40–65.

[22] Jasak, H. *Error Analysis and Estimation for the Finite Volume Method with Applications to Fluid Flows*. PhD thesis, Imperial College, 1996.

[23] Karypis, George, and Kumar, Vipin. *MeTis: Unstrctured Graph Partitioning and Sparse Matrix Ordering System, Version 2.0*, 1995.

[24] Kato, H., Kayano, H., and Kageyama, Y. A Consideration of Thermal Effects on Cavitation Bubble Growth. In *Cavitation and Multiphase Flow* (1994), vol. 194 of *FED*, ASME.

[25] Kawano, Daisuke, Goto, Yuichi, Odaka, Matsuo, and Senda, Jiro. Modelling atomization and vaporization processes of flash-boiling spray. *SAE 2004-01-0534* (2004).

[26] Kawano, Daisuke, Ishii, hajime, Suzuki, Hisakazu, Goto, Yuichi, Odaka, Matsuo, and Senda, Jiro. Numerical study on flashin-boiling spray of multicomponent fuel. *Heat Transfer-Asian Research (Wiley Periodicals, Inc.) 35(5)* (2006), 369–385.

[27] Kim, Y., and O'Neal, D. L. An experimental study of two-phase flow of hfc-134a through short tube orifices. *Heat Pump and Refrigeration Systems Design, Analysis, and Applications 29* (1993), 1–8.

[28] Knapp, Robert T., Daily, James W., and Hammitt, Fredrick G. *Cavitation*. McGraw-Hill, 1970.

[29] Lee, J., Madabhushi, R., Fotache, C. Gopalakrishnan, S., and Schmidt, D. Flashing flow of superheated jet fuel. *Proc. Comb. Inst. In Press, Obtainable at: http:dx.doi.org* (2008), doi:10.1016j.proci.2008.06.153.

[30] Lee, J. C., M., Corn, C., Fotache, S., Gopalakrishnan, and P., Schmidt D. Atomization of superheated jet fuel. In preparation.

[31] Lee, J. C., R., Madabushi, C., Fotache, S., Gopalakrishnan, and P, Schmidt D. Flashing flow of superheated jet fuel. *Proceedings of Combustion Institute 32*, 2 (2008), 3215 –3222.

[32] Lemmon, E.W., Huber, M.L., and McLinden, M.O. *NIST Standard Reference Database 23: Reference Fluid Thermodynamic and Transport Properties-REFPROP*, version 8.0 standard reference data program ed. National Institute of Standards and Technology, Gaithersburg, 2007.

[33] Minato, Akihiko, Takamori, Kazuhide, and Susuki, Akira. Numerical study of two-dimensional structure in critical steam-water two-phase flow. *Journal of Nuclaear Science and Technology 35*, 5 (May 1995), 464–475.

[34] Moody, F.J. Maximum flow rate of a single component, two-phase mixture. *J. Heat Transfer 87*, 1 (1965), 134–142.

[35] Nouri, J.M., Mitroglou, N., Yan, Y., and Arcoumanis, C. Internal Flow and Cavitation in a Multi-Hole Injector for Gasoline Direct-Injection Engines. *SAE Paper 2007-01-1405* (2007).

[36] Nurick, W.H. Orifice cavitation and its effect on spray mixing. *Journal of Fuids Egineering-Transactions of the ASME 98*, 4 (1976), 681–687.

[37] oes Moreira, J. R. Sim and Bullard, C. W. Pressure drop and flashing mechanisms in refrigerant expansion devices. *Int. J. of Refrigeration 26* (2003), 840–848.

[38] OpenCFD. *OpenFOAM - The Open Source CFD Toolbox - Programmers Guide*, 1.4.1 ed. OpenCFD Ltd., United Kingdom, 11 Apr. 2007.

[39] O'Rourke, P. J., and A., Amsden A. The tab method for numerical calculation of spray droplet breakup. *SAE 872089* (Nov 1987).

[40] Oza, R.D., and Sinnamon, J.F. An Experimental and Analytical Study of Flash-Boiling Fuel Injection. *SAE Paper 830590* (1983).

[41] Park, B.S., and Lee, S. Y. An Experimental Investigation of the Flash Atomization Mechanism. *Atomization and Sprays 4* (1994), 159–179.

[42] Reitz, R. D. Modeling atomization processes in high-pressure vaporizing sprays. *Atomization and Spray Technology 3* (1987), 309–337.

[43] Reitz, Rolf D. A Photographic Study of Flash-Boiling Atomization. *Aerosol Science and Technology 12* (1998), 561–569.

[44] Schmidt, David P. *Cavitation in Diesel Fuel Injector Nozzles.* PhD thesis, University of Wisconsin Madison, December 1997.

[45] Schmidt, David P., Chiappeta, Louis M., Goldin, Graham M., and Madabbushi, Rabi K. Transient multidimensional modeling of air-blast atomizers. *Atomization and Sprays 13* (2003), 357–377.

[46] Schmidt, David P., Rutland, C. J., Corradini, M. L., Roosen, P., and Genge, O. Cavitation in asymmetric two-dimensional nozzles. *Journal of Engines 108*, 3 (1999), 613–629.

[47] Schmidt, D.P., Corradini, M.L., and Rutland, C.J. A Two-Dimensional, Non-Equilibrium Model of Flashing Nozzle Flow. In *Proc. of 3rd ASME/JSME Joint Fluids Engineering Conference* (1999), FEDSM.

[48] Schmidt, D.P., Rutland, C.J., and Corradini, M.L. A Fully Compressible Model of Cavitating Flow. *Atomization and Sprays 9* (1999), 255–276.

[49] Schmitz, Ingo, Ipp, Wolfgang, and Leipertz, Alfred. Flash Boiling Effects on the Development of Gasoline Direct - Injection Engine Sprays. *SAE Paper 2002-01-2661* (2002).

[50] Schulz, W. D. Oxidation Products of s Surrogate JP-8 Fuel. *Symposium on Structure of Jet Fuels III* (April 5-10 1991), 383–391.

[51] Senda, J., Yoshiyuki, H., and Hajime, F. Modeling on atomization adn aporization process in flash boiling spray. *JSAE Review 15* (1994), 291–296.

[52] Senecal, P. K., Schmidt, D. P., Nouar, I., Rutland, C. J., Reitz, Rl. D., and Corradini, M. L. Modeling high-speed viscous liquid sheet atomization. *Int. J. Multiphase Flow 25* (1999), 1073–1097.

[53] Sher, Eran, and Chalm, Elata. Spray formation from pressure cans by flashing. *Ind. Eng. Chem., Process Des. Dev. 16(2)* (1977), 237–242.

[54] Spadaccini, L. J., and Huang, H. On-Line Fuel Deoxygenation for Coke Suppression. *Transactions of the ASME 125* (2003), 686–692.

[55] Tikhonenko, L.K., Kevorkov, L.P., and Lutovinov, S.Z. An investigation of the local paramters of critical flow of hot water in straight pipes with a sharp inlet edge. *Teploenergetika 25*, 2 (1978), 41–44.

[56] Tucker, Kelly Colin. *A Flash Vaporization System for Detonation of Hydrocarbon Fuels in a Pulse Detonation Engine*, afitdseny05-03 ed. Dept. US Air Force, Air University, 2005.

[57] Valero, E., and Parra, I.E. The role of thermal diseqilibrium in critical two-phase flow. *Multiphase Flow 28* (2002), 21–50.

[58] VanDerWege, B. A. *The effect of fuel volatility and operating conditions on spray from pressure swirl fuel injectors*. PhD thesis, M.I.T., 1999.

[59] Violi, A, Yan, S., Eddings, E. G., Sarofim, F., Franata, S., Faravelli, T., and Ranzi, E. Experimental formulation adn kinetic model for jp-8 surrogate mixtures. *Combust. Science and Tech. 174(11-2)* (2002), 399–417.

[60] Vortmann, C., Schnerr, G.H., and Seelecke, S. Thermodynamic modeling and simulation of cavitating nozzle flow. *Int. J. of Heat and Fluid Flow 24* (2003), 774–783.

[61] Wada, Yoshimitsu, Nishimura, Yuji, Yamaguchi, Akihiro, Magara, Noriyuki, Senda, Jiro, and Fujimoto, Hajime. Controlling PCCI Combustion with Mixed Fuel - Application of Flashing Spray to Early Injection. *SAE Paper 2007-01-0624* (2007).

[62] Wallis, G.B. Critical two-phase flow. *Multiphase Flow 6* (1980), 97–112.

[63] Weller, Henry G., G.Tabor, Jasak, Hrvoje, and Fureby, C. A Tensorial Approach to Computational Continuum Mechanics Using Object–Oriented Techniques. *Computers in Physics 12*, 6 (1998), 620–63.

[64] Wu, P-K, Shahnam, M., Kirkendall, K., A., C., Carter, and A., Nejad. Expansion and Mixing Processes of Underexpanded Supercritical Fuel Jets Injected into Superheated Conditions 9. *33rd AIAA/ASME/SAE/ASEE Joint Propulsion Conference and Exhibit July 6-9 Seattle, WA AIAA 97-2852* (1997).

[65] Yu, H., Mironov, V., and Razina, N. S. Supersonic Effects with Subcooled Water Flowing Through Cylindrical Nozzles with a Sharp Inlet Edge. *Thermal Engineering 34*, 10 (1987), 587–595.

[66] Zeigerson-Katz, M., and Sher, E. Fuel Atomization by Flashing of a Volatile Liquid in a Liquid Jet. *SAE Paper 960111* (1996).

[67] Zeng, Y., and Lee, C. An Atomization Momdel for Flash Boliling Sprays. *Combust. Sci. Tech. 169* (2001), 45–67.

[68] Zeng, Y., and Lee, C.F. An Atomization Model for Flash Boiling Flow. *Combustion Science and Technology 169* (2001), 45–67.

[69] Zuo, B., Gomes, A. M., and Rutland, C. J. Modelling Superheated Fuel Sprays and Vaporization. *Int. Journal of Engine Research 1* (2000), 321–336.